A Seismic Transmission System for Continuous Monitoring of the Lithosphere: A Proposition

A Seismic Transmission System for Continuous Monitoring of the Lithosphere: A Proposition

Proefschrift

ter verkrijging van de graad van doctor
aan de Technische Universiteit Delft,
op gezag van de Rector Magnificus prof. dr. ir. J.T. Fokkema,
voorzitter van het College voor Promoties,
in het openbaar te verdedigen op woensdag 27 februari 2002 te 10.30 uur
door Rudolf UNGER
elektrotechnisch ingenieur
geboren te Delft

Dit proefschrift is goedgekeurd door de promotoren:
Prof. dr. ir. J.T. Fokkema
Prof. dr. ir. P.M. van den Berg

Samenstelling promotiecommissie:

Rector Magnificus,	voorzitter
Prof. dr. ir. J.T. Fokkema,	Technische Universiteit Delft, promotor
Prof. dr. ir. P.M. van den Berg,	Technische Universiteit Delft, promotor
Prof. dr. ir. C.P.A. Wapenaar,	Technische Universiteit Delft
Prof. dr. S.A.P.L. Cloetingh,	Vrije Universiteit Amsterdam
Prof. dr. ir. P.P.J. van den Bosch,	Technische Universiteit Eindhoven
Dr. K. Roy-Chowdhury,	Universiteit Utrecht
Dr. M.D. Verweij,	Technische Universiteit Delft

Published and distributed by: DUP Science

DUP Science is an imprint of
Delft University Press
P.O. Box 98
2600 MG Delft
The Netherlands
Telephone: +31 15 2785678
fax: +31 15 2785706
E-mail: DUP@Library.TUDelft.NL

ISBN 90-407-2278-1

Keywords: earthquake prediction, seismic transmission, Lithosphere

Copyright © 2002 by R. Unger

All rights reserved. No part of the material protected by this copyright notice may be reproduced or utilized in any form or by any means, electronic or mechanical, including photocopying, recording or by any information storage and retrieval system, without permission from the publisher: Delft University Press.

Printed in The Netherlands

To Susana and Marijke

... some compensation for the adverse effects of pursuing an idea ...

Contents

Introduction **1**

1 Earthquake Prediction Review **9**

1.1 Types of earthquakes 9

1.2 Earthquake process models 10

1.3 Probing the Earth for earthquake precursors 16

2 Controlled-Signal Seismic Transmission System Technology **19**

2.1 System concept 20

2.2 Communications technology topics 22

2.2.1 Signals to be emitted 23

2.2.2 Quadrature processing theory 37

2.2.3 Alternative quadrature component processing 52

2.2.4 A novel signal detection and timing algorithm 53

2.2.5 Signal arrival time error analysis 54

2.3 System requirements 64

2.4 System realization concept 65

2.4.1 The signal emission source 67

2.4.2 Earth propagation 73

2.4.3 Signal reception 77

2.4.4 Front end signal processing 77
2.4.5 Simulation 79

3 Elastodynamic Wavefield Perturbation 85

3.1 The elastodynamic wave equations 87
3.2 Wave equations for the particle velocity 92
3.3 Propagation in an inhomogeneous background: body wave ray theory 96
3.3.1 Ray theory constraints 97
3.3.2 Ray tracing and Green tensor 99
3.4 Final considerations 102

4 Conclusions 105

Bibliography 111

Summary 115

Samenvatting 119

Curriculum Vitae 123

Introduction

The work presented in this thesis has been motivated primarily by the challenge of earthquake prediction feasibility. Earthquake prediction (EP) requires a systematic, multi-disciplinary approach enabling the objective detection and monitoring of potential earthquake precursors. Statistics must be compiled in space and elapsed time regarding the correlation and non-correlation of presumed precursors with the occurrence and non-occurrence of regional earthquakes. These statistics must lead to either rejection or confirmation of precursor validity. The statistics obtained for one or more valid precursors must provide sufficient information for setting earthquake alarm thresholds relative to a tolerable false-alarm rate.

We approach meeting these targets with an innovative methodology, and present the design lay-out of an active seismic transmission system (Figure 1) providing the information required, by continuously probing and monitoring Lithosphere regions in space and elapsed time for significant deviations in Earth physics parameters. Such deviations may be indicative of an earthquake preparation process, and as such, are potential earthquake precursors. The system deploys signal emission and processing methods derived from communications technology, an array of new-technology vibrator sources simultaneously emitting precisely controlled, mutually uncorrelated, long-term stationary signals from fixed locations, and existing standard permanent and portable seismometer stations. The required precursor statistics are to be compiled from high-resolution measurement of elapsed-time variation in surface-observable wave propagation parameters at the stationary seismic station receivers. The need for, and the technological feasibility of realizing such a transmission system, together with its capability of obtaining the information required, are argued.

A system with the capabilities described above meets several additional

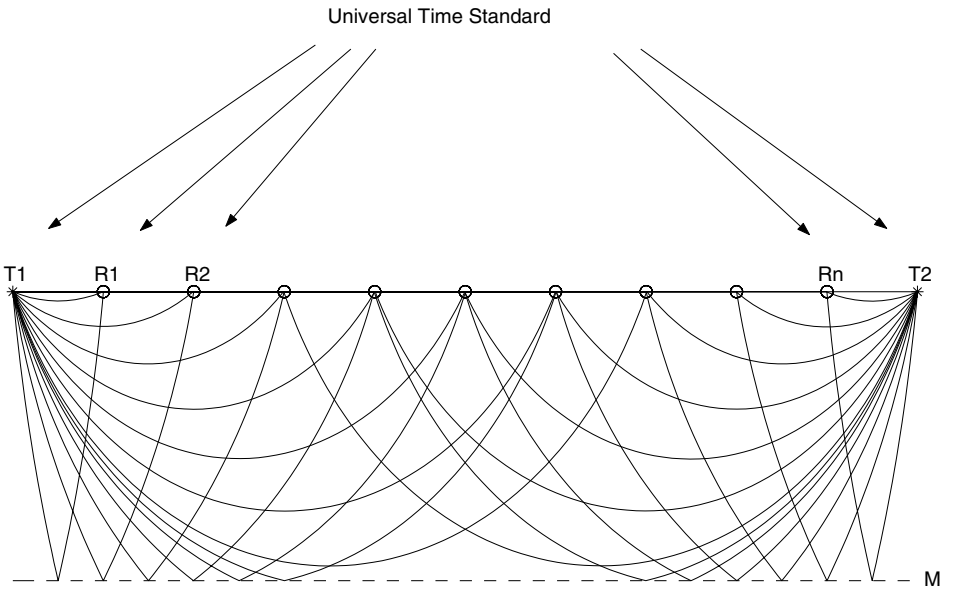

Figure 1: Two-dimensional concept of the coherent seismic transmission system. Coded, mutually uncorrelated surface force signals are emitted, in a continuously repeated fashion, by stationary vibrator sources T1, T2. Stationary receivers R1, R2, ..., Rn continuously record seismic motion. Precise signal time- and phase coherence is established by tying transmitters and receivers to a Universal Time reference. The signals may be received far below the local noise level, and are retrieved by long-term coherent stacking and matched filtering with the emitted signal codes. An earthquake preparation zone (EPZ) is regarded as an emergent heterogeneity. The rays of primary and later seismic phases provide a grid for imaging and characterizing the EPZ by elapsed-time seismic tomography. Space resolution is governed by receiver density, and by the capability of detecting, identifying, ray-tracing, and timing primary and later seismic phases. M indicates the Mohorovičić discontinuity. For clarity, only the rays of the direct and M-reflected P-waves Pg, Pm are drawn.

objectives. Since source locations, signal onset, and signal contents are known exactly, the system enhances seismic propagation studies, and constrains seismic tomography and general inversion solutions. It furthermore enables measuring the combined geology/building response to remotely generated seismic waves for earthquake engineering purposes, and may be applied as an underground reservoir monitoring system for oil, gas, and water resource management. Successful regional sub-surface imaging may improve earthquake and explosion relocation procedures, and enhance nuclear test-ban treaty verification.

Among earthquake precursors suggested, either by supposed observation or by earthquake process modeling, are changes in radon concentration, ground water levels, animal behavior, electrical resistivity, geomagnetism, crustal deformation (strain, tilt, uplift), seismicity patterns, seismic wave propagation velocity, regional earthquake focal parameters, S-wave polarization, S-wave splitting. However, in spite of many efforts and *a posteriori* 'predictions' and 'precursor detections', the sub-commission on earthquake prediction of the International Association of Seismology and Physics of the Earth's Interior (IASPEI), in charge of evaluating the validity of claimed earthquake precursors, as of March, 1994, had listed only five genuine, significant precursors (Wyss, 1997). Many 'predictions' or 'precursors' were insufficiently documented or turned out to be the product of natural parameter fluctuation more or less coinciding with a possible earthquake forming period, where parameter deviation versus earthquake occurrence correlation may have been at approximately the same level as the parameter deviation versus earthquake non-occurrence or parameter non-deviation versus earthquake occurrence correlations.

The definition of a *successful* earthquake prediction states that it must provide an accurate assessment of *time, location,* and *size* of an earthquake, including uncertainty bounds and confidence levels of these parameters. The latter must be obtained from sufficient statistics on each of the precursor parameters measured.

Earthquake precursors and predictions are divided into three categories according to the time interval of earthquake anticipation: long-term (years), intermediate-term (weeks), and short-term (days, hours). In addition, Rikitake (1981) finds presumed precursors which seem to precede earthquakes by time periods that may fall within anyone of these three categories, these might be called mixed-term precursors.

Practical EP problems include:

1. the relatively infrequent occurrence of large earthquakes from which precursors are to be deduced.
2. the apparent differences in earthquake forming mechanisms and physics in different tectonic and geologic regimes causing global inconsistency among supposed precursors.
3. the difficulty in establishing systematic measurement, with sufficient resolution, and in sufficient quantity, of potential precursor parameters.
4. the lack of insight in the mechanics and physics of the earthquake preparation process.

These conditions make it extremely difficult to gather sufficient statistics on potential earthquake precursory behavior to satisfy the conditions for issuing valid earthquake warnings. To improve the statistics data base in both quantity and quality, one would like to monitor potential precursors also for relatively small earthquakes, but then the parameter deviations may be too small to be detected, and the question still arises if the small-earthquake precursor behavior statistics can be extrapolated to larger events.

The relative lack of EP successes has led to an ongoing philosophical discussion on successful EP feasibility (Geller, 1997; Gusev, 1998; Lomnitz, 1994, 1998), one of the arguments being that earthquake forming could be a process too chaotic to enable detection. The system study in the present thesis is based on the assumption that the build-up of the tremendous amounts of energy released by earthquakes cannot go completely unnoticed and should be measurable. It is also very unlikely that this build-up would occur in such a small time interval that it would escape our attention.

The pertinent questions for resolving the EP problem then are:

1. are we capable of performing detection and measurement of earthquake preparatory process parameters with sufficient accuracy, resolution, and consistency?
2. are at least certain classes or regions of earthquakes preceded by phenomena of sufficient similarity and consistency to be identified as precursors?
3. can statistics be collected to an extent that significant deviation in one or more parameters justifies issuing an earthquake alert or warning?

4. can we produce theoretical earthquake forming models compatible with observed precursor behavior?

The present thesis addresses the first question directly in the sense of conceptually and technically attempting to establish a time- and phase-coherent, controlled-signal seismic transmission system continuously probing the Earth in order to systematically detect, measure, and monitor, with advanced accuracy, resolution and consistency, earthquake precursors in the form of *deviations in wave propagation parameter behavior*. When applied, the system should provide some answers to the precursor identification and statistics problems stated in questions 2 and 3. Through modern imaging and inversion algorithms, we can enhance insight in the physics and mechanics of the earthquake preparation process, thus aiding in providing answers to question 4. Ideally, the ensuing precursors would satisfy the definition of a short-term precursor and, possibly integrated with other surface-observable precursors, enable short-term earthquake prediction at least in some regimes.

In Chapter 1 we review the EP status. First, we categorize earthquakes by their general causes. Next, earthquake process models are reviewed, and efforts in Earth parameter monitoring in the search for earthquake precursors are summarized. Our conclusion confirms the need for the development and subsequent deployment of a novel seismic transmission system as proposed in the present study.

Chapter 2 describes the technological design lay-out for the seismic transmission system satisfying the objectives. Essential in the system concept is the incorporation of signal emission and processing techniques used in communications technology. These techniques yield complex-envelope seismograms consisting of the dual time-series of instantaneous amplitude and instantaneous phase. The latter, in particular, enables high-resolution signal detection and timing. We develop a novel signal detection and timing algorithm and a closed-form relationship between signal arrival time error and signal-to-noise ratio. The system objectives, and the implementation of the communication technology concepts put high demands on the signal source, not attainable with seismic source technology available to-date. For that purpose, new-technology surface sources, a magnetic levitation P-wave vibrator and a linear synchronous motor S-wave vibrator, have been conceived and partially developed. Details are presented of the total transmission system consisting of (1) emission of ground force signals by new-technology

surface sources; (2) wave propagation; (3) signal reception by standard fixed or portable seismic stations; (4) front-end signal processing. We conclude this chapter with a two-dimensional crustal transmission simulation.

In Chapter 3 we present the wave propagation mathematical framework for our study. In order to qualitatively and quantitatively assess potential propagation parameter changes, subject to the validity and limitations of wave propagation theory, we formulate the elastodynamic wave propagation emanating from a point-force surface source in a linear, time-invariant, locally reacting solid. Deviating from conventional formulation of wave propagation in an anisotropic, anelastic, inhomogeneous medium, we model the static stress gradient, anisotropy and anelasticity as contrast source perturbations in the wave propagation in a generally isotropic, but inhomogeneous medium. Adopting body wave ray theory to describe the background medium Green function tensor, we arrive at integral representations for contrast source inversion from which the perturbations static stress, anisotropy, and anelasticity are to be resolved. In the search for earthquake preparation zones in space and lapsed time, we consider the earthquake preparation zone as an *emergent heterogeneity* to be detected, mapped, and parameterized by elapsed-time tomography. The essence of this thesis is to provide the measurements required for such tomography; we stop short of developing and actually applying tomography and inversion algorithms.

In Chapter 4 we review the salient issues of this study. Our conclusion is that development and subsequent deployment of the system proposed are both highly desirable and feasible. Analysis and simulation suggest that the system, deploying as few as three vibrator sources simultaneously at different locations, enables Lithosphere seismic tomography through precise detection and arrival time measurement of primary and later seismic phases, made possible by our novel signal detection and timing algorithm. System deployment is expected to lead to enhancement of, and significant findings in earthquake precursor analysis, earthquake prediction, seismic tomography, and seismic wave propagation studies.

The work presented in this thesis has evolved from, and in part reflects and integrates, years of international professional experience in ocean acoustics, signal processing, and seismology, as well as proposal efforts and discussions with experts on relevant topics. A first, broad system concept version, deploying hydraulic vibrators, based on an ocean acoustics transmission system developed at The University of Michigan (Steinberg and Birdsall, 1966;

Unger and Veenkant, 1967a,b), was written in a Texas Instruments Inc. proposal in the early seventies, independent of, and with an approach different from, seismic vibrator experiment efforts initiated elsewhere (Clymer and McEvilly, 1981). The application of communications technology topics in general seismology, in particular the introduction of the complex-envelope seismogram, was developed during research concerning seismic event detection and earthquake-versus-explosion discrimination in the context of Nuclear Test Ban Treaty verification, conducted at Texas Instruments Inc. and at the Universidad Nacional de Tucumán, Argentina (Unger, 1981a,b). The idea of developing and deploying a magnetic levitation vibrator as a seismic source occurred when shown a friction-free magnetic levitation energy buffer dynamo system developed by W.A. van Kampen at Delft University of Technology. Development of this concept was initiated during a stay as a visiting scientist at the Royal Netherlands Meteorological Institute (KNMI) in 1983, subsequently continued in collaboration at Delft University of Technology, and in part reported in a short-form article (Unger, *et al.,* 1987). The linear synchronous motor S-wave vibrator feasibility was suggested in 1999 by A. Veltman during a proposal discussion with roller-coaster industry experts. During recent years, the system concept was refined, adding and working out various new ideas, and placing the concept in a mathematical seismic wave propagation theory context.

Chapter 1

Earthquake Prediction Review

In order to better understand the EP problem, in this chapter we summarize the status of the search for earthquake precursors of the wave propagation type. After categorizing earthquakes by their general causes, we review the most relevant earthquake process models, and efforts to probe the Earth for earthquake precursor detection and measurement. The review leads to our conclusion confirming the need for a novel seismic transmission system as proposed in the present study.

1.1 Types of earthquakes

We distinguish the following categories of earthquakes:

- interplate earthquakes, as a consequence of the tectonic motion and interaction at tectonic plate boundaries.
- intraplate earthquakes, presumably as a consequence of material failure at apparently weak spots either due to Earth dynamics forces within and underneath the interior of a tectonic plate, or due to tectonic stress propagated from the plate's tectonically active edges.
- volcanic earthquakes, as a consequence of volcanic processes.
- induced earthquakes, as a consequence of reservoir loading, fluid injection, liquid or gas evacuation, or underground nuclear explosions.

In all of these, the earthquake process is characterized by stress-strain relations with increasing stress up to and including material failure. Process details may differ among these categories. Below, we review the most relevant earthquake preparation process models.

1.2 Earthquake process models

Several mechanical/physical/geochemical models, in part supported by rock-fracturing laboratory experiments, and in part in an effort to explain presumably observed precursory behavior, have been postulated. Extensive literature on the subject is available; here we summarize the most prominent features as reviewed by Sobolev (1978, Russian and U.S.A. research), Byerlee (1978, U.S.A. research only), and Kasahara (1981), and also discussed to some extent in most seismology text books (e.g., Aki and Richards, 1980; Gershanik, 1996; Lay and Wallace, 1995). Most of the summary below is taken from Sobolev (1978).

The *dilatancy-diffusion (DD) model* describes the earthquake preparation process as follows. Under compressive loading (Figure 1.1), at approximately 50% of failure stress, strain starts to deviate from linearity, reflecting the onset of anelastic behavior, presumably due mainly to crack forming, causing a volume increase and changes in various physical parameters. The behavior is different for wet and dry crack systems. In wet systems, water diffusion plays an important role. Dilatancy causes a decrease in propagation velocity, where the S-wave velocity c_s is affected less than the P-wave velocity c_p, giving rise to measuring changes in c_p/c_s in addition to c_s and c_p individually as potential earthquake precursors. Later, the velocities return to normal, due to water saturation or crack closing.

Figure 1.2 shows the supposed parameter changes in wet and dry models. The volume of the parameter change region, and the precursor development time increase with earthquake magnitude. The DD model explains the occurrence of several potential precursors such as the bay-shaped change in c_p/c_s, drop in electrical resistivity, drop in well water level, and anomalous uplift, and the increase of precursor duration (the earthquake anticipation time period) with earthquake magnitude. However, in view of the lithologic constitution, the presence of mechanical stress concentrations (faults), and the temperature gradient, dilatancy expansion seems unlikely in large

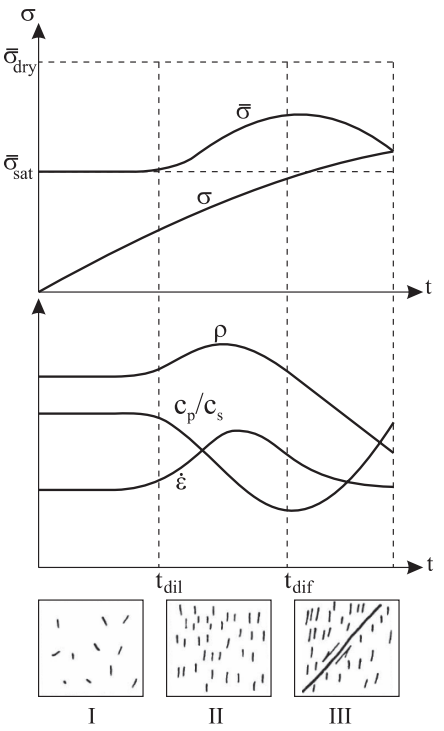

Figure 1.1: The Dilatation-Diffusion model for an earthquake preparation process: σ is the tectonic stress; $\bar{\sigma}_{dry}, \bar{\sigma}_{sat}$ are the strengths of dry and saturated rock; $\dot{\varepsilon}, c_p/c_s, \rho$ are respectively the strain rate, P-wave over S-wave velocity ratio, electric resistivity, t is time, t_{dil}, t_{dif} are the dilatancy and fluid diffusion onset times. The squares show the fracture formation process. (Sobolev, 1978).

rock volumes, e.g., on the order of 10^5 km^3. The model does not explain the transition from dilatancy tension fractures to strike-slip, nor does it explain short-term precursors such as foreshock activity, creep, and the reorientation of the focal mechanism of small earthquakes. In addition, the log-linear relation of precursor duration versus magnitude requires the *assumed* correspondence between water diffusion and tectonic stress.

The *crack avalanche crack (CA) model (*Figure 1.3), also called the *IPE model* after its origin in the Moscow Institute of Physics of the Earth, is based on the interaction of the stress field of fractures and the localization of the process of fracturing, both arising before failure of material under increasing load, and on the study of fatigue strength. In stage I the number and size of fractures gradually grows. Upon reaching a certain critical crack

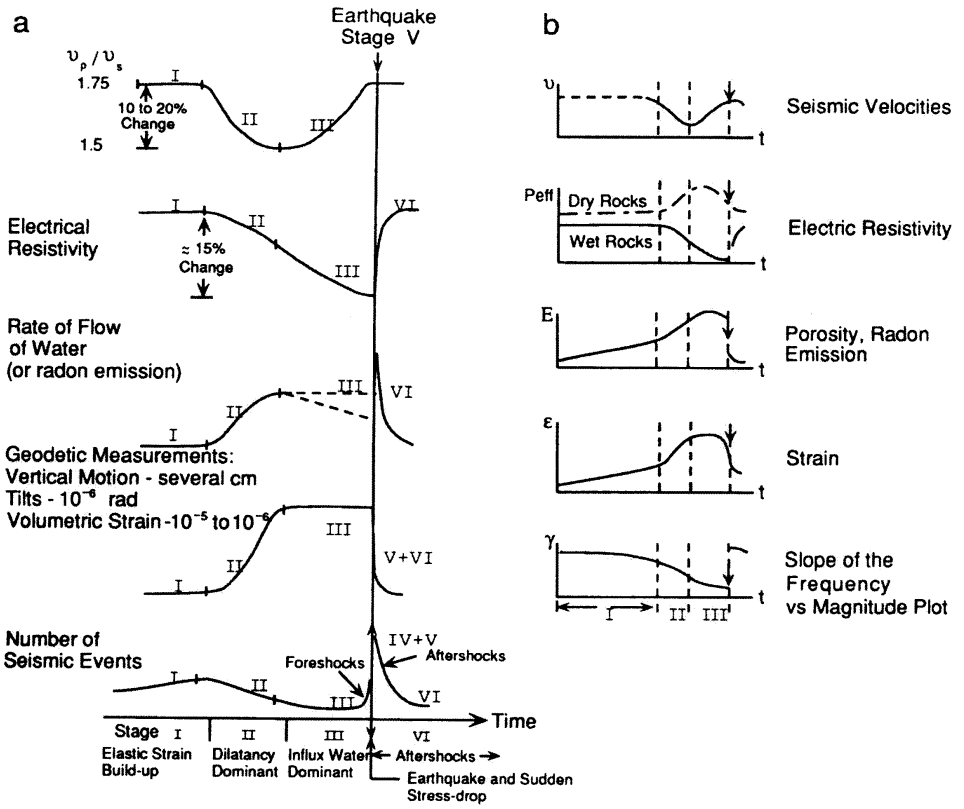

Figure 1.2: Expected physical changes for dilatancy: (a) wet model, (b) dry model. (From Lay and Wallace, 1995, after Kasahara, 1981.)

density, fracture interaction (stage II) and transition to rapid macro-faulting (stage III) occur due to fracture coalescence culminating in the earthquake. Shear fractures are dominant over tension fractures. The CA/IPE model has the merits of an exact physical basis (fatigue strength) and explains variation in seismic regimes and short-term precursors; its inadequacies include undeveloped mathematical models for quantitative precursor analysis and the problem in explaining the c_p/c_s and electrical resistivity presumed precursors.

The *stick-slip (SS) model* describes the alternating processes of slow and sudden displacements due to sudden drops in the coefficient of friction between the walls of an existing fault, as schematically pictured in Figure 1.4. Possible mechanisms for the friction drops include heating, friction force in-

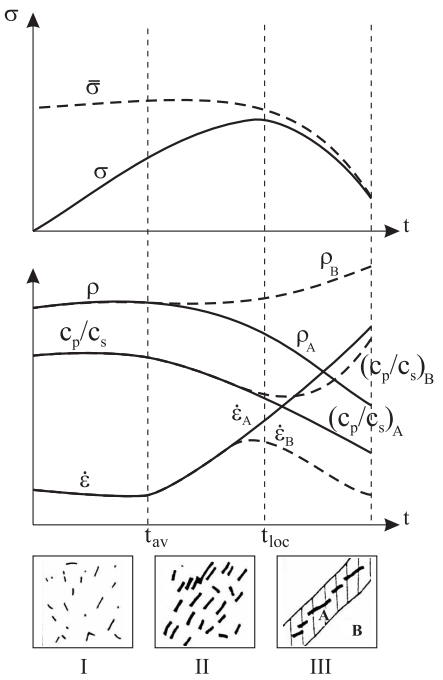

Figure 1.3: Earthquake preparation process based on the Crack-Avalanche (IPE) model. The squares show the fracture formation process. Zone A is the unstable fracture formation zone; zone B is the external zone (Sobolev, 1978).

homogeneity, brittle fracture of roughness upon contact. Porosity enhances stable sliding. The model would explain aseismic creep before earthquakes, radiation incoherence, and changes in the relationship between earthquake magnitude and frequency of occurrence, but does not explain the presence and behavior of other presumed precursors. The model has not yet treated, either experimentally or theoretically, the cases where a fault is constrained on two sides.

In addition to the phenomena described in the above models, we remark that the internal friction will change with crack formation or modification processes in any of these models, so that also wave *attenuation* changes and possibly *attenuation anisotropy* changes should take place. Attenuation and associated dispersion are usually quantized in the propagation quality factor Q and a complex wave speed c; Q probably is an effective measure of rock porosity and liquid saturation.

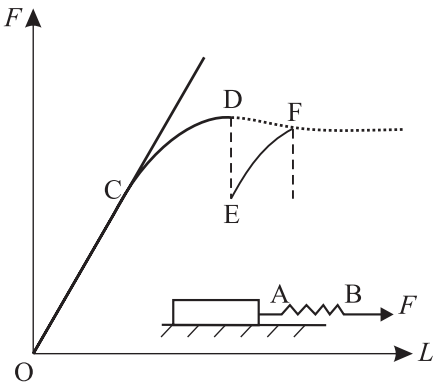

Figure 1.4: The Stick-Slip model: tangential force F vs. displacement L of point B in the mechanical model (Byerlee, 1977).

According to Sobolev (1978), the above models do not necessarily contradict each other in observation of phenomena. For instance, the stage of avalanche fracturing in the CA/IPE model may be linked to sudden dilatant expansion, although the internal mechanisms are completely different. Contradictory observations or non-observations in laboratory experiments may be caused by properties of the equipment and methods used. The CA/IPE and SS model descriptions of fractures are close in many aspects if we accept the idea of enechelon fracture forming before the formation of the macrofault. Theoretical and experimental model research still are in progress. Recently, Dillen *et al.* (1999), from ultrasonic experiments on dry Colton sandstone in a triaxial pressure machine, found that effective stress tensor changes lead to distinct anisotropy velocity changes in P- and S-waves, with dominant sensitivity to stress applied in the polarization and propagation directions.

Byerlee (1978) suggests that for the apparent upper bound of 100 bar ($= 10^7$ Pa), in natural stress change as determined from earthquake *stress drop* calculations, parameter changes may be too small to be detected. He furthermore argues that the stress required to cause dilatancy in rock is greater than the stress required to cause sliding on faults (Hadley, 1973), so that dilatancy then could not occur in country rock, but still may occur within the actual fault zone. In addition, the relative distance travelled by waves through the fault zone would be small, thus making it difficult to measure parameter changes. For that purpose, the use of *artificial sources close to the fault zone* is advocated. Our comment on this issue is that stress drop is a mathematical artefact, it is impossible to physically, *in-situ*, measure the

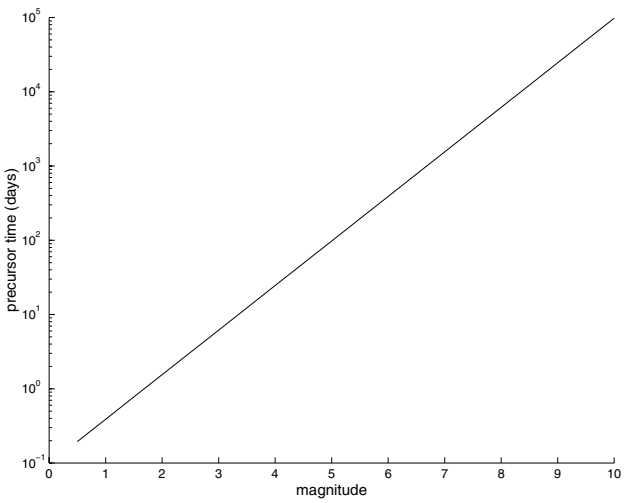

Figure 1.5: Precursor time T vs. magnitude M. After Rikitake (1981).

difference in stress before and after an earthquake directly. Therefore, actual stress change amounts may be considerably higher than those obtained from formulas. Nevertheless, we completely agree with the idea that artificial, well-controlled signal sources such as presented in this study, are probably the only way to accurately assess propagation type precursor phenomena and model validity.

Rikitake (1981) suggests an empirical relation between precursor time T and earthquake magnitude M, based on 163 reported precursor data:

$$\log_{10}(T) = 0.60M - 1.01, \tag{1.1}$$

see Figure 1.5, and also lists an empirical relation given by Dambara (1966) between magnitude and mean crustal deformation radius r in km, which he believes to hold true also for precursors satisfying the precursor time versus magnitude relation:

$$M = 1.96 \log_{10}(r) + 4.45, \tag{1.2}$$

see Figure 1.6. Thus, for an $M = 4$, an $M = 6$, an $M = 8$ earthquake, respectively, the precursor time would be on the order of one month, one year, and seventeen years, and the radius of possible precursor activity 0.6, 6.2, and 65 km. Although these relationships will have to be tested on more precise, possibly regional precursor databases, it is clear that measuring precursors, especially also those possibly occurring before relatively small

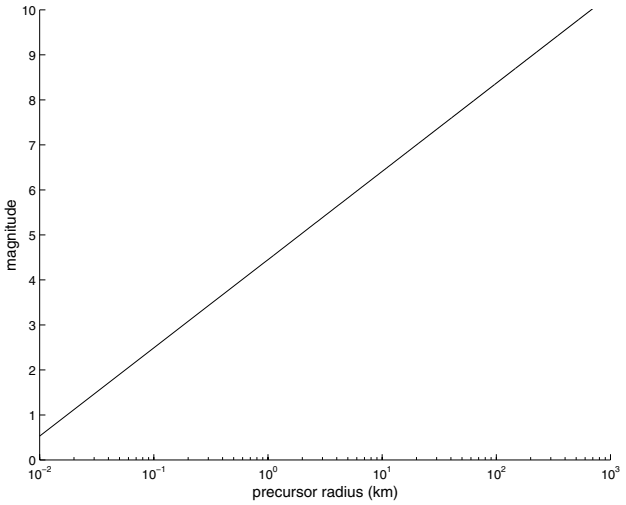

Figure 1.6: Magnitude vs. precursor radius as suggested by Rikitake (1981) after Damara (1966).

earthquakes, requires continuous monitoring with high space-time resolution, and a dense seismometer network.

Our work emphasizes the measurability and statistical significance of precursor phenomena either or not explainable from, or anticipated by existing experimental or theoretical models. Models are *not*, in our opinion, a prerequisite for a precursor's validity, although ultimately, the phenomena will have to be explained in one way or another. Further detailed model discussion, therefore, is beyond the scope of the present work.

1.3 Probing the Earth for earthquake precursors

As stated, a major problem is the space-time resolution required to reliably detect, measure, and monitor earthquake precursors. For instance, claimed deviations in propagation velocity were in general measured from signals passing through a presumed earthquake forming zone, the signals coming preferably from teleseismic earthquakes of which the onset time and hypocenter location are determined from inversion of worldwide seismogram data. This inversion requires accurate Earth parameter models including heterogeneities for all epicenter-station paths. The solutions are not unique,

and possible mismodeling and inversion residues may result in errors in onset time, wave propagation path, and hypocenter location too large to justify a claim of observed velocity deviation in a certain region. Moreover, significant precursory behavior may be missed in the intervals between teleseismic events. In some cases, the signals from regional earthquakes are used, but then the relatively small data bases may cause the onset time and location errors to be even larger. The use of *controlled sources* in the form of explosions or 'shots' of exactly known onset time and location remedies the reference event onset/location problem, but the shots will have to be executed at relatively frequent intervals near or in areas where earthquakes are expected in the more or less near future, for instance based on seismic risk maps. The procedure is costly (e.g., on the order of US$ 100,000 per shot for deep seismics purposes), is prohibitive in populated areas, and significant precursors still may be missed in the intervals between shots. Since in the above cases the source signals are not accurately known, elapsed time amplitude and signal contents variation cannot be properly studied as possible precursors in any of the above methods, leaving only velocity changes as measurable potential precursors.

The 'shots' may be replaced by coherent vibrations of limited duration as used in seismic exploration. In this technique, the required shot-equivalent seismic signal energy is expanded in time, usually in the form of a linear frequency sweep or "chirp" signal of relatively low amplitude, and compressed again by correlating (matched filtering) the received waveforms with a noise-free replica of the emitted force signal. This technique has been applied around the San Andreas Fault by a group led by T.V. McEvilly (Clymer and McEvilly, 1981; Karageorgi *et al.*, 1992, 1997), repeating the vibrations at, for instance, monthly intervals at accurately marked and prepared vibration point benchmarks. The latter reference reports observed significant changes in signal travel time and signal contents, relating some of these to natural climatic variation (e.g., rainfall), and greater variation possibly to seismic activity, including a magnitude $M = 6$ earthquake sequence, in the region of observation (Parkfield). The authors intend to increase the frequency of measurements upon intensification of precursory phenomena. *However, since the system is not continuous, the phenomena cannot be classified as short-term precursors;* it is not accurately known when exactly the changes actually took place. As the authors state:

> "The lack of closely spaced sampling before, during, and after the earthquake sequences precludes detection of abrupt changes or exact correlation of the changes with seismicity features — observations that could prove useful in short-term earthquake prediction. It is impractical to substantially decrease our sampling interval, and any future application of these observations would have to be based on a simple, *continuous* measurement." *(Emphasis by R.U.)*

Transmission range in these experiments has been limited to approximately 20 km lateral with a 40,000 lb (180 kN) peak force shear wave vibrator (Karageorgi *et al.*, 1992, 1997); 24 km depth (the Mohorovičić discontinuity, "Moho" in short) with a 12,000 lb (50 kN) peak force P-wave vibrator (Clymer and McEvilly, 1981). Seismogram length is 20 seconds, showing the primary arrivals of P-wave, S-wave, Love wave, and some coda. For high signal-to-noise ratios, the differential signal arrival time resolution, obtained from the correlogram phase spectrum, is reported to be better than one milli-second.

In addition to the mentioned disadvantage of the measurements not being continuous, we remark:

- The 20 s seismogram length is insufficient to take full advantage of the information contained in later phases and coda.
- The 20 km horizontal range is insufficient to perform earthquake precursor measurement over a region broad enough to accommodate earthquake preparation zones of which the location cannot be narrowly preestablished, such as those at active fault locations.

Our conclusion is that the detection, measurement, and monitoring of earthquake *precursors of the propagation parameter type* (e.g., changes in velocity, attenuation, heterogeneity, anisotropy), requires the *continuous, coherent, simultaneous seismic transmission of exactly known signals over a horizontal range of at least 200 km, from sources placed at different locations; signal code length must be sufficient to accommodate later phases and coda.* Any time-lapse changes in signal arrival time and signal contents then may be studied for earthquake precursory behavior, and inversion and imaging techniques applied to map, characterize, and monitor emergent earthquake preparation zones. The establishment of such a transmission system and assessing its application potential are the main objectives of the present work.

Chapter 2

Controlled-Signal Seismic Transmission System Technology

A multi-sensor seismic hazard warning system requires that components can be easily and systematically integrated, and that for each of these components reliable precursor statistics are available from which alarms can be efficiently called when exceeding a preset threshold for a given false alarm rate. This chapter presents the concept, the design, and the development status of a seismic transmission system providing such a component in the form of measured deviations in space and elapsed time in the Earth impulse response or Green function between stationary sources and receivers. These sources simultaneously emit, for indefinite time, precisely controlled, but mutually uncorrelated, stable, and continuously repeated, time- and phase-coherent ground force signals from different locations. In addition to its seismic hazard precursor identification, detection, and monitoring function, such a transmission system would provide a new tool in general seismology research, should enhance Lithosphere tomography, and may be applied in elapsed-time 3-D reservoir monitoring. Parts of the system concept were briefly presented earlier (Unger *et al.*, 1987).

2.1 System concept

Our objective is to establish the feasibility of realizing a system capable of accurately measuring and analyzing the long-term temporal variation in regional time-space impulse responses or Green functions between fixed-site seismic surface sources and seismometer stations. Figure 1 in the Introduction illustrates the system concept. Given a long-term time- and space-invariant source, this variation would manifest itself at receiving stations in changes in signal contents and arrival time of particle displacement and particle velocity. If statistically significant, such variation may be indicative of an earthquake-forming process somewhere in the wave propagation path, thus potentially establishing a bulk earthquake seismic precursor. With three-dimensional (3-D) transmission, raytracing and appropriate modeling, inversion, and imaging techniques, it may be possible to locate and further delineate these changes, and to relate them to changes in the stress and strain fields, in the stress-strain relations, and in particular physical 'constants' or Earth properties within an earthquake-forming domain. This could make it possible to also determine the domain geometry, size, and orientation, and the long-term (elapsed time) variation in these parameters. For precursors, the duration of these variations is the so-called precursor time (see Figure 1.5), in general considered to be a measure of both anticipated earthquake magnitude, and of earthquake onset time counted from the onset of the parameter variation phenomena. Compiling accurate temporal and spatial variation statistics and correlating these in time and space with the occurrence and with the non-occurrence of regional earthquakes may enable the establishment of well-defined *short-term* earthquake precursor parameters with valid alarm threshold versus false alarm rate settings. Reasonable estimates of event onset time, epicenter, orientation and magnitude may be deduced from these parameters, thus providing significant components in an integrated, multiple-precursor, regional earthquake warning system.

Technically, the broad system concept is to emit precisely known and controlled ground force signals in a continuously repeatable, time- and phase-coherent manner, for indefinite time periods. At the receiving stations, the signals in general arrive well below the local seismic noise level, but are extracted by long-term coherent, noise-weighted stacking and correlation (matched filtering) with the emitted pilot signal. Quadrature processing results in complex-envelope seismograms consisting of the correlogram dual time-series of instantaneous amplitude and instantaneous phase, the latter

playing a crucial role in high-resolution signal detection and timing. Signal time and phase coherency between signal emission and reception is established by incorporating an accurate Universal Time (UT) standard in both, the sources and the receivers.

In order to take full advantage of the information contained in the seismograms, signal code duration (equal to the complex-envelope seismogram length) must accommodate the major seismic phase arrivals as given by the Jeffreys-Bullen travel time tables for a given range, as well as signal coda. Families of *pseudo-random sequences*, to be modulated onto a low-frequency monochromatic carrier wave, provide efficient, sufficient-length signal codes for simultaneous, mutually uncorrelated, but in character identical, signal emission from different source sites.

Depending on regional frequency-dependent attenuation, local seismic noise spectrum, and desired transmission range or depth penetration, the frequency of the emitted signal must be optimized, but in any case should be within the earthquake seismology 'short-period' body-wave frequency range of 0.5-10 Hz. Present seismic land source technology (mechanic, hydraulic, or electrodynamic vibrators) does not meet the ensuing seismic signal emission requirements. Therefore, two types of new-technology seismic surface force sources were conceived, a P-wave source based on the principle of magnetic levitation, and an S-wave source derived from linear synchronous motor technology.

Concerning signal reception, most existing fixed-site and portable seismic stations, arrays or networks worldwide, with most instruments being three-component, satisfy the signal reception requirements and are equipped with a reliable UT reference. New trends in seismometry are to significantly increase sampling rate, memory, and dynamic range, allowing for even greater flexibility, efficiency, and resolution in signal processing and timing. Collected data are to be distributed in standard record formats to interested parties either directly, or via established worldwide seismic data distribution centers.

In summary, the total transmission system consists of: (1) emission of ground force signals by new-technology surface sources; (2) Earth propagation; (3) signal reception by permanent or portable seismic stations; (4) front-end signal processing in the form of complex-envelope (instantaneous amplitude and phase) seismogram generation and signal detection and timing.

We address these items in the following sections. First, in view of its essential role in our system concept, the relevant communications technology topics, in particular pseudo-random sequence signal transmission and quadrature signal processing are reviewed. We enrich this technology by developing a *novel signal detection and timing algorithm*, and derive a deterministic relation between signal timing error standard deviation and signal-to-noise ratio (snr), ranging from less than 0.5 millisecond for 36 dB correlogram snr or higher to less than 0.5 second for -6 dB correlogram snr. This permits signal arrival time measurement and analysis for a great number of later phases and signal coda, presumably sufficient for regional Lithosphere travel time tomography while deploying as few as three sources transmitting simultaneously at different permanent locations. In addition, in this tomography procedure, the timing error standard deviations may be used as inverse weighting factors for the corresponding arrival time information. Second, the system requirements resulting from the system concept, and satisfying the stated objectives are specified. Third, realization of the system in all of its components is described in detail. Based on seismic vibrator transmission experiments conducted with existing sources, and depending on local noise conditions and attenuation properties, over a horizontal range of 200-500 km sufficient snr is expected to be obtained with continuous, coherent signal transmission, stacking and matched filtering over a time period of approximately two weeks.

2.2 Communications technology topics

The two main communications technology elements we want to incorporate in our seismic transmission system are

- pseudo-random sequence (prs) signal transmission, enabling efficient, simultaneous emission of mutually uncorrelated signals of sufficient duration from different source sites. This in addition to the transmission of the more familiar frequency-modulated sweeps or 'chirp' signals used in seismic exploration.
- quadrature signal processing, leading to complex-envelope seismograms, enabling high-resolution signal detection and timing.

We discuss these items in the following subsections.

2.2.1 Signals to be emitted

The system has been designed to enable emission of a broad class of signals, and to apply digital communication technology as used in radar and space communication. Signals include different forms of conventional frequency modulation sweep or 'chirp' signals (Edelmann and Helbig, 1984) in general used with hydraulic vibrators in seismic exploration, and the family of maximal pseudo-random sequences (prs) modulated onto a selected monochromatic carrier wave (Golomb, 1967; Steinberg and Birdsall, 1966, Unger and Veenkant, 1967a,b; Cunningham, 1979; McEliece, 1987). Both classes are a form of pulse expansion; pulse compression is achieved by means of 'matched filtering', i.e., correlating the received signal with a noiseless replica of the emitted signal, the 'pilot' signal. For a linear Earth transfer function, the matched filter output equals the signal auto-correlation function convolved with the Earth impulse response or Green function. In white noise, i.e., noise with a flat power spectrum, the coherent matched filter power processing gain equals $2WT$, i.e., the coherent matched filter improves the amplitude signal-to-noise ratio by a factor $\sqrt{2WT}$, where W is the effective signal bandwidth and T is the signal duration. In non-white noise, the processing gain is less than $2WT$.

The basic properties of the chirp and prs signals are illustrated in Figure 2.1, and further discussed below. We find that, for our objectives, the prs signals are the preferred emission signal class. For our system, the prs signal transmission and processing technique is adapted from underwater acoustics transmission technology originated by T.G. Birdsall (Steinberg and Birdsall, 1966; Unger and Veenkant, 1967a,b).

The chirp signal

The chirp signal (Figure 2.1) has been applied most commonly in seismic exploration and deep seismic profiling, with frequency sweeps of typically 10-100 Hz or subranges thereof, and 8-32 Hz, respectively. For chirps of sufficient dispersion, i.e., the time-bandwidth product, the power spectrum is rectangular, and the envelope of the autocorrelation function is a $[\sin(x)/x]^2$ curve, with main-lobe maximum at $x = 0$, and side-lobe extrema of approximately $1/5, 1/8, 1/11$, etc. at $x = 3\pi/2, 5\pi/2, 7\pi/2$, etc. The $[\sin(x)/x]^2$ curve is scaled with the signal power. Chirp signals are employed as linear or non-linear, up- or downgoing sweeps, and can be coded for special

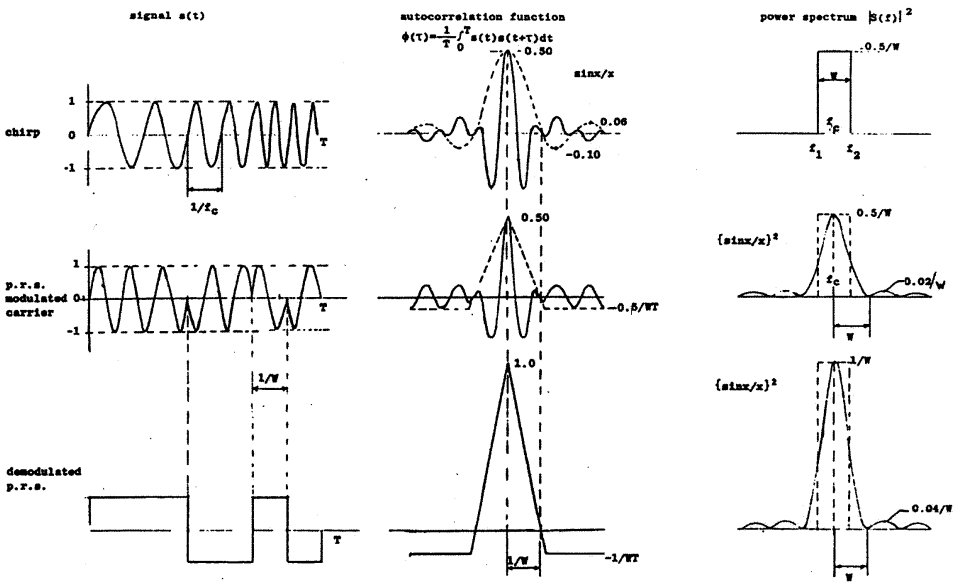

Figure 2.1: Characteristics of linear frequency sweep (chirp) signal and prs signal (Unger et al., 1987).

purposes, e.g., for side-lobe suppression (Edelmann and Helbig, 1984). Side-lobes can also be suppressed by means of signal tapering, at the expense of reducing emitted signal energy.

The pseudo-random sequence signal

The prs signals (Figure 2.1) have been used in a great variety of applications (radar, sonar, econometry, electromagnetic surveying, and others), but apparently not in routine seismic surveying, and not in earthquake seismology research. For the seismic exploration application, however, some experiments have been conducted. Cunningham (1979) finds the prs signals to be superior to chirp signals, mainly because of the inherently low side-lobe of the auto-correlation function.

The pseudo-random sequence A prs can be considered as a repeated coin-tossing experiment of which all outcomes have been pre-programmed. Thus, each prs possesses properties of randomness, but in fact is known exactly. They can be generated in a systematic manner with a series of shift-

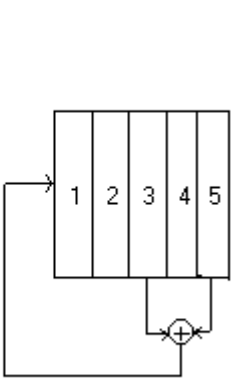

shiftregister element				
1	2	3	4	5
shiftregister contents				
1	1	1	1	1
0	1	1	1	1
0	0	1	1	1
0	0	0	1	1
1	0	0	0	1
1	1	0	0	0
0	1	1	0	0
1	0	1	1	0
1	1	0	1	1
1	1	1	0	1
0	1	1	1	0
1	0	1	1	1

Figure 2.2: Shiftregister sequence generation.

register elements and modulo-two (mod2) adder feedback (Golomb, 1967; McEliece, 1987; Roden, 1982; Viterby, 1966), see Figure 2.2. A shiftregister with N elements results in a sequence length of $n = 2^N - 1$ digits, 2^{N-1} digits equal to a logical 1, and $2^{N-1} - 1$ equal to a logical 0 or -1, or vice-versa, so that $\Pr(1) \approx \Pr(0 \text{ or } -1) \approx 0.5$. Each sequence can be identified, and is completely determined, by a set of three integers $\{N, r1, r2\}$ representing, respectively, the number of shift register elements and the two mod2 feedback elements used. The configuration in Figure 2.2 generates a $\{5, 3, 5\}$ maximal pseudo-random sequence which may be tapped from any of the shiftregister elements as given in the corresponding columns.

Similar to the outcomes of series of coin-tossing experiments, one would expect that maximum-length prs be mutually uncorrelated. But: (1) not all shift register sequences are maximum length, i.e., certain patterns appear as repeated partial sequences so that the auto-correlation function contains more than one correlation peak within one sequence period, and (2) not all maximum-length prs are mutually uncorrelated.

As an example with respect to (1) above, Figure 2.3 shows the auto-correlation functions for the prs generated by all ten mod2 feedback combinations with the end element of an 11-element shift register. Table 2.1 contains the maximum auto-correlation side-lobe value in % and in dB, relative to the zero-lag auto-correlation peak value. The prs length equals $2^{11} - 1 = 2047$ digits, so the auto-correlation noise or side-lobe amplitude of a maximum-length prs should be $1/2047 = 0.05\%$ of the zero-lag amplitude,

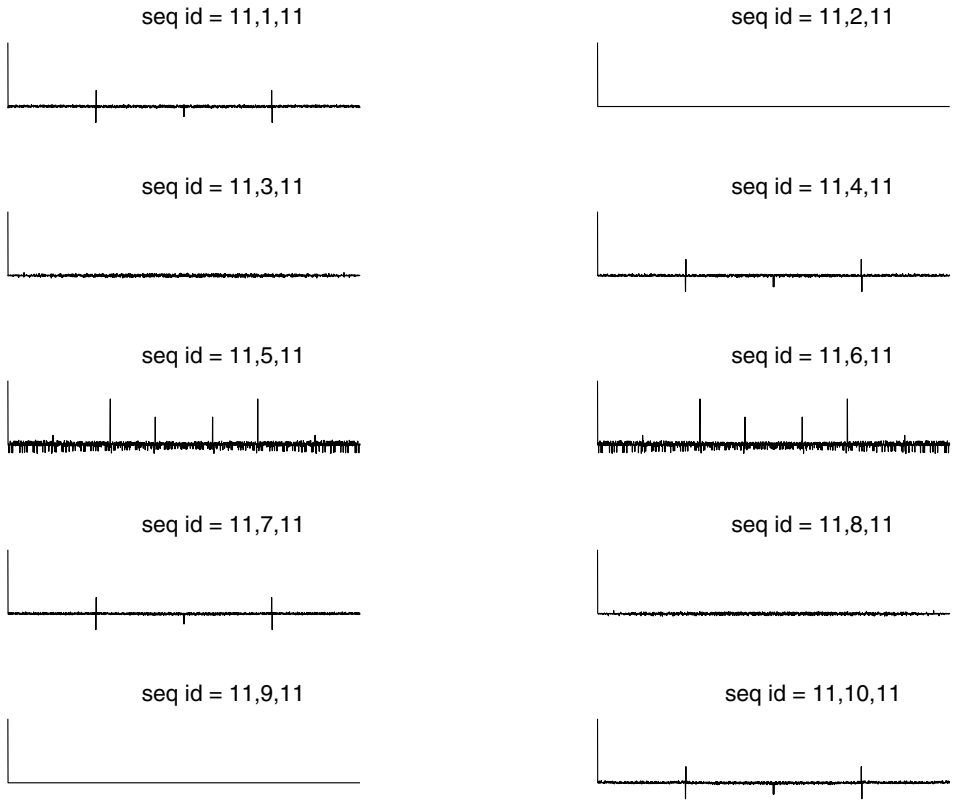

Figure 2.3: Auto-correlation functions of 11-element sequences in different feedback configurations. The zero lag is left justified.

that is, at -66 dB. We note that only the two sequences (11,2,11), (11,9,11) satisfy this maximum-length criterion. Because of their relatively low auto-correlation noise, possibly also the sequences (11,3,11) and (11,8,11) can be used, but they are not maximum-length. Observe also the symmetry in the use of feedback elements, e.g., the auto-correlation function of sequence (11,1,11) is identical to that of sequence (11,10,11); the same holds for the sequence pairs {(11,2,11), (11,9,11)}, {(11,3,11), (11,8,11)}, {(11,4,11), (11,7,11)}, and {(11,5,11),(11,6,11)}.

Concerning problem (2), the mutual cross-correlation functions and characteristics of the 'usable' sequences are given in Figure 2.4 and in Table 2.2. Apparently, not all prs are mutually uncorelated, little is known about the conditions for this mutual non-correlation (McEliece, 1987). But for rela-

Table 2.1: Prs auto-correlation noise for different 11-element shift register feedback configurations

prs id			auto-correlation noise		remarks
nels	ifb1	ifb2	%	dB	
11	1	11	25	-12	
11	2	11	0.05	-66	maximum-length sequence
11	3	11	5	-26	potentially usable sequence
11	4	11	25	-12	
11	5	11	71	-3	
11	6	11	71	-3	
11	7	11	25	-12	
11	8	11	5	-26	potentially usable sequence
11	9	11	0.05	-66	maximum-length sequence
11	10	11	25	-12	

tively long sequences as required for our purpose, families of mutually virtually uncorrelated sequences can be selected and pre-established by computer trial, as shown above. The number of different sequences equals the number of combinations created by combining, in the modulo-two adder feedback, in principle any two of the N shift register elements. However, computer trials indicate that one of the feedback elements has to be the end element. Thus, N shift register elements provide $N - 1$ different sequences. In our application, for a 2.5 Hz carrier wave, we suggest using 10-12 elements to obtain seismogram lengths (equal to the sequence signal periods) of 5-20 min, resulting in 9-11 possible sequences to choose from. Long sequences have the advantage of potentially providing more mutually uncorrelated sequences. On the other hand, in signal reception and processing, they are more vulnerable to noise bursts and signal emission or reception interruptions, which may render entire sequence durations useless for processing. One could try to increase the number of uncorrelated sequences by nesting multiple shift register feedback loops, but again, computer trials indicate that this is unsuccessful, suggesting the possible existence of some number theory law to that extent. Other possibilities are to use chirp signals and random number generated signals of which the mutual non-correlation is to be established by computer trial, in addition to the selected prs families. Also, in the cases where relatively few prs cross-correlation peaks occur within a correlogram, their arrival times can be anticipated exactly from computer

Figure 2.4: Mutual cross-correlation functions of the 'usable' sequences identified in Table 2.1. The scale is the same as used in Figure 2.3.

trials as performed here; in signal processing, these spurious signals then may be removed by means of time-notch filtering. Further investigation of suitable signal codes, including signal spectrum optimization, is left for future research. 3-D transmission requires that at least two, but preferably three or more uncorrelated sequences are emitted simultaneously from different source sites. In the case of simultaneous transmissions to be performed in different regions on the same principle, their signals could interfere after long-term stacking; therefore, preferably, *all* emission signals *everywhere* should be uncorrelated. Indeed, apparently, more research is required in order to provide larger families of mutually uncorrelated signals.

Table 2.2: Cross-correlation noise among usable sequences

prs1	prs2	cross-correlation noise	
		%	dB
11,2,11	11,3,11	8	-22
11,2,11	11,8,11	9	-21
11,2,11	11,9,11	8	-22
11,3,11	11,8,11	9	-21
11,3,11	11,9,11	8	-22
11,8,11	11,9,11	8	-22

Pseudo-random sequence modulation The prs are to be modulated as a square pulse series onto a monochromatic carrier wave of desired frequency. The modulation may be (1) binary phase, i.e., using the logical $\{1, -1\}$ sequence as amplitude modulator, resulting in phase flips of 180° of the carrier wave at each change from a logical 1 to -1 or vice versa, or (2) pure amplitude, using the $\{1, 0\}$ sequence as amplitude modulator, resulting in digits of full amplitude signal alternated by digits of zero amplitude. Adopting the terminology from the underwater acoustics transmission technology reference (Steinberg and Birdsall, 1966; Unger and Veenkant, 1967a,b), we refer to (1) as binary phase modulated sequence (BMSEQ) and to (2) as amplitude modulated sequence (AMSEQ). BMSEQ emits full sinusoid signal power continuously, AMSEQ emits approximately half the full sinusoid signal power. Usually, the digit duration is chosen as an integer number of carrier wave cycles; we will do so also in our system. Figure 2.5 shows a 7-digit BMSEQ with one-cycle digit duration and its modulation onto a 2.5 Hz cosine carrier wave in time- and frequency domain. Note the low side lobe ($=\frac{1}{7}$) in the auto-correlation function, corresponding to the low net power of the carrier wave resulting from mutual cancelation by $+1$ and -1 prs digits. In the modulated-signal spectrum the slight deviation from the $\sin(x)/x$ spectrum is caused by aliasing. Similarly, a 7-digit AMSEQ modulation is pictured in Figure 2.6.

The BMSEQ power spectrum is a $[\sin(x)/x]^2$ curve centered at the carrier frequency, the same (except for scaling) as that of a single pulse; its bandwidth W as defined in Figure 2.1 is the inverse of the duration of a single digit or pulse width. Thus, a sequence of length T seconds contains WT pulses or digits. Due to the fact that, in BMSEQ, the numbers of positive

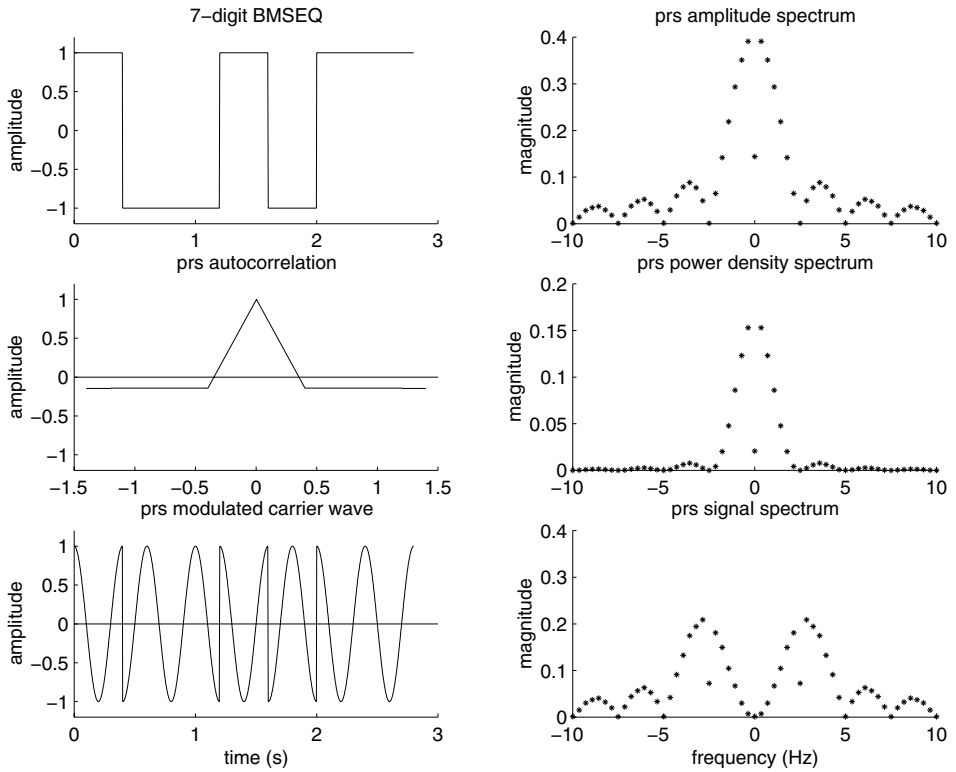

Figure 2.5: Characteristics of a 7-digit BMSEQ modulated onto a 2.5 Hz carrier wave: time domain (left), frequency domain (right).

and negative pulses differ only by one, this one pulse difference establishes the net amount of pure carrier wave power. Therefore, the carrier wave is *suppressed* by a factor WT; it appears as the side-lobe in the auto-correlation function. The spectrum of the demodulated signal has the same shape, but is centered and suppressed at dc (0 Hz). The BMSEQ auto-correlation function is given by

$$\phi(\tau) = \begin{cases} 1 - W|\tau| \text{ for } |\tau| \leq 1/W\,, \\ -1/WT \text{ for } |\tau| \geq 1/W\,, \end{cases} \tag{2.1}$$

i.e., it has a triangular peak at zero delay ($\tau = 0$) with base width equal to $2/W$, and a constant side lobe of magnitude $1/WT$ and opposite phase. The side-lobe magnitude thus is inversely proportional to the time-bandwidth product. All BM sequences of a given pulse width have the same spectrum.

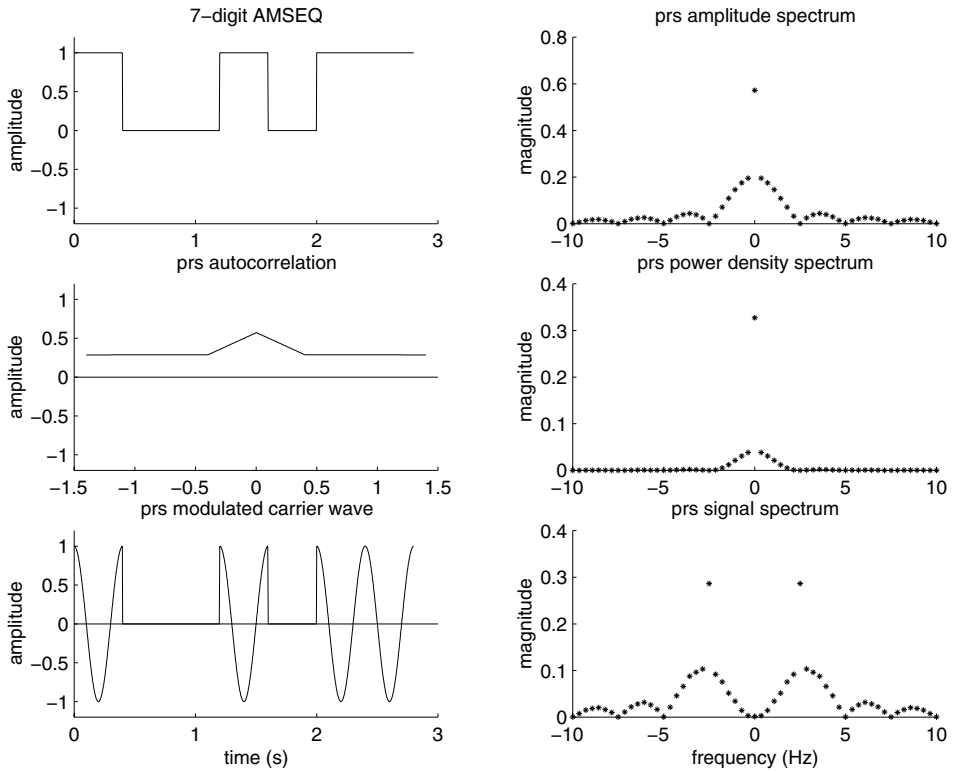

Figure 2.6: Characteristics of a 7-digit AMSEQ modulated onto a 2.5 Hz carrier wave: time domain (left), frequency domain (right).

The characteristics of the AMSEQ are similar, except that in the auto-correlation function the level of the side-lobe representing the carrier wave power is at approximately one-half of the auto-correlation maximum. The spectral line at carrier frequency is *enhanced* by a factor WT, and only approximately one-half of the energy of the BMSEQ signal is emitted. With N^1 the number of 'one' digits, and N the total number of digits in an AMSEQ period, the AMSEQ auto-correlation function is expressed by

$$\phi(\tau) = \begin{cases} \frac{N^1}{N}\,(1 - W|\tau|) \;\text{ for } |\tau| \leq 1/W\,, \\ \frac{N^1}{2N} \;\text{ for } |\tau| \geq 1/W\,. \end{cases} \tag{2.2}$$

For long sequences $\frac{N^1}{N} \to 0.5$.

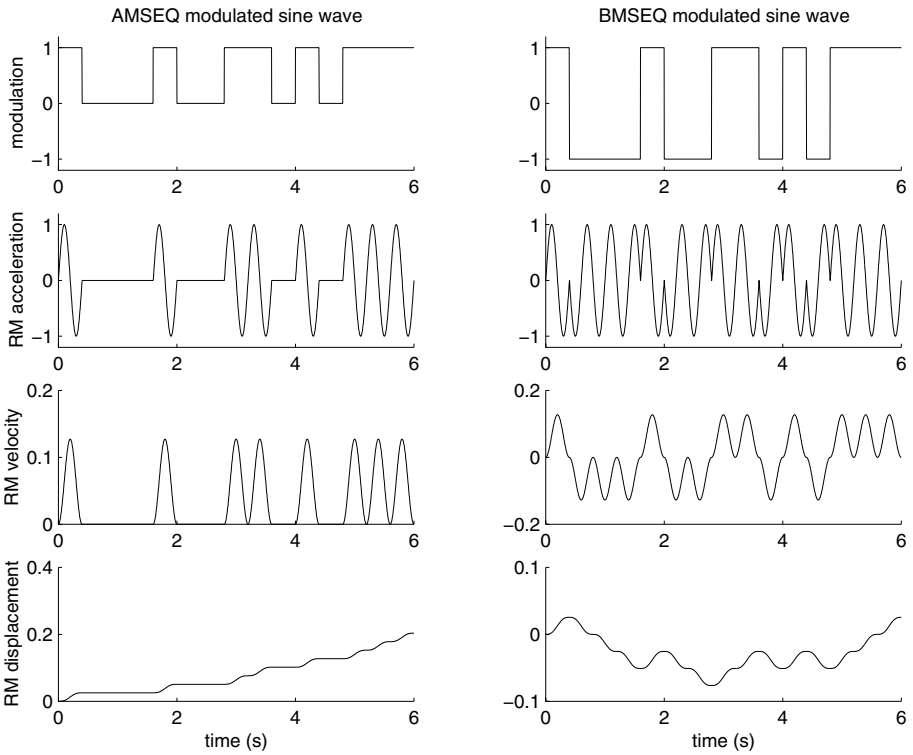

Figure 2.7: Reaction mass motion for source force signals of AMSEQ and BMSEQ modulated onto a *sine wave* carrier, causing *drift* in the reaction mass displacement function. The AMSEQ stroke is unbounded; the BMSEQ stroke is excessive and depends on the sequence length.

Consequences for vibrator reaction mass motion In seismic vibrator technology, the force exerted onto the Earth surface (the 'ground force'), is generated by moving a reaction mass in vertical direction in the case of a P-wave vibrator, and in horizontal direction in case of an S-wave vibrator. For a perfectly rigid support, the ground force signal equals the reaction mass acceleration multiplied by the reaction mass quantity, so that the ground force signature follows the reaction mass acceleration signature. The peak-to-peak reaction mass displacement amplitude is known as the reaction mass *'stroke'*. The dimensions of the vibrator are determined by the reaction mass quantity and the stroke. In turn, the reaction mass-stroke combination depends on the required peak ground force at a given minimum frequency.

So far, we have not yet discussed the type of carrier wave to be used. In

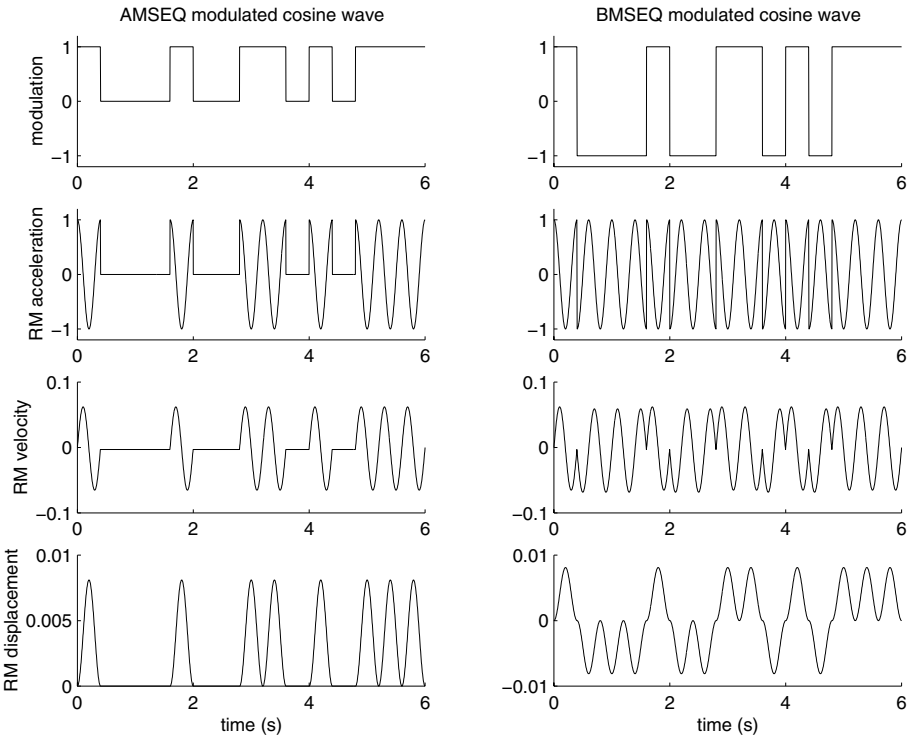

Figure 2.8: Reaction mass motion for source force signals of AMSEQ and BMSEQ modulated onto a *cosine wave* carrier: there is *no drift* in the reaction mass displacement function. The stroke is bounded and independent of sequence length.

an arbitrary kind of signal transmission, e.g., radio transmission, it probably would be irrelevant if a sine wave or a cosine wave, or, for that matter, any sinusoid with arbitrary phase offset, is used as a carrier wave. In seismic vibrator signal emission, however, this choice has significant consequences for the reaction mass motion, and in particular, for the reaction mass stroke. Figures 2.7 and 2.8 show a given vibrator reaction mass acceleration function, and Riemann integrated velocity and displacement functions, for AMSEQ and BMSEQ modulation of a sine wave carrier and a cosine wave carrier, respectively. We observe that, due to the elevated cosine velocity signature, a sine wave acceleration carrier causes drift in the reaction mass displacement. The drift is unbounded in the case of AMSEQ modulation, requiring an infinite stroke. In BMSEQ modulation, the amount of drift within a sequence period depends on the number of successive sequence digits having the same

polarization, i.e., successive +1 or successive −1 digits. This number will be greater as the sequence is longer. At the end of the sequence period the net drift equals the integration of one positively or negatively elevated cosine cycle of the velocity function. Thus, although here the displacement drift is less severe, the required stroke becomes intolerably large, in particular for long sequences and long-term continuous transmission. One might want to remedy the displacement drift situation by attempting to prescribe either the velocity or the displacement function such that the acceleration function, derived by differentiation, satisfies the required reaction mass acceleration, but this would lead to unrealizable impulse functions. Consequently, the sine wave carrier is not suited for seismic vibrator pseudo-random sequence signals.

In contrast, the cosine wave carrier does not cause any drift problem and the stroke is well bounded: the AMSEQ stroke equals $\frac{2}{\omega_c^2}$ times the reaction mass acceleration amplitude, the BMSEQ stroke $\frac{4}{\omega_c^2}$ times the reaction mass acceleration amplitude, where ω_c is the angular carrier wave frequency. In the figures, a 2.5 Hz carrier wave is used, leading to an AMSEQ stroke of approximately 8 mm per ms^{-2} reaction mass acceleration, and a BMSEQ stroke of approximately 16 mm per ms^{-2} reaction mass acceleration. In Section 2.4.1 we discuss a 50 kN peak force magnetic levitation vibrator with a 10,000 kg reaction mass moving with 5 ms^{-2} amplitude BMSEQ acceleration at a peak force minimum frequency of 2.5 Hz, requiring an 8 cm stroke.

Note that, for the same ground force, the AMSEQ stroke equals one-half of the BMSEQ stroke, at the expense of halving the emitted signal energy.

Other forms of signal emission and processing combinations In the above, we have considered either BMSEQ or AMSEQ transmission and autocorrelation. Another option is to transmit AMSEQ and correlating the received signals with the BMSEQ signal, or vice-versa, resulting in correlograms with zero side-lobe but with 6 dB signal-to-noise-ratio loss with respect to BMSEQ autocorrelation (Figure 2.9). AMSEQ can also be considered as consisting of the sum of approximately 50% BMSEQ and approximately 50% pure carrier wave (CW) transmission. The latter permits *continuous wave analysis* in which the instantaneous amplitude and phase can be tracked and monitored (Steinberg and Birdsall, 1966; Unger and Veenkant, 1967a,b). Finally, it is also possible to *coherently* alternate the

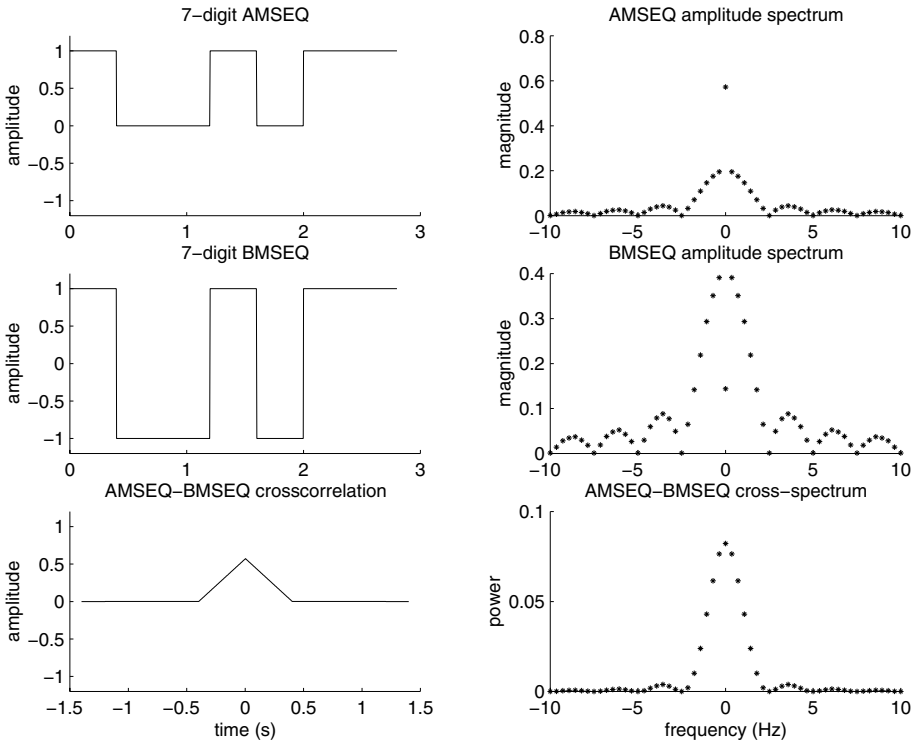

Figure 2.9: AMSEQ-BMSEQ cross-correlation in time domain (left) and frequency domain (right).

three forms (BMSEQ, AMSEQ, CW) of transmission in any desired coherent duration pattern. For instance, BMSEQ may be transmitted continuously with insertions of relatively short periods of AMSEQ or CW.

Pilot signal generation The prs pilot signal can be generated in a signal control computer, by continuously running the shift register sequences synchronized by the UT timing equipment and modulating this onto the desired, UT synchronized carrier wave. The output is to be strobed by the system control computer where it is used as the reaction mass acceleration reference signal. In addition, the derived reaction mass velocity and displacement functions can be generated and used as additional reference signals in a state variable control system. With accurate UT timing, the transmission may be interrupted and resumed coherently, e.g., at the moment another sequence period is supposed to begin. This enables the signal processing, in

particular the stacking and correlation process, to be interrupted and to be continued coherently after transmission resumption. In this way, any number of full sequence periods containing transmission interruption or suspension, or excessive noise, can be coherently omitted.

The above characteristics satisfy the system signal requirements. For instance, for our objectives, we may use a 2.5 Hz carrier frequency with a 5-20 min BMSEQ consisting of one-cycle digits, resulting in a $[\sin(x)/x]^2$ power spectrum with its main lobe centered at 2.5 Hz and extending from zero to five Hz. This signal covers the typical earthquake seismology short-period body-wave frequency range of 1-5 Hz. The spectrum can be extended simply by increasing the carrier wave frequency. Spectral shaping may be obtained by superimposing sequence signals with different carrier frequencies; we leave these experiments for future research.

Conclusion on signals to be emitted

In comparison with the chirp signal, for our objectives the advantages of the prs signals are:

- availability of suites of near-orthogonal (mutually uncorrelated) prs codes, all with identical signal characteristics, allowing simultaneous 3-D signal transmission from different source sites.
- the inherently low side-lobe in the prs BMSEQ autocorrelation function.

A disadvantage is that due to the phase flips, the BMSEQ required reaction mass displacement amplitude or stroke is twice that of the chirp signal for the same peak force at a given minimum frequency and the same amount of signal power emitted. In particular because of the first advantage, and in spite of the BMSEQ stroke disadvantage, the family of prs signals is the preferred choice in meeting our objectives.

As a final remark on signal emission, given the stroke required by BMSEQ, one might be tempted to double the chirp or AMSEQ force signal amplitude and thus quadruple the emitted signal power. Then, however, the reaction mass acceleration also is doubled, and would exceed the acceleration of gravity, causing 'hold-down' problems experienced with existing types of seismic vibrators as will be described in Section 2.4.1.

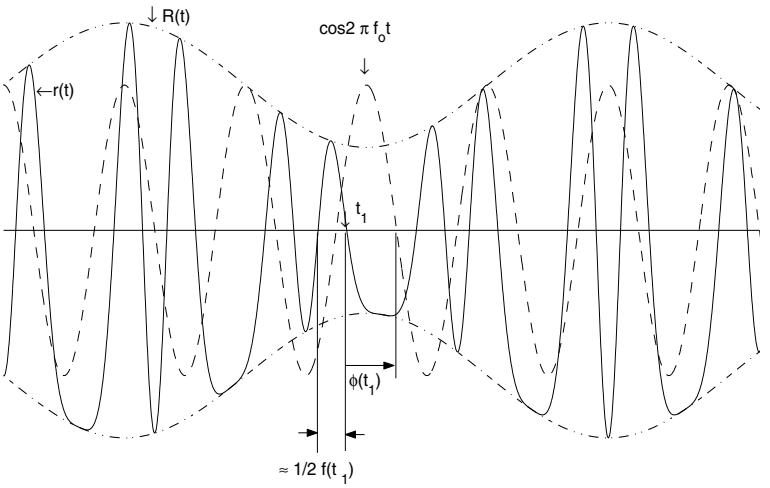

Figure 2.10: Waveform representation in terms of the instantaneous amplitude or envelope $R(t)$, the instantaneous phase ϕ(t), and the instantaneous frequency $f(t)$.

2.2.2 Quadrature processing theory

Since quadrature processing plays an essential role in our application, and apparently sofar has been applied only on rare occasions in seismology, we elaborate to some extent on the definition and specific features of the parameters involved. For that purpose, we reproduce and adapt parts of publications summarizing the use of this technique by the author in previous seismology and underwater acoustics research (Unger, 1981; Unger and Veenkant, 1967a,b).

Parameter definition

Any bandlimited waveform $r(t)$, *not necessarily narrowband*, but with its spectrum not extending down to dc, can be represented in any of the following three *equivalent* forms, see Figure 2.10:

$$r(t) = x(t)\cos(2\pi f_0 t) - y(t)\sin(2\pi f_0 t)\,, \tag{2.3}$$

or

$$r(t) = R(t)\cos\left[2\pi f_0 t + \phi(t)\right]\,, \tag{2.4}$$

or

$$r(t) = R(t)\cos\left[2\pi\int_0^t f(\tau)d\tau\right], \tag{2.5}$$

with the relationships

$$x(t) = R(t)\cos[\phi(t)], \tag{2.6}$$

$$y(t) = R(t)\sin[\phi(t)], \tag{2.7}$$

$$R(t) = \left[x^2(t) + y^2(t)\right]^{\frac{1}{2}}, \tag{2.8}$$

$$\phi(t) = \arctan\left[\frac{y(t)}{x(t)}\right] \pm 2\pi k, \tag{2.9}$$

$$f(t) = \frac{1}{2\pi}\frac{d\phi(t)}{dt} + f_0, \tag{2.10}$$

where

$\{x(t), y(t)\}$ are referred to as the Cartesian or quadrature components,
$R(t)$ is the instantaneous amplitude or envelope,
$\phi(t)$ is the instantaneous phase,
$f(t)$ is the instantaneous frequency,
$f_0(t)$ is any fixed frequency.

Equations (2.6) - (2.9) reflect the familiar Cartesian-to-polar coordinate and vice-versa conversions. Either of the function pairs $\{R(t),\ 2\pi f_0 t + \phi(t)\}$ or $\left\{R(t),\ 2\pi\int_0^t f(\tau)d\tau\right\}$ is known as the *complex envelope* in which $2\pi f_0 t + \phi(t)$ and $2\pi\int_0^t f(\tau)d\tau$ are the *angular argument.* Note that $R(t)$ is independent of the waveform's phase or frequency.

Waveform modulation and demodulation

Modulation concept We may view $R(t), \phi(t), f(t)$ as the amplitude, phase, and frequency *modulation,* respectively, of a, possibly fictitious, carrier wave $\cos 2\pi f_0 t$ with 'carrier' frequency f_0 Hz and zero phase. In *active* transmission, such as radio communication, active radar, etc., a carrier wave is actually present; in *passive* transmission, e.g., in noise or in seismograms generated by earthquakes or explosions, no actual carrier wave is present, but we may invent a fictitious one. Although the carrier frequency f_0 may

be chosen arbitrarily, and even different from an actual carrier frequency if present, it is convenient to choose f_0 either as the actual carrier frequency in active transmission, or as the center of the frequency band of interest in passive transmission. This general waveform representation contains simultaneous amplitude and frequency modulation, Eq. (2.5), or, equivalently, simultaneous amplitude and phase modulation, Eq. (2.4). In line with this, we refer to $\{x(t), y(t)\}$ as the Cartesian modulation, Eq. (2.3).

Demodulation concept The modulating parameters $x(t)$, $y(t)$, $R(t)$, $\phi(t)$ and $f(t)$ can be resolved, i.e., the waveform $r(t)$ *demodulated*, through the *Hilbert transform*, defined as

$$\check{r}(t) = \mathcal{H}\{r(t)\} = \frac{1}{\pi} \int_{-\infty}^{\infty} \frac{r(\tau)}{t-\tau}\, d\tau\,, \tag{2.11}$$

i.e., the *convolution with* $1/\pi t$, and also known as a *quadrature filter* or -90^0 *phase shift operator* (Papoulis, 1965, Schwartz, 1970, Aki and Richards, 1980, Dahlen and Tromp, 1998, Unger, 1981a). Applying the Hilbert transform to the three equivalent expressions for $r(t)$, Eqs. (2.3), (2.4) and (2.5) are transformed into

$$\check{r}(t) = x(t)\sin(2\pi f_0 t) + y(t)\cos(2\pi f_0 t)\,, \tag{2.12}$$

$$\check{r}(t) = R(t)\sin\left[2\pi f_0 t + \phi\,(t)\right]\,, \tag{2.13}$$

$$\check{r}(t) = R(t)\sin\left[2\pi \int_0^t f(\tau) d\tau\right]. \tag{2.14}$$

Equations (2.3) and (2.12) then yield

$$x(t) = r(t)\cos(2\pi f_0 t) + \check{r}(t)\sin(2\pi f_0 t)\,, \tag{2.15}$$

$$y(t) = -r(t)\sin(2\pi f_0 t) + \check{r}(t)\cos(2\pi f_0 t)\,. \tag{2.16}$$

Note that also $\{x\,(t)\,, y\,(t)\}$ form a Hilbert transform pair, which is seen also from Eqs. (2.6) and (2.7):

$$y(t) = \mathcal{H}\{x(t)\}\,, \tag{2.17}$$

$$x(t) = \mathcal{H}\{-y(t)\} = -\mathcal{H}\{y(t)\}\,, \tag{2.18}$$

where the minus sign in the latter compensates for applying the Hilbert transform twice, resulting in a 180° phase shift.

Combining Eqs. (2.4) and (2.13), we obtain the instantaneous amplitude as an alternative expression to Eq. (2.8),

$$R\,(t) = \left[r^2\,(t) + \check{r}^2\,(t)\right]^{\frac{1}{2}}\,, \tag{2.19}$$

and the instantaneous phase as

$$\phi\,(t) = \arctan\left[\frac{\check{r}(t)}{r(t)}\right] \pm 2\pi k - 2\pi f_0 t\,, \quad k = 0, \pm 1, \pm 2, \ldots\,, \tag{2.20}$$

which agrees with Eq. (2.9) if we incorporate the term $-2\pi f_0 t$ in the arctangent argument through trigonometric relations:

$$\phi(t) = \arctan\left[\frac{-r(t)\sin 2\pi(f_0 t) + \check{r}(t)\cos(2\pi f_0 t)}{r(t)\cos(2\pi f_0 t) + \check{r}(t)\sin(2\pi f_0 t)}\right] \pm 2\pi k\,. \tag{2.21}$$

Finally, the combination of Eqs. (2.5) and (2.14) leads to

$$2\pi \int_0^t f(\tau)d\tau = \arctan\left[\frac{\check{r}(t)}{r(t)}\right] \pm 2\pi k\,, \tag{2.22}$$

in agreement also with Eq. (2.10).

Note that the $\arctan\left(\frac{\check{r}(t)}{r(t)}\right) \pm 2\pi k = 2\pi \int_0^t f(\tau)d\tau$ part of Eq. (2.20) reflects the phase with respect to a 'carrier wave' of frequency 0 Hz, i.e., dc. By subtracting $2\pi f_0 t$ we express the phase with respect to the f_0 Hz carrier wave, i.e., we obtain the phase modulation explicitly, allowing greater detail and resolution in the phase variation display. The same is achieved when expressing the phase directly from the Cartesian modulation components as done in Eq. (2.9).

Time-series considerations

The above equations hold for continuous waveforms. In our case, the waveforms have been digitized at the receiving station, presumably after passing the waveform through an anti-alias filter, and sampling it at the Nyquist or higher frequency, the Nyquist frequency f_N being equal to twice the highest bandpass frequency $f_{\max}$. In all of the above equations, therefore, we may assume t to represent discrete time points spaced uniformly at sample intervals Δt, and replacing integration by summation, and differentiation

by taking first differences, thus expressing the parameters involved as discrete time-series. Now, in equations determining the angular arguments, the time-series of these angular arguments is bounded by $\pm\pi$, and contains the term $\pm 2\pi k$ of angular argument ambiguity causing step functions in this time-series, and artificial spikes in the time-series of its first differences.

Phase unwrapping algorithm We resolve the $\pm 2\pi k$ ambiguity, by 'unwrapping' the phase time-series bounded by $\pm\pi$ radians as follows. Adjacent Nyquist samples, and certainly closer spaced samples, cannot differ more than π radians; this follows from

$$\Delta t \leq \frac{1}{f_N} = \frac{1}{2f_{max}}\,, \tag{2.23}$$

$$|\Delta\phi| \leq 2\pi f_{max}\Delta t = \pi\,. \tag{2.24}$$

Thus, we accumulatively add 2π radians at 'discontinuities' less than $-\pi$ radians, and subtract 2π radians at 'discontinuities' greater than $+\pi$ radians. The result is the *unambiguous* 'unwrapped' or 'continuous' time-series of the instantaneous phase with respect to the 'carrier wave' of frequency f_0 and zero phase. Step functions in this time-series now reflect actual signal discontinuities caused by new signal arrivals or noise.

Computing the instantaneous frequency The instantaneous frequency time-series is obtained by taking first differences of the unwrapped phase time-series:

$$f(t_k) = \frac{\phi(t_k) - \phi(t_{k-1})}{2\pi\Delta t}\,. \tag{2.25}$$

So, there is no need for first deriving the closed-form expression for the instantaneous frequency explicitly as a function of t by expanding Eq. (2.10) and carrying out the actual differentiation of $\phi\,(t)$ as given by Eqs. (2.9), (2.20), or (2.21). Like the step functions in the 'continuous' instantaneous phase, any spikes in the instantaneous frequency time-series explicitly reflect new signal arrivals or noise.

The complex-envelope seismogram

The above aspects are illustrated in Figure 2.11 showing complex-envelope seismograms of three different types of seismic events. In addition, the figure displays automatic signal detection and timing (vertical dotted lines)

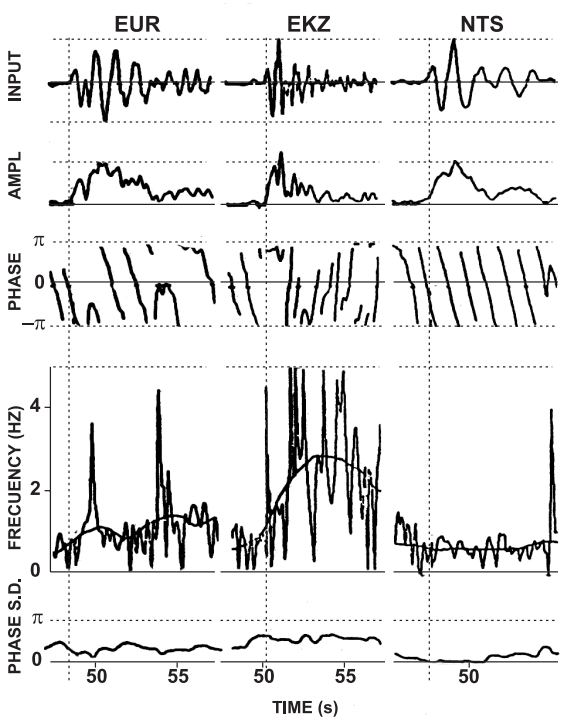

Figure 2.11: Traditional and complex-envelope seismograms for a Eurasian earthquake (EUR), an Eastern Kazakh presumed underground nuclear explosion (EKZ), and a Nevada Test Site (NTS) presumed underground nuclear explosion. The time indication is relative to the seismogram record start time (Unger, 1981a).

obtained from an envelope detector algorithm, the instantaneous mean frequency (solid curve in the instantaneous frequency time series), and the phase standard deviation (lower trace). The instantaneous mean frequency is computed as the closed-form time derivative of the instantaneous mean phase polynomial obtained by moving-window second order regression on the time-series of the unwrapped instantaneous phase. The phase standard deviation is measured as the residue in this regression. The phase standard deviation is a measure of pulse complexity which, in relation to seismic event magnitude, has been found to be a strong contributor in earthquake versus underground explosion discrimination in the context of Nuclear Test Ban Treaty seismic verification methods. The pulse complexity appears to reflect local rock-fracturing properties. In all, it is clear that the complex-envelope parameters are important quantities in seismic signal detection, signal tim-

ing, and any kind of signal analysis. This research has been reported in earlier publications (Unger, 1981a,b).

Vector diagram representation

Vector diagram definition In view of the equations and concepts presented in the previous subsection, we may study the behavior of the waveform $r\,(t)$ at any instant as that of a vector or phasor $\mathbf{r}\,(t)$ with polar coordinates

$$|\mathbf{r}(t)| = R(t)\,, \tag{2.26}$$

and

$$\arg[\mathbf{r}(t)] = 2\pi \int_0^t f(\tau)d\tau = 2\pi f_0 t + \phi(t), \tag{2.27}$$

or Cartesian coordinates $\{r(t), \check{r}(t)\}$ in a vector diagram representation with respect to dc. If we want to study amplitude and phase *variation*, the term of constant rotation $2\pi f_0 t$ in the latter expression is irrelevant, and may be omitted, resulting in the *demodulated* complex-envelope vector diagram representation of Figure 2.12 rotating with angular velocity $\omega_0 = 2\pi f_0$. Then, $\mathbf{r}_d(t)$, with polar coordinates $\{R(t), \phi(t)\}$ and Cartesian coordinates $\{x(t), y(t)\} = \{R(t)\cos\phi(t), R(t)\sin\phi(t)\}$ represents the behavior of the receiver *demodulated waveform*, i.e., with respect to f_0.

Signal detection aspects Vector diagram representation is illustrative in signal detection and in multiple signal analysis (Unger, 1981a). Figure 2.13 shows the vector diagrams for three signal-to-noise ratio (snr) cases, where $\mathbf{n}$ is the noise vector and $\mathbf{s}$ is the signal vector. We study the behavior of the signal-plus-noise waveform envelope vector $\mathbf{r}$. For a given snr, the instantaneous phase angle ϕ of the signal-plus-noise envelope vector depends on the instantaneous noise phase angle ϕ_n with respect to the signal phase. We observe that in the case of snr ≥ 1, the signal-plus-noise envelope phase excursions are limited to maximum values $|\phi_{\max}|$ as indicated in the figure. From vector diagram geometry we find

$$|\phi_{\max}|_{\text{snr}>1} = \arcsin\left(\frac{|\mathbf{n}|}{|\mathbf{s}|}\right) = \arcsin\left(\frac{1}{\text{snr}}\right), \tag{2.28}$$

and

$$|\phi_{\max}|_{\text{snr}=1} = \frac{\pi}{2}\,. \tag{2.29}$$

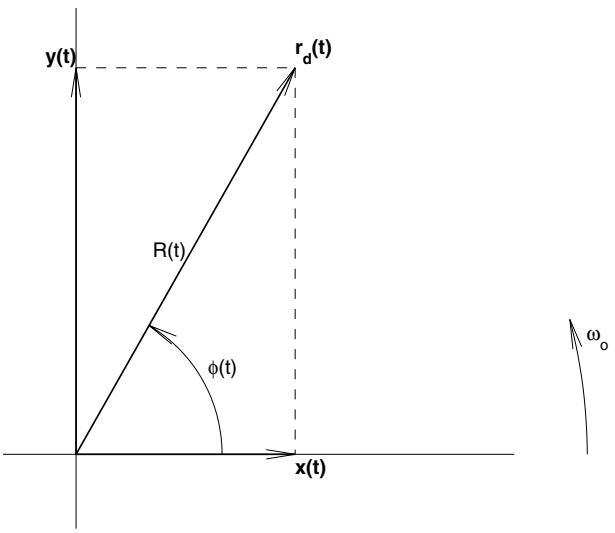

Figure 2.12: Demodulated waveform vector diagram representation.

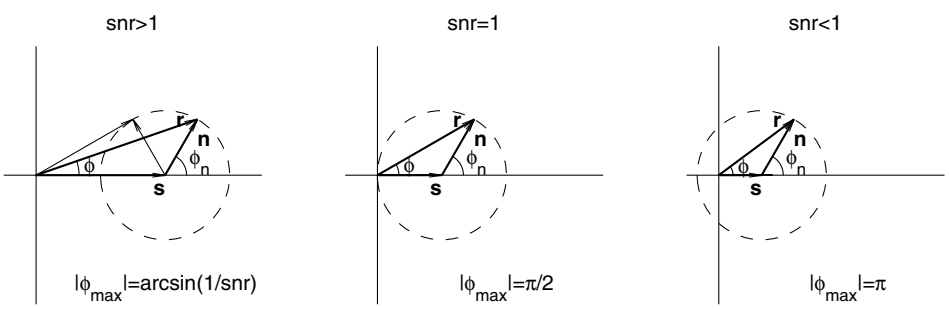

Figure 2.13: Vector diagram representations of signal and noise interaction. Without loss of generality, the signal reference phase is taken as zero (Unger, 1981a). The dashed circles are the loci of noise vector end points for random noise phase angles for the given snr. In the snr > 1 figure, the vector tangential to the dashed circle has maximum phase; for snr $= 1$, the tangential is the positive Y axis.

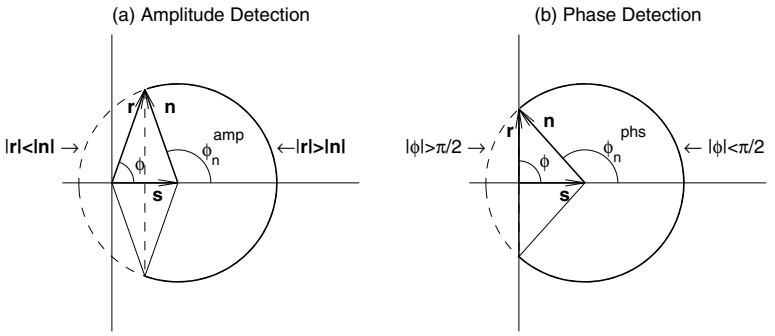

Figure 2.14: Vector diagram geometry for envelope and phase detection (Unger, 1981).

In the case of snr < 1, ϕ can take on any value on $[-\pi, \pi]$.

In all snr cases, with the exception of snr $= 0$, *the distribution of* ϕ *is biased*, and even an infinitesimally small signal component will influence the signal-plus-noise envelope phase distribution. This suggests the feasibility of detecting signals in noise by means of a phase bias detection method. In Figure 2.14, we compare amplitude and phase detection methods. Figure 2.14a represents the intuitive, and usually applied amplitude detection method requiring that the signal-plus-noise envelope modulus is greater than the noise-only envelope modulus. At each instant, for a given snr, the probability that the signal-plus-noise envelope is greater than the noise-only envelope, $\Pr(|\mathbf{r}| > |\mathbf{n}|)$, depends on the noise-phase-minus-signal-phase angle, and in the figure equals the ratio of solid arc over full circle arc, this ratio equals ϕ_n^{amp}/π. In Figure 2.14b, the same holds for the probability that the signal-plus-noise instantaneous phase is biased, for instance as $|\phi| < \pi/2$, but now the solid arc is larger, and thus the probability of signal detection by this phase bias method, $\Pr(|\phi| < \pi/2) = \phi_n^{phs}/\pi$, is greater than the above probability of amplitude detection. Vector diagram geometry leads to analytic expressions for the probabilities of amplitude detection and this phase bias detection as functions of signal-to-noise ratio:

$$\Pr(|\mathbf{r}| > |\mathbf{n}|) = 1 - \pi^{-1} \arccos\left(\frac{|\mathbf{s}|}{2\,|\mathbf{n}|}\right), \tag{2.30}$$

$$\Pr(|\phi| < \pi/2) = 1 - \pi^{-1} \arccos\left(\frac{|\mathbf{s}|}{|\mathbf{n}|}\right), \tag{2.31}$$

see Figure 2.15. Note the factor two difference in the arccosine snr argument

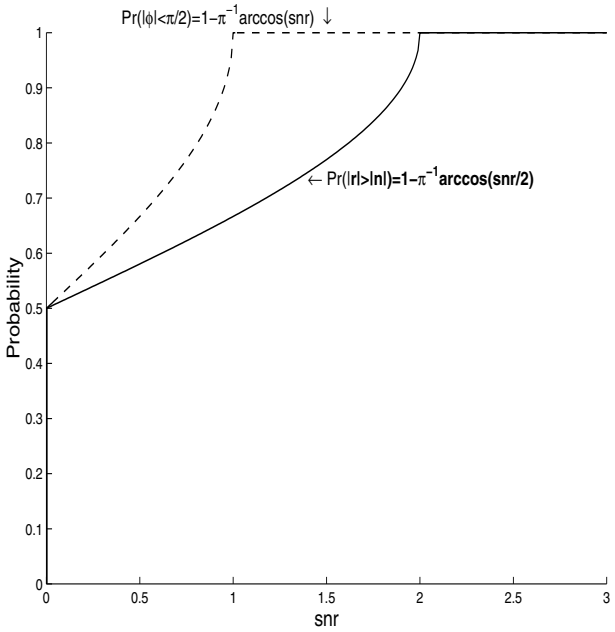

Figure 2.15: The probability distribution functions for amplitude detection (solid curve) and phase bias detection (dashed curve).

in favor of the phase bias detection probability, indicating that this phase bias detection method is roughly 6 dB more sensitive than the intuitive amplitude detection method. Of course, it can be argued that our choice of phase bias criterion, $|\phi| < \pi/2$, is arbitrary. For instance, if we choose a phase bias criterion of $|\phi| < \phi_n^{amp}$ with ϕ_n^{amp} as in Figure 2.14a, the probabilities of signal detection by the amplitude and the phase bias criteria would be identical. In order to see which method is better, signal detection tests would have to be performed, applying both methods to the same suite of snr cases, showing detection success versus false alarm rate for each method. Such experiments are left for future research.

The strong phase detection sensitivity relative to amplitude detection sensitivity is apparent in overlays of coherent ocean acoustics BMSEQ transmission complex-envelope correlograms (Steinberg and Birdsall, 1966; Unger and Veenkant, 1967a), where distinct multipath signal arrivals are clearly visible as a bias in the coda of the correlogram's instantaneous phase, whereas the coda in the instantaneous amplitude trace is virtually indistinguishable from noise (Figure 2.16).

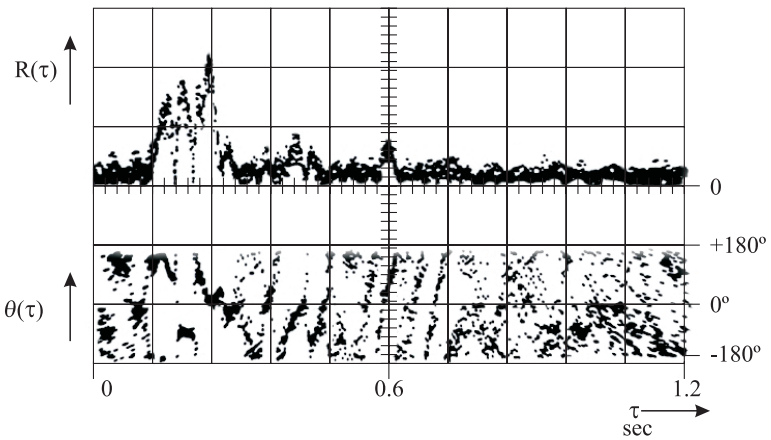

Figure 2.16: Ensembles of underwater acoustics complex-envelope correlograms showing the relatively strong signal detectability by the instantaneous phase as compared to the instantaneous amplitude (Unger and Veenkant, 1967a).

Multiple signal arrivals result in principle in stepfunctions in the instantaneous amplitude and in the instantaneous phase (Figure 2.17), and spikes in the instantaneous frequency. However, the instantaneous phase contains more information in a given bandwidth than does the instantaneous amplitude, given the fact that adjacent Nyquist phase samples can differ by as much as π radians whereas the amplitude variation is limited by the bandpass of the original waveform $r(t)$. This is also reflected by the known higher efficiency, fidelity, and noise rejection of FM over AM radio transmission. For this reason, the mentioned stepfunctions due to multiple signal arrivals materialize as such in the instantaneous phase, but become smooth (bandlimited) transitions in the instantaneous amplitude time-series, as seen in Figures 2.11 and 2.16.

Phase resolution benefits

The detection sensitivity and broad-band features of the instantaneous phase are greatly beneficial in direct and time-lapse signal arrival timing, multiple signal analysis, and analysis of time-lapse coda variation reflecting changes in Earth heterogeneity and anisotropy. Time-lapse signal variation may reflect earthquake precursory behavior somewhere along the wave propagation path. Signal arrival time variation due to changes in wave propagation ve-

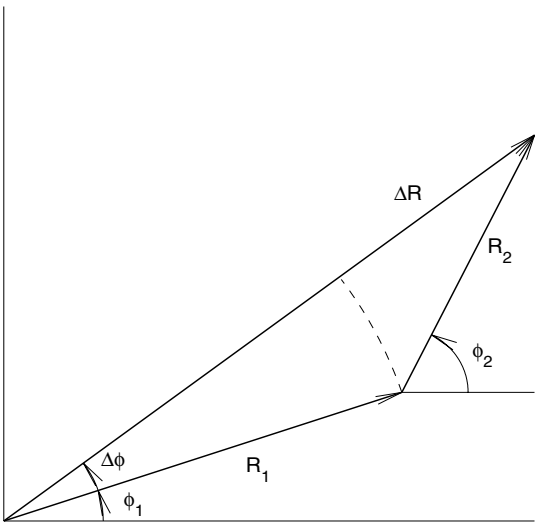

Figure 2.17: Vector diagram representation of secondary signal interaction, resulting in step functions in amplitude (ΔR) and in phase ($\Delta\phi$).

locity is believed to be one of the prime potential earthquake precursors. Below, we give an example of attainable timing resolution with ensuing stability requirements for the signal source.

In a 32-bit computer, the phase can in principle be computed with a resolution of $\pm 2^{-31}\pi = 1.4629 \times 10^{-9}$ radians, resulting, for our projected 2.5 Hz, 0.4 s period carrier wave, in $\frac{\pm 2^{-31}\pi}{2\pi} \times 0.4$ s ≈ 0.1 nanosecond timing resolution. Naturally, because of noise, i.e., waveform noise as well as natural parameter variation, and algorithm and round-off errors, this ideal resolution will not be feasible. In Section 2.25 we consider the effect of waveform noise on the accuracy of signal arrival times obtained from matched filter complex-envelope correlograms. It is clear, however, that source signal stability, and especially signal phase stability, is of utmost importance in order to take full advantage of the phase resolution attainable in quadrature signal processing.

Matched filtering

In matched filtering (MF) or correlation filtering, the waveform to be processed is correlated with a noise-free replica of the emitted signal (the 'pilot' signal). According to seismic wave propagation theory, the far-field particle

displacement is proportional to the source force. Therefore, MF should consist of correlating the particle displacement waveform received at a seismic station with the noise-free source force signal. In quadrature processing and demodulation, also known as *coherent processing,* each of the particle displacement quadrature components, i.e., each of the Cartesian demodulation components $x(t), y(t)$, is correlated with the force modulating signal code. The two Cartesian correlograms then are converted into the polar form, resulting in the complex-envelope seismogram consisting of the correlogram dual time-series of instantaneous amplitude and instantaneous phase.

In white noise, the MF output power signal-to-noise ratio equals the ratio of signal energy over noise power density (Papoulis, 1991). In formula, with $S(f)$ the signal power density spectrum received at a seismic station, T the total signal transmission and stacking time, W the signal frequency band, and N_0 the noise power density:

$$\left|\frac{\mathbf{s}}{\mathbf{n}}\right|^2 = \frac{T\int_W S(f)df}{N_0}. \tag{2.32}$$

In the case of colored noise, with noise power density spectrum $N(f)$ and average power density N_0, the MF output signal-to-noise ratio is arrived at by filtering the signal-plus-noise waveform such that the noise becomes white (noise 'whitening'), resulting in

$$\left|\frac{\mathbf{s}}{\mathbf{n}}\right|^2 = \frac{T\int_W \frac{S(f)}{N(f)}df}{N_0}. \tag{2.33}$$

For a slope α in a generic log-power versus log-frequency displacement noise spectrum, we may describe the noise power density spectrum by $N(f) = N_0 f^{\alpha}$, leading to the MF output power signal-to-noise ratio

$$\left|\frac{\mathbf{s}}{\mathbf{n}}\right|^2 = \frac{T\int_W f^{-\alpha}S(f)df}{N_0}. \tag{2.34}$$

For instance, if the noise spectrum is like the ones shown in Figure 2.18, in the frequency range 1-10 Hz to be used in our system, the particle velocity noise decreases at a rate of 20 dB/decade, i.e., second order. The displacement noise then decreases third order, $\alpha = -3$, and the MF output power snr integrand increases with f^3.

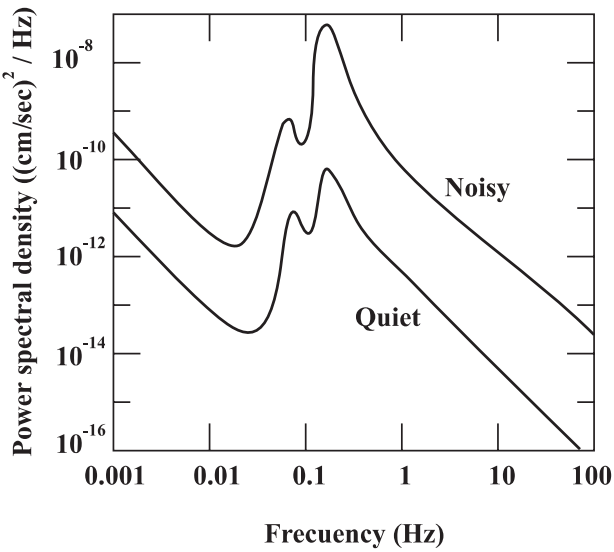

Figure 2.18: Power spectra of ambient seismic particle velocity noise at noisy and quiet conditions for a typical station on hard basement rock (Aki and Richards, 1980).

In body wave ray theory for an anelastic, smoothly varying isotropic medium, the Green function is subject to the source radiation pattern, to geometric spreading, to reflection/transmission coefficient attenuation, to an exponential amplitude attenuation factor $\exp\left(-\pi f r/c\left(f\right)Q\right)$ for each of the frequencies f in the signal pass band, and to attenuation-associated dispersion. Here, r is the raypath range, $c\left(f\right)$ is the frequency-dependent propagation speed, and Q is the propagation quality factor considered frequency-independent when allowing for dispersion. For two different frequency components f_1, f_2 this dispersion is given by (Aki & Richards, 1980):

$$\frac{c(f_1)}{c(f_2)} = 1 + \frac{1}{\pi Q} \ln\left(\frac{f_1}{f_2}\right) . \tag{2.35}$$

The frequency components arrival time dispersion is

$$|\Delta t| = \left|\frac{r}{c} - \frac{r}{c+\Delta c}\right| = \frac{r}{c}\left|1 - \frac{1}{1+\Delta c/c}\right| \approx \frac{r}{c} \times \frac{|\Delta c|}{c} , \tag{2.36}$$

where

$$|\Delta c| = |c(f_1) - c(f_2)| , \tag{2.37}$$

and

$$\left|\frac{\Delta c}{c}\right| = \left|\frac{1}{\pi Q}\ln\left(\frac{f_1}{f_2}\right)\right|. \tag{2.38}$$

For the $\sin(x)/x$ amplitude spectrum of our suggested 2.5 Hz carrier wave pseudo-random sequence transmission, with its main energy between 1 and 4 Hz, and assuming, for instance, $Q = 250$, we have less than 0.2% velocity change over this frequency range, leading to a frequency components arrival time dispersion of

$$|\Delta t| < \frac{r}{c} \times 2 \text{ ms}, \tag{2.39}$$

e.g., $c = 5$ km/s results in $|\Delta t| < 40$ ms per 100 km wave propagation path length, and an accordingly broadening of the signal pulse.

Neglecting the dispersion effect, denoting the source force amplitude by $\hat{F}$ and the source force signal power density spectrum by $F(f)$, approximating the amplitude geometric spreading factor by r^{-1}, and lumping the radiation pattern and transmission/reflection effects into a single proportionality factor K, the above considerations lead to a generic formula for the MF output power snr:

$$\left(\frac{|\mathbf{s}|}{|\mathbf{n}|}\right)^2 = K\hat{F}^2 r^{-2} T \int_{f_1}^{f_2} f^{-\alpha} F(f) \exp\left(-\frac{2\pi f r}{cQ}\right) df\,. \tag{2.40}$$

Note that for $\alpha < 0$, at some point, depending on the transmission parameters α, f, r, c, Q, the apparent benefit of increasing snr with frequency due to the factor $f^{-\alpha}$ is compensated and overcome by the greater exponential attenuation with increasing frequency. Thus, the transmission can be optimized with respect to these parameters. For instance, for media with relatively high attenuation, the attainable transmission range is increased by lowering the transmission frequency, demonstrating the importance of creating the capability of emitting low-frequency seismic waves. In the Earth propagation subsection 2.4.2, we will elaborate on this, and, from existing seismic vibrator experiments extrapolate estimates of attainable transmission range versus signal transmission time for various parameter combinations, see Figure 2.31.

In quadrature processing, one has the choice of either first obtaining the demodulated quadrature components, i.e., the Cartesian components, through the Hilbert transform, and performing the correlation on each of these components, or first performing the correlation and then applying the

quadrature processing. In general, the first option is preferred, because all further signal processing is applied to the relatively slowly varying modulating and demodulated signals, allowing a lesser sampling rate and, therefore, saving computer time and memory. In our system, moreover, the emitted signal is a pseudo-random binary sequence (prs) code consisting of $\{+1, -1\}$ or $\{1, 0\}$ digits modulated onto a low-frequency carrier wave. Thus, the pilot signal to correlate the demodulated waveform with, is the modulating waveform, i.e., the given pseudo-random sequence of either ones and minus ones, or ones and zeros. The first alternative, demodulation followed by matched filtering, then has the additional advantage that the correlation process comes down to, respectively, a series of additions and subtractions for the $\{+1, -1\}$ sequence, or a series of additions only in the case of the $\{1, 0\}$ sequence. We will adopt this technique, originally used in the underwater acoustics project mentioned (Steinberg and Birdsall, 1966; Unger and Veenkant, 1967a) in our signal processing procedure.

Thus, we will first obtain the Cartesian components $\{x(t), y(t)\}$, and correlate each with the pilot signal $\{1, -1\}$ or $\{1, 0\}$ prs pattern, followed by converting the resulting quadrature correlograms into the polar correlograms of instantaneous amplitude and instantaneous phase. The result is the desired complex-envelope seismogram; its length equals the prs duration or period. Detection and timing of primary and later seismic phases now is achieved with the technique described in Subsection 2.2.4.

2.2.3 Alternative quadrature component processing

So far, our development has been based on the formal Hilbert transform to provide quadrature signal components. Usually, the Hilbert transform is obtained via the fast Fourier transform of a given signal time window, frequently requiring window tapering in order to avoid window edge effects. Below, we briefly describe an alternative method for obtaining quadrature signal components by sampling exactly at four times the carrier wave frequency. This method, developed in the afore mentioned underwater acoustics project, and described in detail in a technical report (Unger and Veenkant, 1967a), avoids the windowing problem altogether, saves considerable amounts of computer time, and allows processing to be carried out continuously from one data record into the next. We adopt this algorithm in our further signal processing development.

We repeat the representation of the received signal, Eq.(2.3):

$$r(t) = x(t)\cos(2\pi f_0 t) - y(t)\sin(2\pi f_0 t)\,, \tag{2.41}$$

and substitute

$$t = t_k = \frac{k}{4f_0},\ k = 0, 1, \ldots\,, \tag{2.42}$$

resulting in

$$r(t_k) = x(t_k)\cos\Big(k\frac{\pi}{2}\Big) - y(t_k)\sin\Big(k\frac{\pi}{2}\Big)\ , \tag{2.43}$$

and yielding the Cartesian components as

$$\begin{aligned} x\,(t_k) &= r\,(t_k)\,,\ k = 0, 4, 8, \ldots\,, \\ x\,(t_k) &= -r\,(t_k)\,,\ k = 2, 6, 10, \ldots\,, \\ y\,(t_k) &= -r\,(t_k)\,,\ k = 1, 5, 9, \ldots\,, \\ y\,(t_k) &= r\,(t_k)\,,\ k = 3, 7, 11, \ldots\,. \end{aligned} \tag{2.44}$$

Following this Cartesian demodulation process, the matched filter processing is carried out on each of the Cartesian component time series separately. The Cartesian match filter outputs then are converted into the time series of the instantaneous amplitude and the instantaneous phase constituting the complex-envelope seismogram. For our proposed transmission of prs modulated signals with prs digit length equal to one carrier wave period, signal arrivals in the matched filter output will be recognizable by three-point triangular correlation peaks in the instantaneous amplitude time series, and, because of phase bias due to signal presence, as three-point clusters in ensembles of the instantaneous phase time series, or, consequently, as three-point minima in the time series of the ensemble's phase s.d. We use these features to develop a novel signal detection and timing algorithm, as described below.

2.2.4 A novel signal detection and timing algorithm

With the considerations above, we now are able to construct an efficient and accurate, *novel* signal detection and timing algorithm, operating on a number of MF output records forming a coherent *ensemble* of complex-envelope correlograms, as follows.

- Compile a synchronized ensemble of coherent correlograms.

- At each lag in the time-series of the instantaneous phase correlogram, determine the *ensemble* phase standard deviation (PSD).
- PSD *minima* below a set threshold reflect signal arrivals.
- Determine either the ensemble phase mean or the ensemble phase median (PMN) for the ensemble of phase values at the lag time index of minimum PSD.
- relative signal arrival time = time of PSD minimum + (PMN/2π) $\times$ carrier wave period.

In this procedure, there is a trade-off between the desired total averaging time, or the number of signal records per MF input stack, and the desired number of MF output records or correlograms per ensemble. On the one hand, the snr in each correlogram increases with the square root of the number of records per MF input stack. On the other hand, a greater number of correlograms yields better statistics, in particular for the analysis of the behavior of potential earthquake precursor parameters. The maximum total raw data stacking time is determined by the minimum amount of elapsed time in which Earth parameter variation is expected to take place, the minimum number of correlograms is determined by a minimum statistics criterion, e.g., at least ten correlograms per ensemble. In signal detection applications, the trade-off is a general problem of averaging procedures versus "counting" procedures. In our case, it seems prudent to put priority on satisfying the sufficient statistics criterion and relatively "short " time-lapse windows; after all, the correlogram snr always can be further increased by stacking the MF output correlograms in addition to MF input record stacking. In this way, we obtain greater flexibility in signal processing and in moving-window time-lapse parameter analysis.

2.2.5 Signal arrival time error analysis

For the signal detection and timing algorithm described above, we now perform signal arrival time error analysis in two ways: (1) in closed form, from the uniform distribution of the noise phase angle in normally distributed noise; (2) empirically, by adding normally distributed random noise to the modulated waveform and applying, respectively, quadrature demodulation, matched filtering, and our new signal detection and timing algorithm as described in the previous section.

Closed-form analysis

From the vector diagram geometry given in Section 2.2.2, Figures 2.13 and 2.14, we derive a closed-form relationship between signal timing error and signal-to-noise ratio. We consider the triangles formed by the signal, noise, and envelope vectors $\mathbf{s}, \mathbf{n}, \mathbf{r}$, with sides $s = |\mathbf{s}|$, $n = |\mathbf{n}|$, $r = |\mathbf{r}|$. The signal timing error is directly related to the distribution of the instantaneous phase ϕ of the signal-plus-noise waveform; ϕ depends on the snr s/n and on the noise instantaneous phase angle ϕ_n. Given the probability distribution of ϕ_n, and knowing the relation between ϕ and ϕ_n, we arrive at the ϕ distribution through transformation of the ϕ_n distribution, by applying the *fundamental theorem* of probability density function transformations (Papoulis, 1965, p. 126).

According to this theorem, the probability density function of ϕ follows from the probability density function of ϕ_n by

$$f_{\phi}(\phi) = \frac{f_{\phi_n}((\phi_n)_1)}{|g'((\phi_n)_1)|} + \frac{f_{\phi_n}((\phi_n)_2)}{|g'((\phi_n)_2)|} + ... + \frac{f_{\phi_n}((\phi_n)_m)}{|g'((\phi_n)_m)|}, \tag{2.45}$$

where $(\phi_n)_1$, $(\phi_n)_2$, ..., $(\phi_n)_m$ are all of the *real* roots of $\phi = g(\phi_n)$, and $g'((\phi_n)_i)$ is the derivative of $\phi = g(\phi_n)$ with respect to ϕ_n, evaluated at the root $(\phi_n)_i$.

We first derive the forward and inverse relations $\phi = g(\phi_n)$, $\phi_n = g^{-1}(\phi)$ for a given snr s/n by applying the trigonometric law of cosines twice in the triangles of Figure 2.13:

$$r^2 = s^2 + n^2 - 2sn\cos(\pi - \phi_n) \text{ or } r^2 = s^2 + n^2 + 2sn\cos(\phi_n), \tag{2.46}$$

$$n^2 = r^2 + s^2 - 2rs\cos(\phi) \quad \text{or} \quad r^2 = -s^2 + n^2 + 2rs\cos(\phi), \tag{2.47}$$

and subtracting the expressions on the right:

$$0 = 2s^2 + 2sn\cos(\phi_n) - 2rs\cos(\phi), \tag{2.48}$$

from which follows

$$\cos(\phi) = \frac{s/n + \cos(\phi_n)}{(r/n)}. \tag{2.49}$$

From Eq. (2.46) we obtain

$$r/n = \sqrt{(s/n)^2 + 1 + 2(s/n)\cos(\phi_n)}, \tag{2.50}$$

where, since r and n are positive values, we have maintained only the positive root.

Equation (2.50) transforms Eq. (2.49) into

$$\cos(\phi) = \frac{s/n + \cos(\phi_n)}{\sqrt{(s/n)^2 + 1 + 2(s/n)\cos(\phi_n)}}\,, \tag{2.51}$$

or

$$\phi = \arccos\left(\frac{s/n + \cos(\phi_n)}{\sqrt{(s/n)^2 + 1 + 2(s/n)\cos(\phi_n)}}\right), \tag{2.52}$$

so that now indeed, the signal-plus-noise waveform phase angle ϕ is a function of the snr s/n and the noise phase angle ϕ_n. We remark that in the denominator, the square root argument equals zero only in the case that

$$s/n = 1 \text{ and } \phi_n = \pm\pi\,, \tag{2.53}$$

in all other cases it is definite positive, as shown by

$$\begin{aligned}(s/n)^2 + 1 + 2(s/n)\cos(\phi_n) &= [s/n + \cos(\phi_n)]^2 + 1 - \cos^2(\phi_n) \\ &= [s/n + \cos(\phi_n)]^2 + \sin^2(\phi_n) > 0\,.\end{aligned} \tag{2.54}$$

Inversely, Eq. (2.51) yields

$$\cos(\phi_n) = \sqrt{(s/n)^2 + 1 + 2(s/n)\cos(\phi_n)}\,\cos(\phi) - s/n\,, \tag{2.55}$$

or

$$\cos(\phi_n) + s/n = \sqrt{(s/n)^2 + 1 + 2(s/n)\cos(\phi_n)}\,\cos(\phi)\,, \tag{2.56}$$

from which we obtain, after quadratizing, the possible solutions

$$\cos(\phi_n)_1 = -(s/n)\sin^2(\phi) + \cos(\phi)\sqrt{1 - (s/n)^2\sin^2(\phi)}\,, \tag{2.57}$$

$$\cos(\phi_n)_2 = -(s/n)\sin^2(\phi) - \cos(\phi)\sqrt{1 - (s/n)^2\sin^2(\phi)}\,. \tag{2.58}$$

Since quadratizing Eq. (2.56) may have introduced a fictitious solution, we must check these solutions for validity. We do this by considering the special case where $s/n = 1$, see Figure 2.13b, resulting in

$$\cos(\phi_n)_1 = -\sin^2(\phi) + \cos^2(\phi) = \cos(2\phi)\,, \tag{2.59}$$

i.e., for all values of the noise phase angle ϕ_n, the signal-plus-noise envelope vector $\mathbf{r}$ is in the direction of the bisectrix of ϕ_n, a valid solution, in agreement also with a theorem in plane geometry. For the second solution follows, for $s/n = 1$,

$$\cos(\phi_n)_2 = -\sin^2(\phi) - \cos^2(\phi) = -1\,, \tag{2.60}$$

which would lead to $\phi_n = \pm\pi$ for all values of ϕ. Clearly, this cannot be the case, so we reject the second solution, leaving

$$\phi_n = \arccos\left[-(s/n)\sin^2(\phi) + \cos(\phi)\sqrt{1-(s/n)^2\sin^2(\phi)}\right] \tag{2.61}$$

as the only root of $\phi = g(\phi_n)$.

Next, we must investigate if this root is real. This is the case if

$$s/n \leq 1\,, \tag{2.62}$$

or if

$$s/n > 1 \text{ and } |\sin(\phi)| \leq 1/(s/n)\,. \tag{2.63}$$

The second condition in the latter equation is always satisfied, as can be seen from vector diagram geometry, Figure 2.13a, since for $s/n > 1$ the maximum value for the signal-plus-noise phase angle equals

$$|\phi_{\max}| = \arcsin(n/s)\,. \tag{2.64}$$

Thus, the root ϕ_n is real for all signal-to-noise ratios, and for all values $-\pi \leq \phi_n \leq \pi$.

Assuming normally distributed noise, the noise phase angle ϕ_n *is uniformly distributed* between $-\pi$ and π, so that

$$f_{\phi_n}(\phi_n) = \frac{1}{2\pi}\,. \tag{2.65}$$

For the derivative of $g(\phi_n)$ with respect to ϕ_n we find

$$|g'(\phi_n)| = \left|\frac{1+(s/n)\cos(\phi_n)}{(s/n)^2+1+2(s/n)\cos(\phi_n)}\right|, \tag{2.66}$$

leading to

$$f_{\phi}(\phi) = \frac{1}{2\pi}\left|\frac{(s/n)^2+1+2(s/n)\cos(\phi_n)}{1+(s/n)\cos(\phi_n)}\right|, \tag{2.67}$$

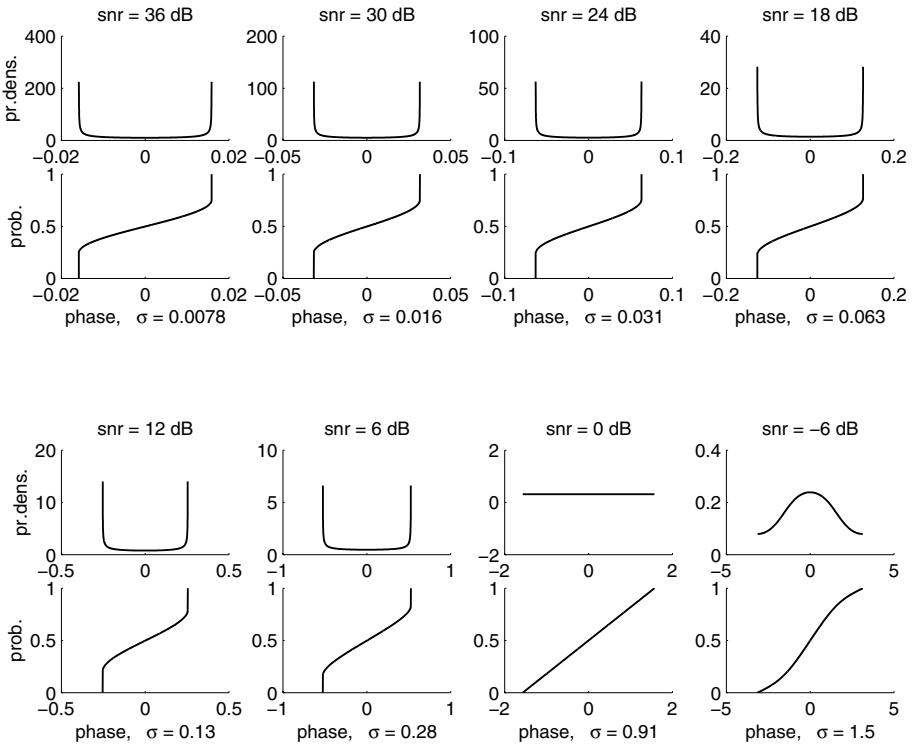

Figure 2.19: Analytically determined probability functions and standard deviations σ for the instantaneous phase of the signal-plus-noise waveform for various signal-to-noise ratios.

in which

$$\cos(\phi_n) = -(s/n)\sin^2(\phi) + \cos(\phi)\sqrt{1-(s/n)^2\sin^2(\phi)}\,, \tag{2.68}$$

with $|\phi| < \pi$ for $s/n < 1$ and $|\phi| < \arcsin[1/(s/n)]$ for $s/n \geq 1$.

To check these relations, we consider some special cases. First, for $s/n = 1$,

$$f_{\phi}(\phi) = \frac{1}{2\pi}\left|\frac{2+2\cos(\phi_n)}{1+\cos(\phi_n)}\right| = \frac{1}{\pi}\,, \tag{2.69}$$

independent of ϕ_n, i.e., for the uniform distribution of the noise phase angle between $-\pi$ and π, the signal-plus-noise phase angle is uniformly distributed between $-\frac{\pi}{2}$ and $\frac{\pi}{2}$, in agreement with Figure 2.13b, and $\phi = \phi_n/2$ as found

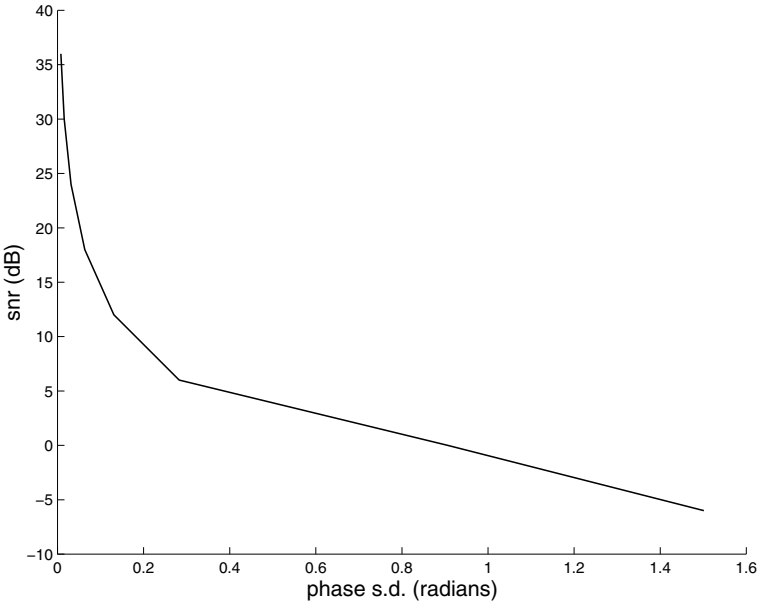

Figure 2.20: Analytically determined signal-plus-noise instantaneous phase standard deviation vs. signal-to-noise-ratio.

from Eq. (2.59). For $s/n = 0$, we have $\phi = \phi_n$ so that $f_{\phi}(\phi) = f_{\phi_n}(\phi_n) = 1/2\pi$, in agreement with Eq. (2.67). In all other snr cases, the distribution of ϕ is non-uniform. Finally, in the limit as $s/n \to \infty$, $\phi \to 0$ so that

$$\lim_{s/n \to \infty} f_{\phi}(\phi) = \delta(0)\,. \tag{2.70}$$

The probability density functions, probability distribution functions, and the resulting phase standard deviations σ of the signal-plus-noise waveform instantaneous phase ϕ for several snr cases are given in Figures 2.19, 2.20. For high signal-to-noise ratios,

$$|\phi_{\max}| = \arcsin(\mathrm{snr}^{-1}) \approx \mathrm{snr}^{-1}, \tag{2.71}$$

so that also the phase standard deviation increases near-linearly with snr^{-1}, as seen in the σ values annotated in Figure 2.19. For snr < 6 dB, σ appears to increase log-linearly with snr^{-1}, as shown in Figure 2.20.

For the transmission signal proposed, i.e., a BMSEQ pseudo-random sequence consisting of one-cycle digits, modulated onto a 2.5 Hz carrier wave,

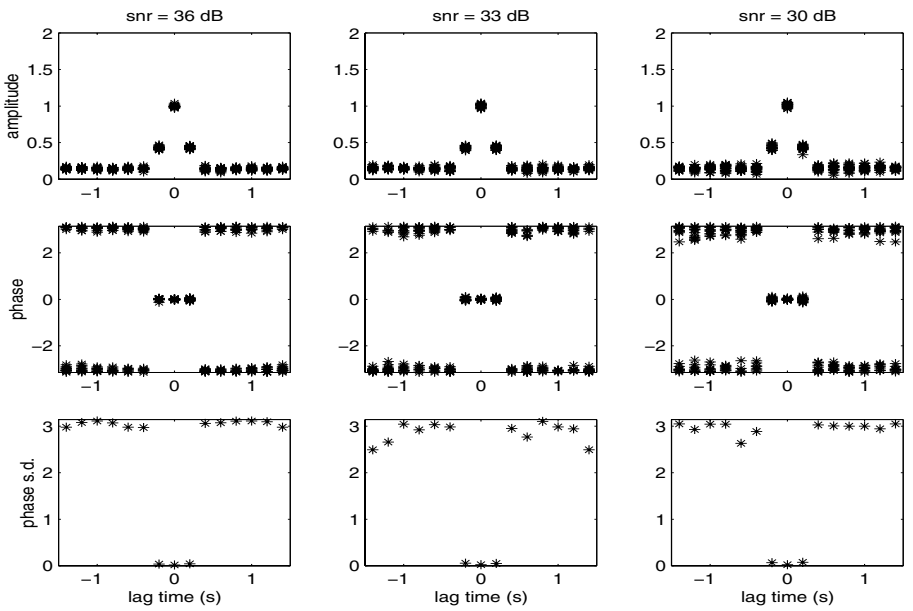

Figure 2.21: Ensembles of 20 complex-envelope seismogram time-series for a 7-digit prs modulated onto a 2.5 Hz carrier wave at various correlogram snr levels, showing the spread of instantaneous amplitude and phase values, and the resulting ensemble phase s.d. at each correlogram lag, for each snr.

the phase s.d. corresponds to a timing error s.d. of

$$\sigma_t = \frac{\sigma_\phi}{\pi} \times 0.2 \text{ s}, \tag{2.72}$$

resulting in $\sigma_t \approx 0.5$ ms at 36 dB, and $\sigma_t \approx 0.1$ s at -6 dB correlogram snr.

Empirical analysis

Figures 2.21 - 2.25 show prs-modulated signal complex-envelope correlogram ensembles obtained by coherently overlaying 20 complex-envelope correlograms, and the ensuing ensemble PSD time-series, for various correlogram amplitude signal-to-noise-ratios. Figure 2.26 presents the timing-error-versus-snr behavior resulting from 30 trials at each snr. The timing error s.d. ranges from 0.3 milliseconds at 36 dB snr to 0.38 seconds at -6 dB snr. Signal timing is stable down to +3 dB, with the timing error slowly increasing with snr. Below the +3 dB snr, the timing error increases rapidly,

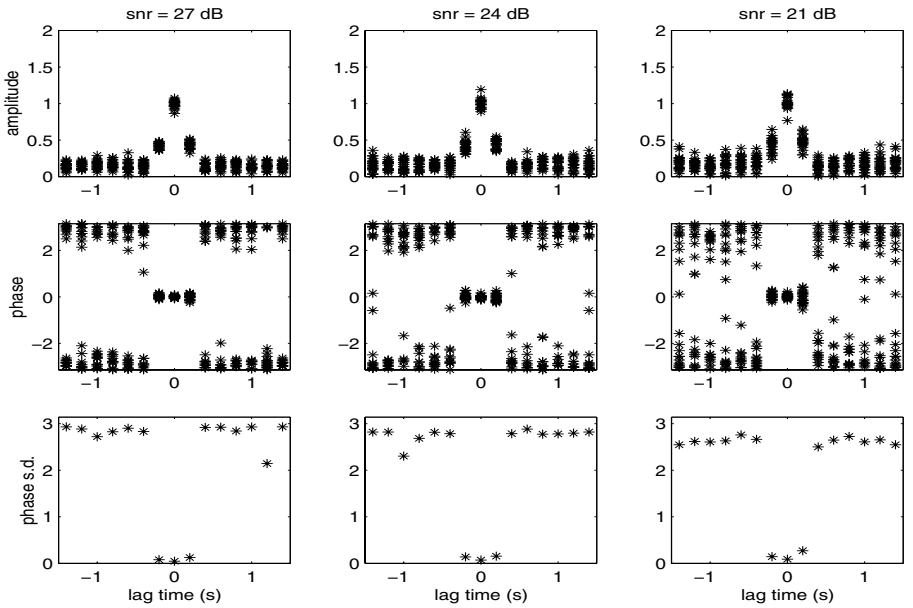

Figure 2.22: Ensembles of complex-envelope seismograms (continued).

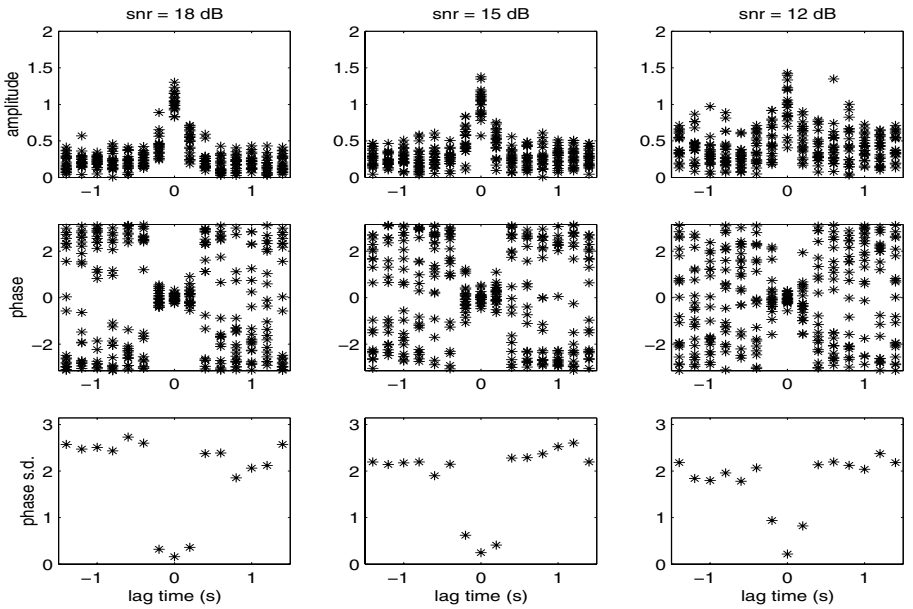

Figure 2.23: Ensembles of complex-envelope seismograms (continued).

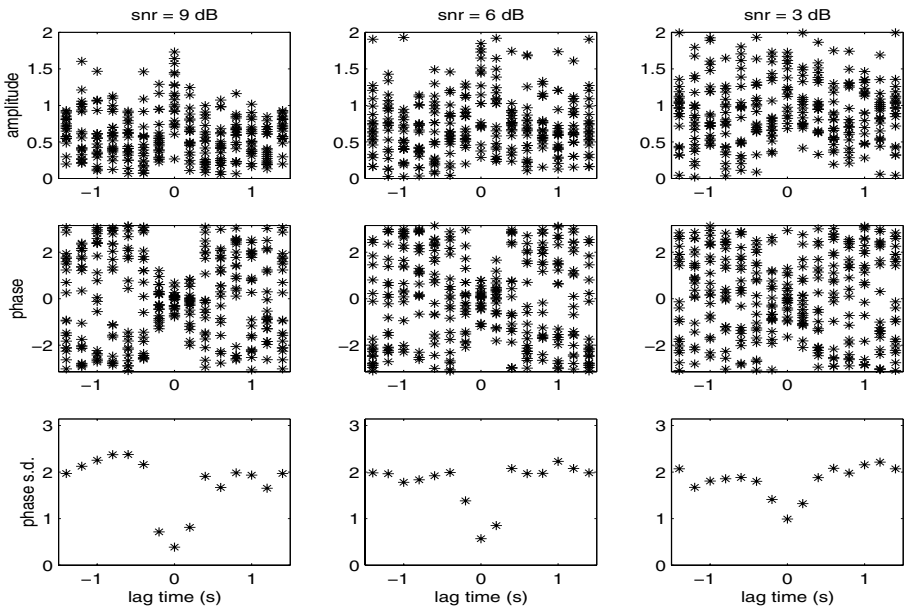

Figure 2.24: Ensembles of complex-envelope seismograms (continued).

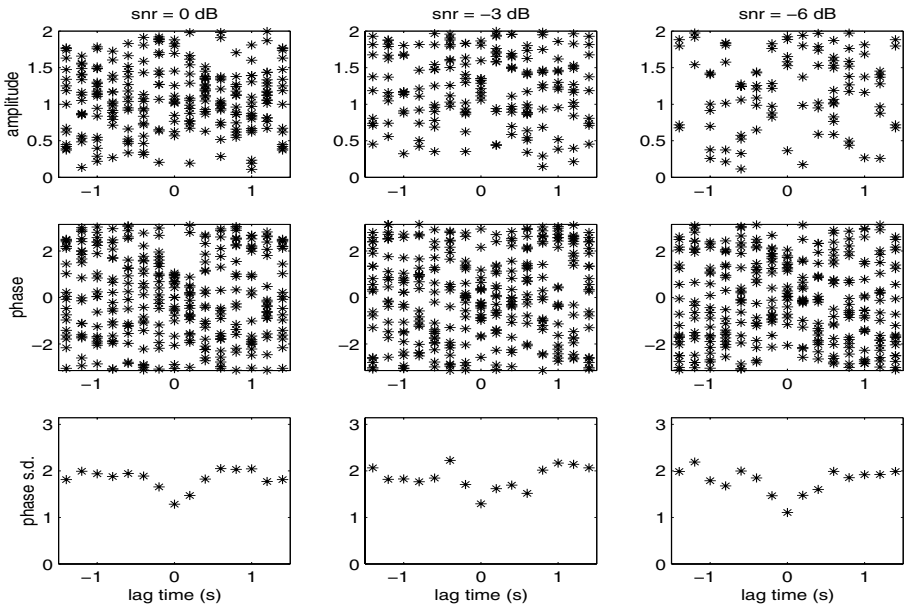

Figure 2.25: Ensembles of complex-envelope seismograms (continued).

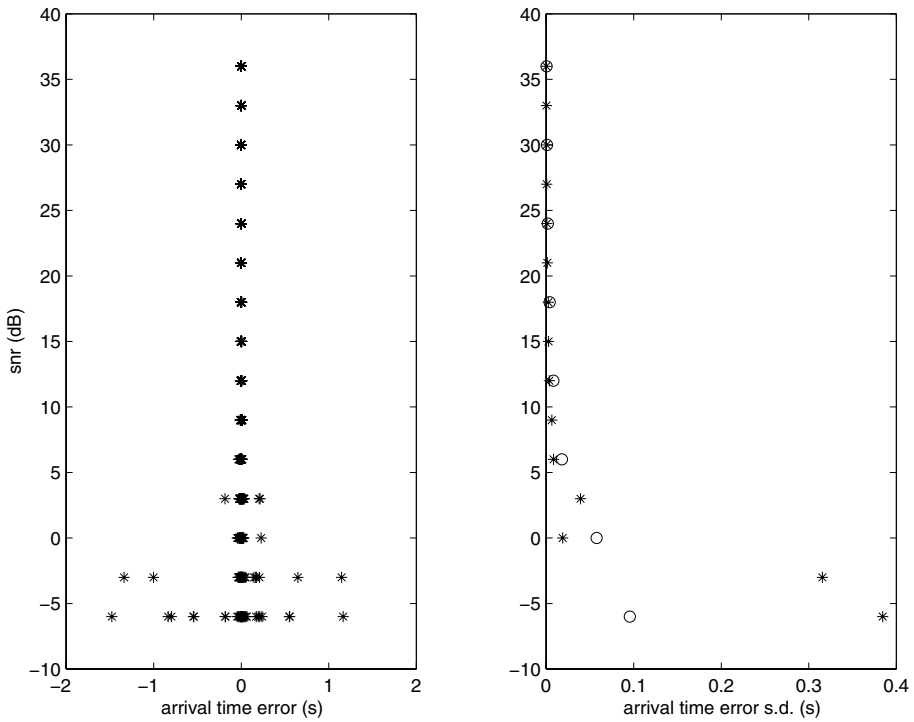

Figure 2.26: Signal arrival time error and error s.d. as a function of correlogram snr, obtained from 30 trials at each snr. The circles in the righthand figure mark the analytically determined time error s.d.

but even at −3 dB remains within one period of the carrier wave (0.4 s for this data). In the academic case that no noise is present, the timing is exact to the least significant computer bit. Down to +3 dB, these observations are in good agreement with the analytically derived PSD for a uniform instantaneous phase distribution of the noise, as shown by superimposing the data points of Figure 2.20, converted to time error s.d., on Figure 2.26. Below +3 dB, outliers cause deviation from the analytically determined timing error; these outliers probably can be removed by means of extreme-error filtering, or by human interaction.

2.3 System requirements

We summarize the system requirements evolved from the system concept, the communications technology items to be incorporated, and the system objectives stated. We consider, respectively, the requirements for the signals to be emitted, the surface force source, signal reception, and front-end signal processing.

The force *signals to be emitted* must satisfy the following conditions:

- signature prescribed and known exactly.
- continuously and accurately repeatable for indefinite time periods.
- long-term time and phase coherent.
- high-resolution, low-side lobe auto-correlation function.
- signal code duration spanning the major seismic phase arrivals (5-20 min).
- allow simultaneous, mutually uncorrelated emission from various source sites.
- low frequency (1-10 Hz).
- Universal Time (UT) controlled to microsecond precision.

The surface force *signal sources* must accommodate the above signal emission requirements. The source sites should preferably be on hard rock in order to minimize transmission surface effects which might adversely affect signal repeatability.

At *signal reception,* the seismometers should be three-component, cover the frequency range of at least 0.5-10 Hz, and preferably be placed in boreholes to minimize surface effects. The signals must be received continuously, and digitized at $\geq$ 50 Hz sampling rate after anti-alias filtering. Sampling must be UT-synchronized to microsecond precision. Either automatic gain control, or multi-level sampling must be provided. The digitized data may be field stacked coherently with the emitted signal code period, but stacking control must be manually or remote-control accessible.

Front-end signal processing in general is to be performed off-line. It must include coherent, noise-weighted stacking over moving-window time periods of weeks or months or longer, followed by quadrature demodulation and

matched filtering of the stacks. This is to result in coherent moving-window ensembles of complex-envelope seismograms consisting of the dual time series of instantaneous amplitude and instantaneous phase. The seismogram length equals the emitted signal code duration period. Next, the automatic signal detection and timing algorithm is to be applied to yield the arrival times of primary and later seismic phases, together with confidence levels and signal-to-noise ratio. The seismograms and the signal timing data are to be recorded in standard record format for local and worldwide distribution to interested parties for evaluation and further analysis.

2.4 System realization concept

To satisfy the above system requirements, we present our system realization concept below, addressing each of the system requirement topics in the same order.

Our prime choice of *signals to be emitted,* see Section 2.2.1, is the pseudo-random binary sequence (prs) modulated onto a low-frequency carrier wave, enabling the selection of families of modulation codes which

- are mutually near-uncorrelated (have low cross-correlation noise).
- have mutually identical sweep duration, of sufficient length to accommodate the major seismic phase arrivals.
- have mutually identical sweep spectrum spanning the earthquake seismology body-wave frequency range of 1-5 Hz or wider.
- have a high-resolution auto-correlation function (triangular auto-correlation peak, its basewidth equals two carrier wave cycles).
- have a low auto-correlation side lobe (low auto-correlation noise), equal to the inverse of the prs length.

In addition to prs signal emission, the so-called "chirp" signals (linear or non-linear frequency sweeps) as used in seismic exploration may be transmitted.

Concerning the *signal emission source*, existing vibrator techniques do not seem capable of meeting the system requirements. For instance, with rotating mechanical eccentrics, it will be extremely difficult to control its

movements as to follow a prescribed pilot signal such as the fast-changing prs signals, maintenance requires too frequent interruptions, and the system would be too much subject to high mechanical wear to enable efficient continuous operation. Other vibrator techniques such as the hydraulic vibrator used in seismic exploration, and the electrodynamic vibrator, suffer from mechanical resonances around 3 Hz caused by the hold-down mass-spring system, harmonic distortion, maintenance problems, and difficulty in generating prs modulated signals (Unger *et al.*, 1987). The low-frequency resonances would impede transmission in the earthquake seismology short-period range of 1-5 Hz. In order to meet the system requirements stated, two types of new seismic vibrator technology were conceived:

- the magnetic levitation vibrator (MLV)
- the linear synchronous motor vibrator (LSMV).

The essential features of these new-technology surface force sources are:

- floating reaction mass (ML), or rolling reaction mass (LSMV).
- no friction (ML), only rolling friction (LSMV).
- virtually maintenance-free.
- one-man "crew" per source.
- accurately follows prescribed signal such as prs, chirp, or virtually any other signal signature.
- continuous, coherent operation for indefinite duration.
- constant peak force over the frequency range 2.5-10 Hz or wider.
- 30 kW power consumption for 50 kN peak force at 2.5 Hz; less power consumption at higher frequencies for the same peak force.
- water cooling.

Signal reception can be realized with existing standard permanent and portable digital seismic stations, arrays, and networks provided with a UT standard of at least microsecond precision. Signal coherency is established by deploying the UT standard at both, sources and receiver stations.

Front-end signal processing, consisting of noise-weighted, coherent stacking, quadrature demodulation and matched filtering, complex seismogram generation, signal detection and timing, are to be performed off-line, or in

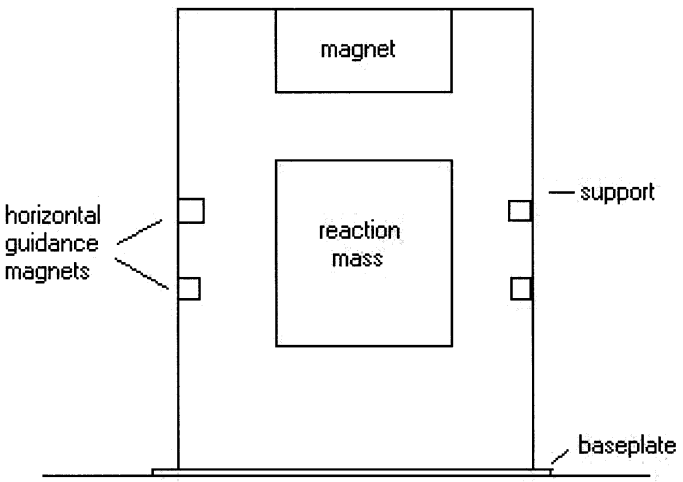

Figure 2.27: Magnetic levitation vibrator schematic diagram.

part on-line, according to the specifications given in the front-end signal processing system requirements, and as described in the section on quadrature processing, Section 2.2.2.

Below, we elaborate on aspects and details of the above items.

2.4.1 The signal emission source

As mentioned, present seismic vibrator technology does not satisfy the requirements for a long-term continuous, coherent emission of surface force pseudo-random sequence signals. Below, we present the two types of new-technology seismic vibrator technology conceived: the magnetic levitation vibrator, and the linear synchronous motor vibrator.

The magnetic levitation vibrator

In the MLV technique (Unger *et al.,* 1987; van Kampen, Ritsema and Unger, 1987), see Figure 2.27, a mass of, e.g., 10,000 kg is kept floating in vertical and lateral magnetic fields. By increasing the vertical magnetic field, the mass is pulled up, and exercises, through the support structure, an increasing reaction force (negative traction) onto the ground. By decreasing the magnetic field, gravity will pull the mass down, and the ground force is

reduced (positive traction). The system acts like a magnetic 10-ton yo-yo. By controlling the magnetic flux in a manner such that the mass acceleration, and thus, assuming a perfectly rigid support structure, the ground force, follow a prescribed pilot signal, practically any kind of modulation of a sinusoidal carrier wave, including the fast changing prs signals, can be obtained as the emitted ground force signal. This emission can be held constant, coherent, and continuously repeatable, in principle for indefinite duration. In its present concept form, the MLV is principally a *P-wave generator*, but in accordance with its radiation pattern, also S-wave components are generated. The concept can be adapted to generate precisely prescribed horizontal reaction mass motion, still keeping the reaction mass floating in vertical and horizontal magnetic fields, but now activating its motion in a push-pull fashion in one particular horizontal direction. Through appropriate ground coupling, the MLV in this way becomes principally an *S-wave generator*, but in accordance with its radiation pattern, also P-wave components are generated.

In comparison with hydraulic and electrodynamic vibrators, to achieve a given peak force, the reaction mass is increased so that its acceleration can be kept below the acceleration of gravity, thus reducing the stroke, and avoiding the need for a hold-down mass with the resulting mechanical resonance problem. The technique thus circumvents the low-frequency mechanical resonance problem, and permits low-frequency transmission for deeper and farther penetration, in particular in high attenuation media. The clean, fast magnetic flux control strongly reduces harmonic distortion, and enables efficient, stable transmission of our proposed pseudo-random sequence modulated signals. Moreover, the reaction mass is the only moving part; its motion is completely without friction. The system, therefore, is virtually maintenance-free, and can be operated by a one-man 'crew' for indefinite time. As stated in Section 2.2.2, signal emission may be interrupted, and resumed coherently with respect to the signal modulation code period.

In a 50 kN peak force, 10 ton reaction mass industrial prototype, built after a technical design by W.A. van Kampen satisfying the source requirements stated, efficient and fast flux control is achieved by means of switching between magnet current injection and extraction, at intervals as short as 10 μs, by a semi-conductor power converter. With this method, high flux stability, and, implicitly, high ground force signal stability, is achieved. In particular, the signal *phase*, in Section 2.2.2 shown to be of utmost relevance for our system objectives, in this way is held stable to within $10^{-5} \times 2\pi f_0$

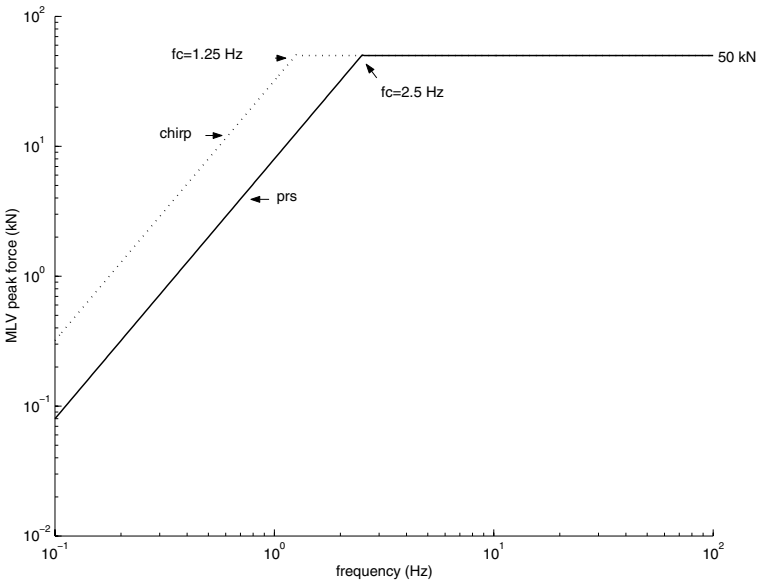

Figure 2.28: MLV peak force spectrum.

radians, i.e., within 0.2 milli-radians for our proposed 2.5 Hz carrier wave, or less than 0.025× the phase standard deviation at 36 dB snr, see Figures 2.19, 2.20. Consequently, the MLV system noise is completely negligible with respect to the seismic noise. This more than satisfies our system objective concerned. The 1600 A peak-current magnet and power converter are water-cooled and use a total maximum dissipated power of 30 kW to deliver 50 kN maximum force amplitude at 2.5 Hz carrier wave, with the BMSEQ requiring an 8 cm reaction mass stroke at this frequency. There is a trade-off between stroke and reaction mass size. A large stroke causes magnetic flux leakage, reducing the effective peak force. Moreover, a larger stroke would mean higher reaction mass acceleration which is prohibitive in order not to exceed the acceleration of gravity and the need for a hold-down mass with resulting mechanical resonance problems. Consequently, a higher peak force demands a larger reaction mass and correspondingly larger vibrator dimensions.

The concept was extended to include commercial exploration frequencies. For this purpose, in this design, the constant 50 kN peak force has been extended to at least 100 Hz signal frequency, with decreasing stroke and less power consumption at the higher frequencies (Figure 2.28). The peak force

Figure 2.29: Magnetic Levitation Vibrator industrial prototype: peak force 50kN from 2.5 to 170 Hz, height 2 m, diameter 1.5 m, weight 15,000 kg. The power converter (not shown), is external.

decreases 12 dB/oct with decreasing frequency, down from 50 kN at 2.5 Hz for prs signals, and, maintaining the 8 cm stroke, down from 50 kN at 1.25 Hz for chirp signals

Dissipative power is of the order of 30 kW, but because of the highly reactive voltage-current relation, power must be supplied by a 200 kVA *apparent power* diesel generator, or possibly by sun-panels. The emission can be sustained continuously for weeks or months or longer by a one-man 'crew'. Since, for our purpose, the vibrator is to be used as a fixed-site source, no special transportation facilities have been designed. The vibrator could be lowered into a two meter diameter borehole, or placed in mine shafts, to reduce parameter variation due to surface effects.

The industrial prototype has been assembled (Figure 2.29) and equipped

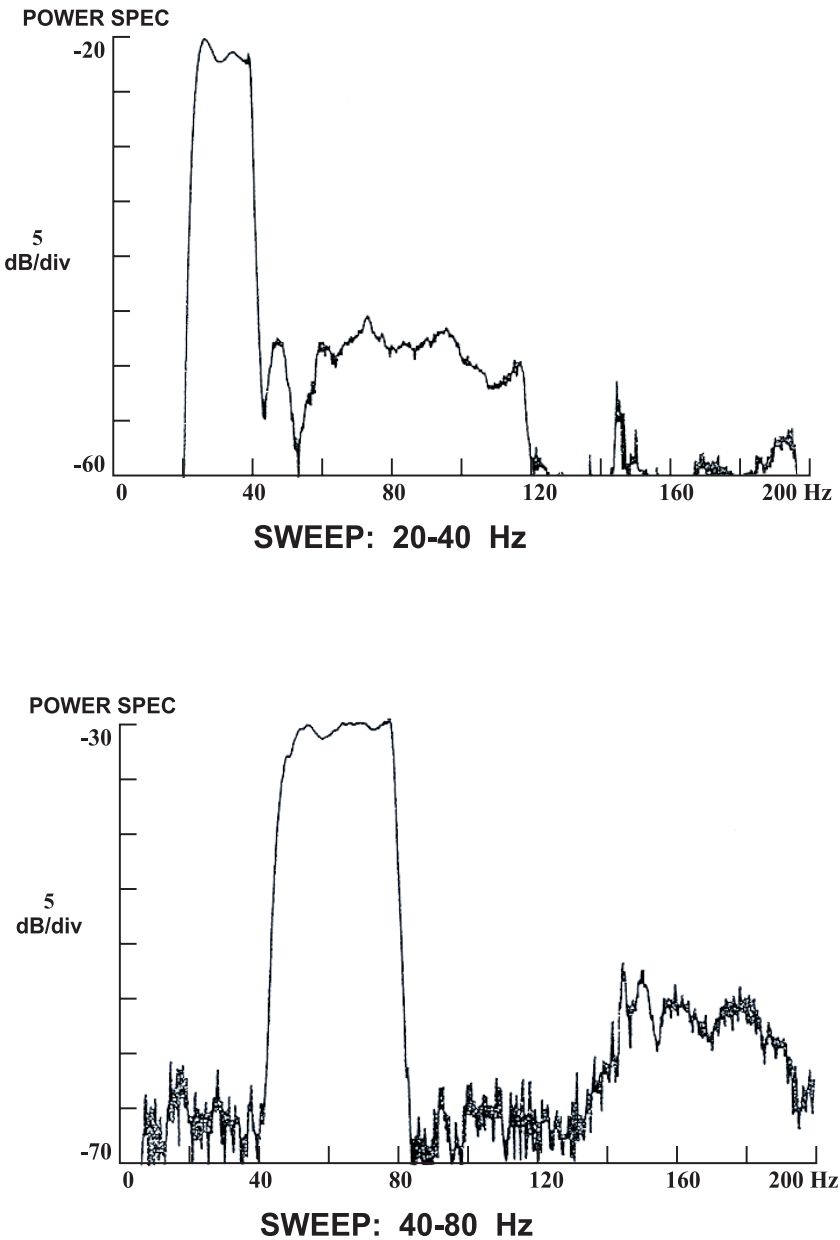

Figure 2.30: Magnetic Levitation Vibrator prototype test performance. Note the low harmonic distortion and system noise levels. Courtesy of Shell Research, Rijswijk, The Netherlands.

with a provisionary vertical motion control system for sweeps of short duration (60 s maximum), 8-100 Hz, of the seismic exploration type. Preliminary tests have demonstrated the feasibility of the new technology and its improvement in performance over hydraulic vibrators (Figure 2.30). At the present time, this prototype is jointly owned by Schlumberger, Houston, Texas, U.S.A., and Verolme Machinefabriek IJsselmonde (VMIJ), Rotterdam, The Netherlands. Schlumberger holds the patents involved. Schlumberger/VMIJ may make the prototype 'as is' available to the earthquake seismology and deep seismics research community. However, a new, comprehensive vertical and lateral motion control system has to be designed, and tests with long-term coherent, 1-5 Hz, 5-20 min sweep length signals must be performed prior to field experiments.

The linear synchronous motor vibrator

A linear motor can be considered as an unrolled version of a rotary motor, and consists of a linear stator and a linear 'rotor'. Like in a rotary motor, a traveling magnetic flux pulls the rotor, but now in a horizontal direction on wheel bearings along a mechanical guidance rail. Increasing/decreasing the magnetic flux accelerates/decelerates the rotor; inverting the magnetic field direction inverts the rotor motion. Thus, as in the case of the MLV, the rotor motion can be controlled to very precisely follow a prescribed reference signal. Linear motors are used in a variety of applications, from material sorting, moving, and processing functions in the steel industry and high speed transportation systems, to heart pumps and pick-and-place machines in the chips industry. In the linear *synchronous* motor (LSM), both the stator and the rotor are excited, the latter often by means of permanent magnets. In recent years, modern, computer controlled power electronics, and the use of rare earth magnets have increased the LSM capabilities considerably: >200 kN thrust, 60 m stroke, 25 m/s speed. The LSM technique is used, among other applications, to a high degree of efficiency, with near 100% duty cycle, in drives for roller coasters in entertainment parks. The technique can be adapted to refine its motion control to the extent that *horizontal* reaction mass acceleration is produced which precisely follows a prescribed signal. Through appropriate ground coupling, in this way virtually any type of desired horizontal ground force signal can be delivered to the earth. The vibrator thus is principally an *S-wave generator*, but, in accordance with its radiation pattern, also P-waves are generated. To achieve sufficient ground

coupling, the vibrator gravitational force, i.e., its weight times the acceleration of gravity, must exceed the horizontal driving force. In this way, also S-wave vibrators are subject to the hold-down problem when the horizontal reaction mass acceleration exceeds the acceleration of gravity. In order to avoid these problems and the associated mechanical resonance phenomena, the reaction mass must be chosen sufficiently large to keep its acceleration below the acceleration of gravity for a desired peak force, as discussed in the MLV case. With vertical guidance, the LSMV becomes principally a P-wave generator, but, in accordance with its radiation pattern, also S-waves are generated. Either one satisfies our transmission system source requirements in the same fashion as does the MLV. At the present time, the LSMV development is still in the concept stage and subject to proprietary information restrictions.

2.4.2 Earth propagation

Obviously, the Earth propagation part of the total transmission system is not in our hands, but seismology aspects have to be taken into account to assess their consequences for our proposed transmission system performance. Separately, we dedicate Chapter 3 to mathematical wave propagation modeling for our system. In the present subsection, we attempt to estimate the effects of Earth impedance and the attainable transmission range under various conditions.

Earth impedance

The issue of Earth impedance, defined as the ratio of traction over particle velocity, has been amply addressed in hydraulic seismic vibrator technology (e.g., Miller and Pursey, 1954; Safar, 1984, Baeten, 1984; Sallas, 1984). For hydraulic vibrators, the issue is especially important in reaction mass and baseplate motion control, taking into account the vibrator compliance and mass parameters. The conclusions from this literature are that for hard ground, applicable to our work, the Earth impedance is predominantly capacitive, and that, for the relatively high frequencies used in commercial seismic exploration, the feedback control should consist of a weighted sum of baseplate and reaction mass motion.

The impedance modeling problem is complicated, even for the case of

an isotropic, homogeneous, elastic half-space, (1) by the singularity of the Green function at the origin, and (2) by the mixed boundary conditions existing underneath and around the vibrator baseplate. Consequently, a simple, valid expression for the Earth impedance cannot be found, and theoretical impedance values will have to be obtained through extensive numerical approximations, the validity of which may be questionable.

The MLV has been designed with a high support stiffness, such that the mechanical vibrator parameters do not interfere with the Earth impedance; the MLV mechanical resonance frequency is above 300 Hz. Especially for the low frequencies to be used in our system, there is no need for a weighted sum of baseplate and reaction mass motion; the reaction mass motion determines the ground force signal signature. Also, because the MLV reaction mass acceleration remains well below the acceleration of gravity and does not require a hold-down weight, there will be no low-frequency resonances; the vibrator remains coupled to the ground at all times. The baseplate dimension, of approximately one meter diameter, is small with respect to wavelengths of 0.4-6 km corresponding to the 1-5 Hz signal frequency and 2-6 kms^{-1} wave propagation velocity. Consequently, we consider the vibrator as a surface *point-force source.*

Transmission range

In Section 2.2.2 we arrived at a formula expressing the matched filter (MF) output power signal-to-noise ratio (snr^2) as a function of the various transmission parameters involved; we repeat this expression here:

$$\text{snr}^2 = K\hat{F}^2 r^{-2} T \int_{f_1}^{f_2} f^{-\alpha} F(f) \exp\left(-\frac{\pi f r}{cQ}\right) df. \tag{2.73}$$

where

- K is a proportionality factor lumping the radiation pattern and boundary transmission/reflection effects.
- $\hat{F}$ is the source force signal amplitude.
- $F(f)$ is source signal power density spectrum, normalized to unit power.
- f represents the signal transmission frequency components in the signal band f_1 to f_2.

- r is the raypath range.
- α is the order of displacement noise power density increase with frequency.
- T is the signal duration, i.e., the total coherent signal transmission and stacking time.
- c is the propagation velocity.
- Q is the propagation quality factor.

Based on past seismic vibrator transmission experiments, we want to use this expression to obtain a rough estimate of attainable transmission range versus total required transmission time as functions of the transmission parameters f, α, c, Q. To this end, we approximate the frequency variable f in the integrand in Eq. (2.73) by a constant equal to the frequency band center frequency, $f \longrightarrow f_c = (f_1 + f_2)/2$, resulting in

$$\mathrm{snr}^2 = K\hat{F}^2 r^{-2} T W f_c^{-\alpha} \exp\left(-\frac{2\pi f_c r}{cQ}\right), \tag{2.74}$$

where $W = f_2 - f_1$ is the effective signal frequency band.

In P-wave vibrator experiments conducted around the San Andreas fault (Clymer and McEvilly, 1981) vertical reflections from the Mohorovičić discontinuity (the 'Moho') at approximately 24 km depth were obtained by stacking and correlating twenty 30 s, 30-10 Hz chirp sweeps generated by a 50 kN hydraulic seismic vibrator; the P-wave propagation velocity is estimated as $c = 5$ km/s, the area propagation quality factor as $Q = 200$. This agrees with deep seismic profiling results, where similar depths have been reached with single 26 s sweeps from an array of five vibrators, the latter reducing the necessary sweep duration by a factor $5^2 = 25$.

Taking the Clymer and McEvilly (1981) result ($r = 2 \times 24 = 48$ km, $T = 20 \times 30 = 600$ s, $f_c = 20$ Hz, $W = 20$ Hz, $c = 5$ kms^{-1}, $Q = 200$) as a 0 dB reference, assuming the noise spectrum to be as in Figure 2.18 ($\alpha = -3$), and applying Eq. (2.74) in comparison, Figure 2.31 shows rough estimates of snr relative to this reference point ("ref" in the figure), as a function of attainable raypath range, for various $\{f, Q\}$ combinations, when deploying a 50 kN peak force seismic vibrator. On the right is annotated the coherent transmission and stacking time T required to obtain the same snr as at the reference point, i.e., a snr sufficient to reliably detect and time primary and

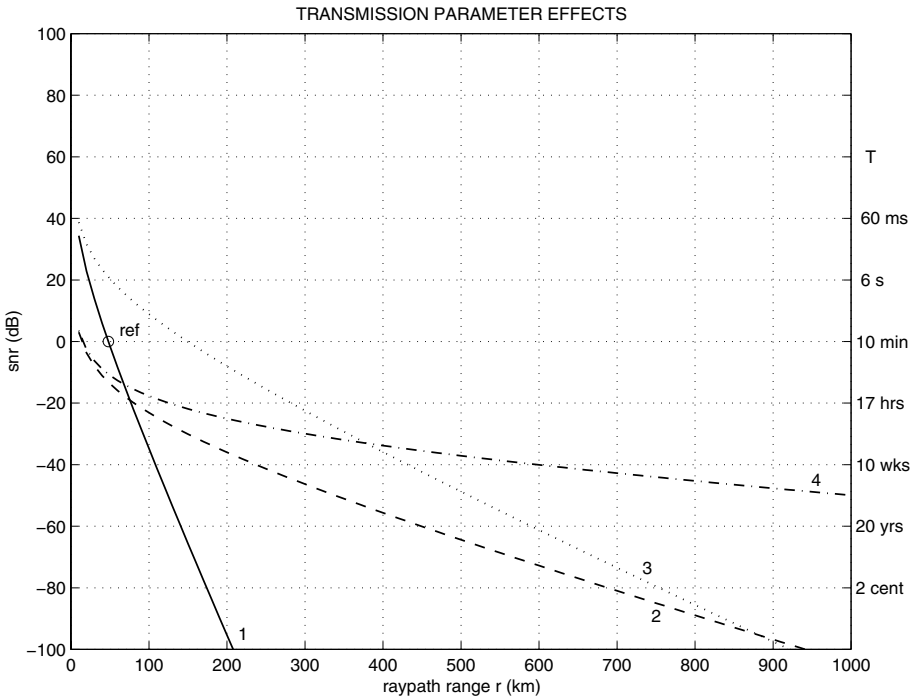

Figure 2.31: Estimates of signal-to-noise ratio (snr) and required compensating transmission time T (on the right) vs. transmission range, referenced (ref) to seismic vibrator results reported by Clymer and McEvilly (1981): (1) 30-10 Hz chirp, $Q = 200$; (2) 2.5 Hz prs, $Q = 200$; (3) 30-10 Hz chirp, $Q = 1000$; (4) 2.5 Hz prs, $Q = 1000$. The required transmission time increases dramatically with raypath distance.

later seismic phase arrivals. The graph suggests that, strongly dependent on regional seismic noise and attenuation characteristics, sufficient snr is obtained at raypath ranges of $r = 150$-300 km, corresponding typically to depth ranges of 75-150 km and horizontal ranges of 100-200 km, with one week continuous, coherent signal transmission, stacking, and matched filtering of our proposed 2.5 Hz prs signal. According to Figure 1.5, this period approximately corresponds to the precursor time of a magnitude $M = 3.0$ earthquake. As attenuation models, and, in particular, Q-values, in general are not well established, propagation results may well be quite different from the example presented here. Eventually, only field experiments can establish the true transmission range possibilities. As a final remark, from Eq. (2.73) we note that the transmission raypath range increases quadratically with the vibrator peak force $\hat{F}$, or with the number of equal peak force vibrators

deployed in a tuned source array.

2.4.3 Signal reception

As mentioned in the broad concept, signal reception can take place at fixed standard digital seismic stations or arrays, or with portable instruments or arrays. Modern digital seismometers have a frequency range of 10^{-5} – 10 Hz, a dynamic range of 120 dB, automatic gain control, and 16-24 bit digital recording. As found in Section 1.2 on earthquake process modeling, seismometry will have to be dense, on the order of 1-10 km spacing. New technology developments such as optical fibre interferometry (Whelan, *et al.*, 1998a,b) are likely to result in relatively inexpensive, easy-to-install, dense, digital seismometer network systems.

A concern may be when the transmitted signals arrive well below the local noise level, or even below the least-significant bit; one might think that in that case the signal would not be retrievable. However, since we can arbitrarily say that the noise is superimposed upon the signal, or that the signal is superimposed upon the noise, even if the signal amplitude at the station is below the least significant bit, it will bias the noise amplitudes and 'push' them over the various digitization levels. Thus, although this process is non-linear, the signal is ultimately retrievable with a long-term stacking and matched filtering process.

2.4.4 Front end signal processing

The continuous data flow digitally recorded by fixed and/or portable seismic stations is to be converted into complex-envelope seismograms featuring the dual time-series of instantaneous amplitude and instantaneous phase, by the following processes:

- noise-weighted, coherent stacking
- quadrature matched filter processing
  - Cartesian component demodulation
  - correlating each Cartesian component with the emission pilot signal
  - instantaneous amplitude correlogram
  - instantaneous phase correlogram

  - signal detection and timing

- complex seismogram recording and distribution
  - worldwide standard data format
  - distribution by worldwide data centers.

The above items are addressed below in more detail.

Data stacking

The continuously recorded digitized data are to be cut into records with duration equal to the emitted prs signal period. Since the seismic noise levels vary with time, obviously records containing a relatively high noise level will contribute less information than records with lower noise levels. Therefore, we *weight* each entire prs-length record with a factor inversely proportional to the rms amplitude level of the entire record. Since in general the signals are received well below the local noise level, this rms value reflects, to a sufficient degree, the power level $\mathcal{N}$. The weights are to be normalized with respect to a local standard noise level $\mathcal{N}_0$ obtained by measuring the rms noise under typical noise conditions at the station concerned, resulting in weights $\frac{\mathcal{N}_0}{\mathcal{N}}$. We realize that relatively long records with short, high-level noise bursts or spikes may be adversely affected by this weighting scheme. For that reason, automatic noise burst and spike editing may be incorporated before weighting. In addition, since the data are recorded with automatic gain control to obtain maximum resolution, all data to be stacked into one stack must be *gain-equalized* before stacking.

Since the record length exactly equals the prs signal length, signal phase coherence and full synchronization are preserved at all times. The actual moment of physically starting the record is irrelevant, but the start time must be recorded, together with the record gain applied as given by the receiver automatic gain control, and the noise weight used. The noise-weighted, gain-equalized records then are stacked and the stack record submitted to the quadrature matched filter process.

The number of records to be stacked before further processing is a trade-off between obtaining sufficient processing gain and the desired elapsed-time parameter variation resolution. As pointed out in Section 1.2, small-earthquake precursors will have relatively short precursor times which may

be obscured when using long averaging times. On the other hand, if processing gain is insufficient due to insufficient stacking time, the earthquake-related parameter variation may be obscured by noise, i.e., seismic noise and/or natural (non-earthquake related) parameter variation. Moreover, these phenomena will be different for different regions with different geological or tectonic regimes. When preserving the 'raw' data or stack records with relatively short stacking times, e.g., on the order of three hours, one may experiment with stacking time versus parameter variation resolution.

Instead of performing the stacking process off-line as described above, it may be implemented on-line by intelligent data recorders if desired. It then is imperative to maintain relatively short stacking times.

Quadrature matched filter processing

The quadrature matched filter processes of Cartesian component demodulation, correlation with the emission pilot signal, and generating the complex-envelope seismogram consisting of the dual time-series of instantaneous amplitude and instantaneous phase correlograms, are to be performed as described in the paragraph on quadrature matched filter processing theory, Section 2.2.2. This is to be followed by signal detection and timing as described in Section 2.2.4.

Complex seismogram recording and distribution

The complex-envelope seismograms generated are to be recorded in standard world-wide data exchange format as used in seismogram exchanges. The record headers should contain source and station identification, and record start time, gain, and noise weights used. The records then can be sent to worldwide data distribution centers from where they can be retrieved by interested parties for further research and analysis, or sent directly to interested parties upon request.

2.4.5 Simulation

We present a simple 2D simulation of crustal raypaths and corresponding seismograms produced by two seismic P-wave vibrators simultaneously transmitting mutually uncorrelated prs signals. The velocity profile is given in Figure 2.32; the raypaths for the direct P-waves Pg, and the first Moho-reflected P-waves Pm, together with δ-functions reflecting their arrival time

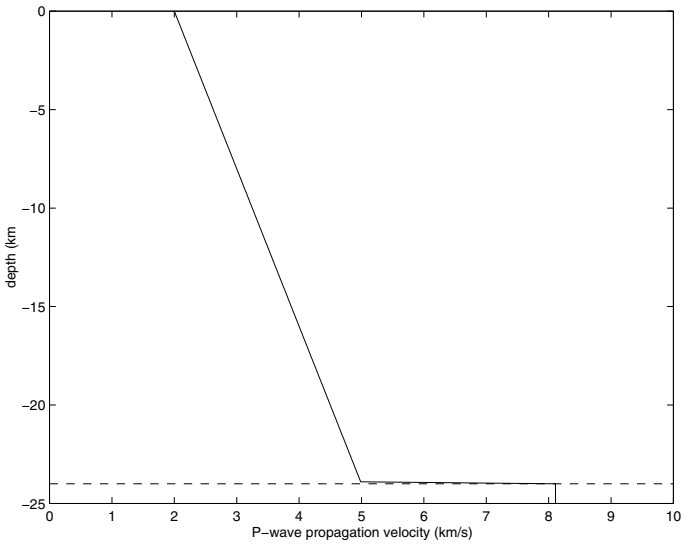

Figure 2.32: P-wave velocity profile in ray tracing simulation.

and relative amplitude, are presented in Figure 2.33. For each of the receivers R1-R5, a coherent, noisy complex-envelope seismogram ensemble and its phase standard deviation time series are pictured in Figures 2.34-2.38. Because of the configuration symmetry, the seismograms for receivers R6-R9 are identical, except for noise, to those for receivers R4-R1, in this order.
The raypaths were constructed with the body wave "ray-shooting" method, i.e., starting with a given ray departure angle from the source, we apply Snell´s law over small ray increments according to the given velocity profile, and modify the departure angle iteratively until the ray "hits" the receiver concerned. For each ray, summation over all raypath increments yields the total raypath length r and the travel time T. For the Pg waves, the relative amplitude is calculated from the P-wave far-field radiation pattern, applying a geometric spreading attenuation factor r^{-1}, and approximating the internal friction attenuation, with $Q = 250$, as for an $f = 2.5$ Hz monochromatic wave, according to the formula

$$\text{attenuation factor} = \exp(\pi f T/Q). \tag{2.75}$$

The Pm wave amplitude is computed in the same manner, but in addition, the reflection coefficient at the Moho boundary is taken into account, as given by the transmission matrix (Aki and Richards, 1980) for the given velocities and densities at both sides of the boundary.

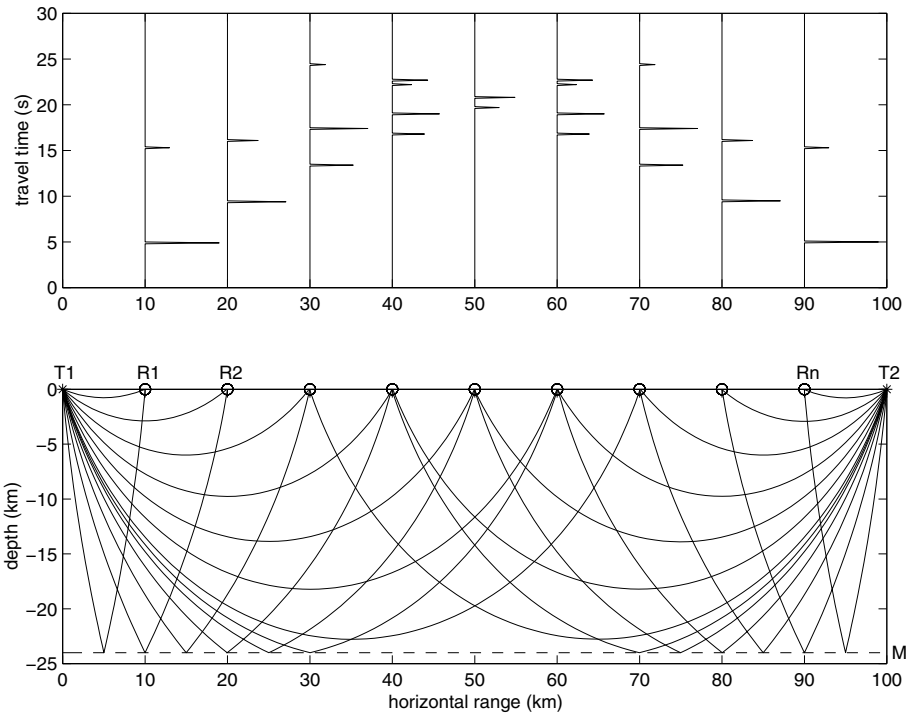

Figure 2.33: Crustal Pg, Pm rays (lower figure) and signal arrivals (upper figure) for the velocity profile of Figure 2.32 and a given transmitter/receiver configuration T1,T2,R1,...,R9. The δ-functions in the upper figure represent the arrival times and relative amplitudes of the Pg and Pm waves. M indicates the Mohorovičić discontinuity.

The seismograms are obtained by convolving the δ-function traces of Figure 2.33 with the prs modulated transmission signals, adding normally distributed random noise, and performing quadrature matched filter processing as described in Section 2.2.2. The noise is added at an amplitude signal to rms noise ratio of $18 - 10\log_{10}(2WT)$ dB, the right term being the matched filter processing gain, so that the seismogram signal to noise ratio equals 18 dB, all referenced to the amplitude of the strongest of all signal arrivals over the entire receiver array, in this case the first arrival at receiver R1. In this way, the absolute noise level is the same at all receivers and for all arrivals. Due to sampling at four times carrier wave frequency, and each pseudo-random sequence digit containing exactly one cycle, signal arrivals are visible as 3-point triangular correlation peaks in the instantaneous ampli-

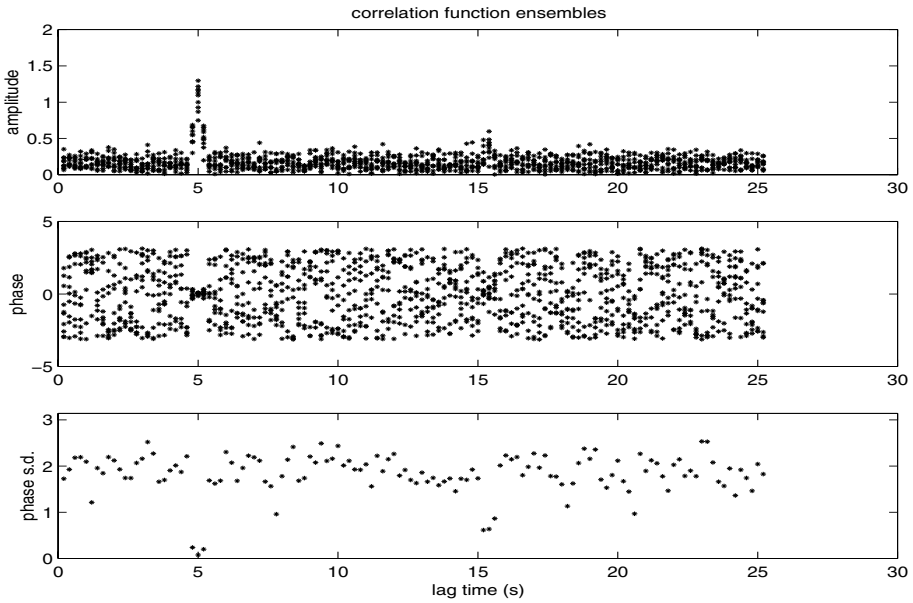

Figure 2.34: Coherent complex-envelope seismogram ensemble and phase s.d. time series for receiver R1.

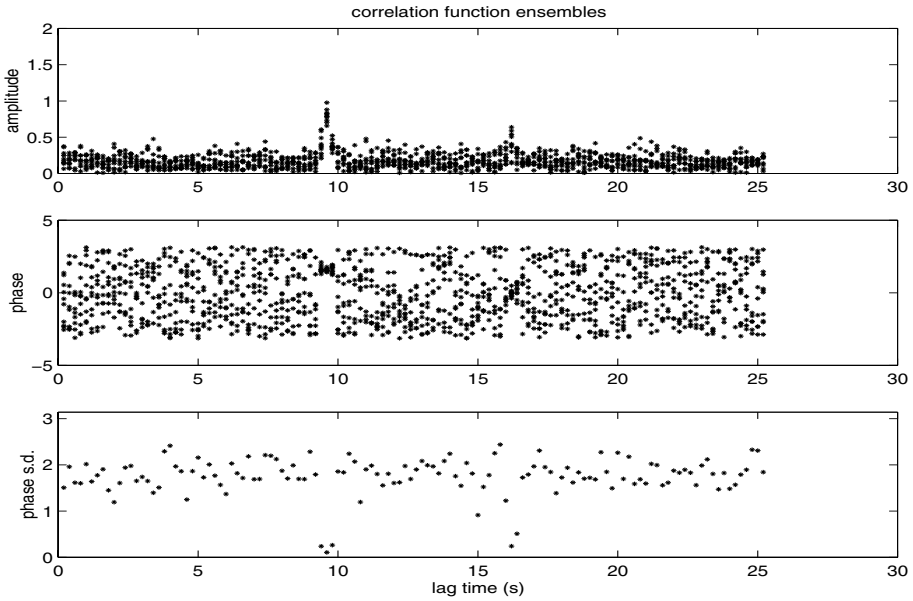

Figure 2.35: Coherent complex-envelope seismogram ensemble and phase s.d. time series for receiver R2.

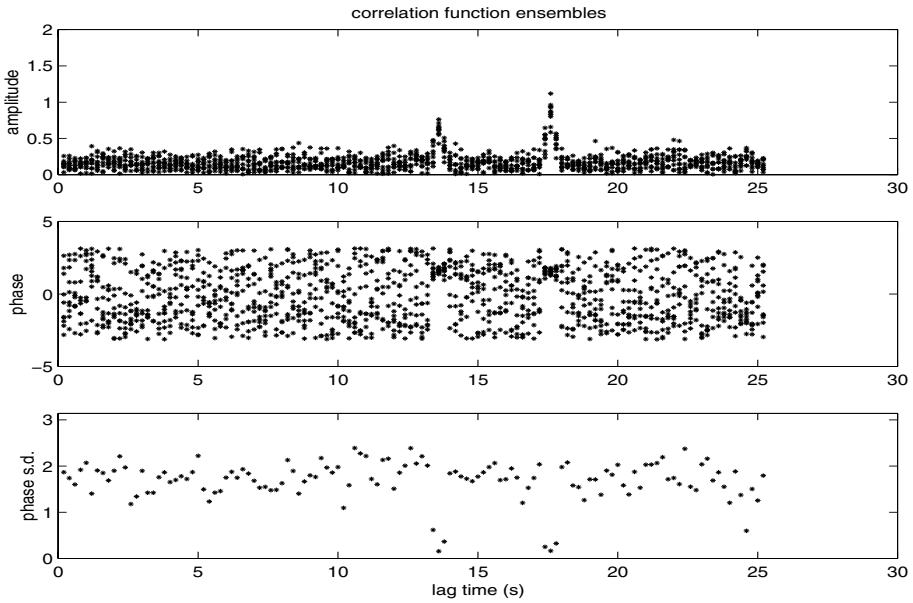

Figure 2.36: Coherent complex-envelope seismogram ensemble and phase s.d. time series for receiver R3.

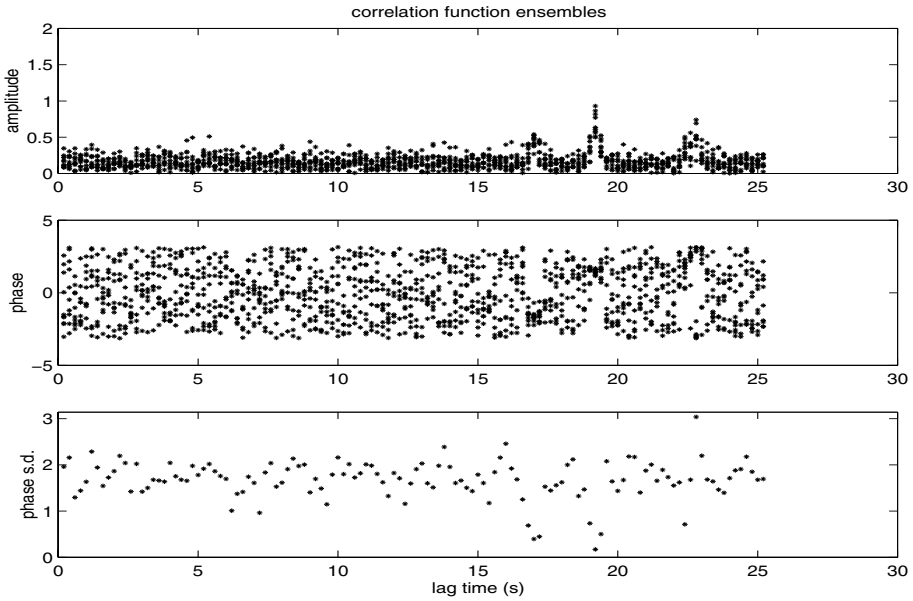

Figure 2.37: Coherent complex-envelope seismogram ensemble and phase s.d. time series for receiver R4.

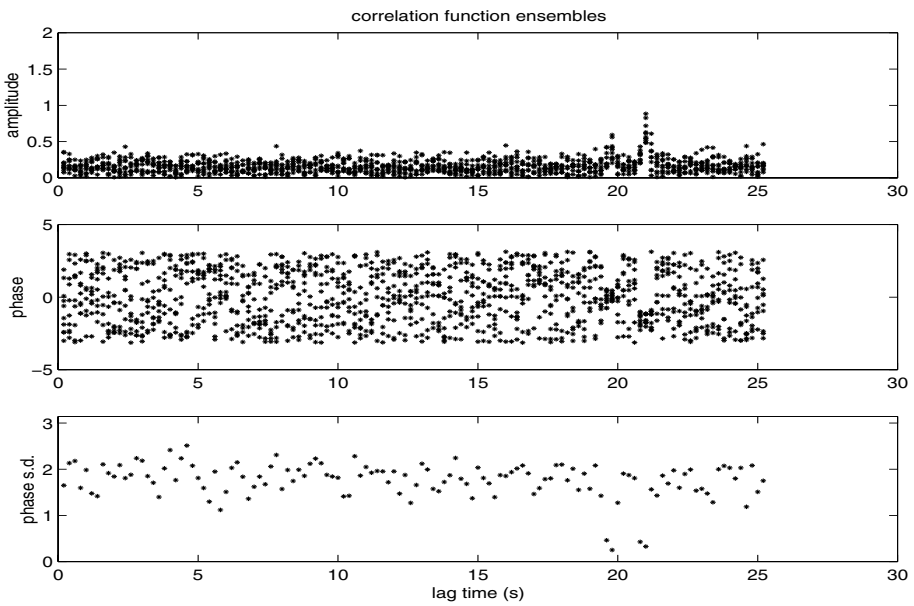

Figure 2.38: Coherent complex-envelope seismogram ensemble and phase s.d. time series for receiver R5.

tude seismogram ensembles for the higher signal to noise ratios (in general $\geq$ 6 dB), and, including for $\leq$ 6 dB signal to noise ratios, as 3-point minimum spread clusters in the instantaneous phase seismogram ensembles resulting in minima in the phase s.d. time series, conform Section 2.2.

We observe that, with a primary seismic phase arrival at 18 dB signal-to-noise ratio, all other arrivals, with the exception of the fourth arrival at receiver R4, are duly detected and timed correctly, supporting our suggestion that travel time tomography can be adequately performed with a limited number of controlled-signal sources. The problem with the fourth arrival at R4, within one second of the third arrival, is that its instantaneous phase value approximately equals $\pm 180^\circ$, the noise then causes ensemble phase fluctuations to hover around these two values, so that the phase s.d. is maximized rather than minimized. We still have to correct our signal detection/timing algorithm to eliminate this problem.

Chapter 3

Elastodynamic Wavefield Perturbation

For our main objective of earthquake precursor measurement and earthquake prediction, in Chapter 2 we presented the technical design layout of a seismic transmission system in which *signal emission and reception are stationary in space and elapsed time*, and which is capable of high-resolution signal parameter measurement. In stationary transmission, any changes in signal arrival time and signal contents must be caused by changes in Earth physics quantities somewhere along the propagation path in the Earth's interior. These changes in physics quantities may be indicative of an earthquake preparation process. Signal changes observed in elapsed time, therefore, are potential earthquake precursors. The precursory character is to be confirmed or rejected by systematic, continuous measurement and statistics compilation on the correlation and non-correlation with regional seismic activity.

In order to anticipate which signal changes can be expected, and to which extent, we need to perform perturbation analysis on those Earth physics quantities which determine the signal propagation characteristics. Inversely, if sufficient space-time data are obtained, modern ray-tracing, imaging and inversion methods may enable us to deduce the location, geometry, and character of the earthquake preparation zone, and to monitor its evolution as an *emergent heterogeneity* by means of elapsed-time seismic tomography.

The mathematical framework for the problem of monitoring Earth physics quantities and parameters lies in the theory of seismic wave propagation. In

this chapter, for our proposed seismic transmission system, we formulate the propagation of seismic waves emanating from a surface point-force source in a linear, time-invariant, locally reacting solid. Our objective in this chapter is twofold:

- to assess the effects that changes in Earth physics quantities and parameters have on seismic signals generated by a space and elapsed-time stationary source-receiver system.
- to establish explicit mathematical relations between parameter changes on the one hand, and the signal changes on the other, for possible application in seismic tomography.

First, we summarize the derivation of the elastodynamic wave equations for a linear, time-invariant, locally reacting solid jointly for point-force surface sources representing our seismic vibrators, and volume density injection sources representing earthquakes and underground explosions. In this development, we will see that for the stated objectives, we cannot, in principle, neglect the static stress spatial gradient term. To solve this problem, we isolate this term as a perturbation in the form of an internal contrast source distribution, and take it to the right-hand side of the elastodynamic wave equations. In similar fashion, we avoid polemic issues and fundamental problems in modeling wave propagation in anelastic and anisotropic media, by considering internal losses and anisotropic behavior as perturbations of wave propagation in a general isotropic medium, and represent also these perturbations as internal contrast source distributions. This formulation leads to an essentially nonlinear problem; we propose a Born type linearization by substituting the background wavefield in the contrast source domains.

Thus, a standard wave propagation algorithm for an inhomogeneous, isotropic background can be used and the internal static stress, anisotropy and losses considered as contrast source perturbations with respect to this background. A candidate for describing the wave propagation in this background is body wave ray theory, valid for "far-field, relatively high-frequency" body waves in "smoothly varying" media. We adopt this theory as expressed in textbooks (e.g., Aki & Richards, 1981; Dahlen & Tromp, 1998), but state explicitly the limitations with respect to the approximations applied in establishing this theory, and analyze in this sense its validity relative to our proposed controlled seismic signal transmission. For a given velocity distribution in the background medium, results obtained from appropriate ray-tracing techniques define the geometric raypaths, the raypath length, the

polarization vectors, and the travel time along each ray. These parameters, and the velocity distribution, may be adjusted through travel time tomography. The final results establish the ray-theoretical Green function for the inhomogeneous, isotropic background medium. Since our wave propagation formulation is preferably carried out in the frequency domain, we also express the ray-theoretical Green function in the frequency domain. The three types of contrast sources: static stress, losses, and anisotropy, are to be found by inversion of observed phenomena through our mathematical representation; we do not elaborate on the specific inversion algorithm to be used. The observed information for this inversion, as well as for travel time tomography, may come from earthquakes, underground explosions, and seismic vibrator signals, the latter preferably generated by our proposed seismic transmission system.

At this stage, the *static* medium properties, including both losses and anisotropy, are defined within the background medium limitations mentioned. Our main objective is to locate, map, and characterize earthquake preparation zones emerging in elapsed time. Their location and geometry can be found from the intersections of rays experiencing elapsed time differences in travel time; their character is to be determined from contrast source inversion.

Throughout this thesis, emphasis is placed on the attempt to *technically* create a seismic transmission system capable of continuously, systematically, and accurately monitoring the Lithosphere in space and elapsed time for changes in Earth physics quantities. The wave propagation models presented, therefore, are intended mainly to illustrate the need for such a system in order to advance earthquake process research through continuous *in situ* parameter measurement, and to establish the feasibility of parameter measurement by our proposed system conform the stated objectives. At the same time, the model may serve as a suggested framework from which further research may be undertaken.

3.1 The elastodynamic wave equations

In our development we basically follow De Hoop (1995) for a linear, time-invariant, locally reacting solid. We start with the equation of motion

$$-\triangle_{k,m,p,q}\partial_m \tau_{p,q} + \dot{\Phi}_k = f_k \,, \tag{3.1}$$

the deformation rate equation

$$\triangle_{i,j,m,r}\partial_m v_r - \dot{e}_{i,j} = h_{i,j}\,, \tag{3.2}$$

where $\Delta_{i,j,p,q} = \frac{1}{2}\,(\delta_{i,p}\delta_{j,q} + \delta_{i,q}\delta_{j,p})$ is a unit tensor of rank four. Furthermore, ∂_m denotes differentiation with respect to x_m, while ∂_t denotes differentiation with respect to time. In these equations, the different quantities are

$$\begin{aligned} v_r &= \text{particle (drift) velocity } (\mathrm{ms}^{-1}),\\ \tau_{p,q} &= \text{stress } (\mathrm{Pa}),\\ \dot{\Phi} &= \text{mass flow density rate } (\mathrm{kgm}^{-2}\mathrm{s}^{-2}),\\ \dot{e}_{i,j} &= \text{deformation rate } (\mathrm{s}^{-1}),\\ f_k &= \text{volume source density of force } (\mathrm{Nm}^{-3}),\\ h_{i,j} &= \text{volume source density of strain rate } (\mathrm{s}^{-1}). \end{aligned}$$

The equation of motion and the deformation rate equation are supplemented with the constitutive relations which express $\{\dot{e}_{i,j}, \dot{\Phi}_k\}$ in terms of $\{\tau_{p,q}, v_r\}$. For a solid with relaxation (an anelastic solid) these relations are

$$\dot{e}_{i,j}(\mathbf{x},t) = \int_0^\infty \chi_{i,j,p,q}(\mathbf{x},t')D_t\tau_{p,q}(\mathbf{x},t-t')dt'\,, \tag{3.3}$$

$$\dot{\Phi}_k(\mathbf{x},t) = \int_0^\infty \mu_{k,r}(\mathbf{x},t')D_t v_r(\mathbf{x},t-t')dt'\,, \tag{3.4}$$

where

$$\begin{aligned} \chi_{i,j,p,q} &= \text{compliance relaxation function } (\mathrm{Pa}^{-1}\mathrm{s}^{-1}),\\ \mu_{k,r} &= \text{inertia relaxation function } (\mathrm{kgm}^{-3}\mathrm{s}^{-1}), \end{aligned}$$

and

$$D_t = \partial_t + v_m\partial_m \tag{3.5}$$

is the time-derivative experienced by an observer when co-moving with the solid with velocity v_m.

Low-velocity linearization of the constitutive relations about the static values yields (De Hoop, 1995):

$$\dot{e}_{i,j}(\mathbf{x},t) = \int_0^\infty \chi_{i,j,p,q}(\mathbf{x},t')[\partial_t\tau_{p,q}(\mathbf{x},t-t') + v_r(\mathbf{x},t-t')\partial_r\tau^{(0)}_{p,q}(\mathbf{x})]dt', \tag{3.6}$$

$$\dot{\Phi}_k(\mathbf{x},t) = \int_0^\infty \mu_{k,r}(\mathbf{x},t')\partial_t v_r(\mathbf{x},t-t')dt', \tag{3.7}$$

in which $\tau_{p,q}^{(0)}$ is the static stress.

In general, the variation of the static stress over space is small with respect to the temporal variation of the dynamic stress so that, for low-amplitude velocities, the term $v_r \partial_r \tau_{p,q}^{(0)}$ in Eq. (3.6) in many cases can be neglected with respect to the term $\partial_t \tau_{p,q}(\mathbf{x}, t)$. Apparently, this strategy suffices for most seismology modeling. Notably, among others, De Hoop (1995), Gershanik (1996) and Aki and Richards (1980, box 8.5, p. 374), the latter in part based on work by Dahlen (1972, 1973), neglect the effects of static stress in their developments and take the stress situation existing just before the occurrence of a seismic event (earthquake, underground explosion, seismic exploration vibrator signal, etc.) and zero strain as the reference state. De Hoop (1995) calculates that in the case of hydrostatic gravity stress, the static stress gradient term elements are roughly of the same or higher order of magnitude as those of the term $\partial_t \tau_{p,q}$ for waves with a characteristic period of 200 s or less, justifying neglecting the static stress gradient term for waves of frequency $f \gg 5$ mHz, say frequencies greater than 0.5 Hz. Dahlen and Tromp (1998, Section 4.3.5) find that the effects of gravity are comparable to those of inertia and elasticity for oscillations with periods on the order of 3000 s, and consequently are ignored routinely in body-wave, regional-wave, and exploration seismology for periods shorter than approximately 30 s, or frequencies higher than approximately 30 mHz.

In our system, we strive for the highest attainable accuracy in measurable quantities, and in Chapter 2 proposed a surface point-source force signal consisting of a pseudo-random sequence modulated onto a 2.5 Hz carrier wave, resulting in a $[sin(x)/x]^2$ main lobe power spectrum extending from 0-5 Hz, with still significant signal energy below 0.5 Hz. Moreover, further system development most certainly will enable the transmission of even lower frequencies. For the stated objectives, in particular the one of finding and measuring earthquake precursors, neglecting the term $v_m \partial_m \tau_{p,q}^{(0)}$ thus may adversely affect the resolution and accuracy of the quantities we want to measure. On the other hand, the static stress field must be known with sufficient accuracy to justify incorporating this term, also in view of neglecting higher-order terms in the linearization process applied. Consequently, for the time being, we take this static stress term along in our further development, but will balance this against knowledge of its accuracy. For instance, if the static stress field is dominated by hydrostatic gravity, this term may be calculated with sufficient accuracy to improve measurement of the wanted

quantities. Ironically, however, exactly in areas where we want to apply our system to perform earthquake precursor measurement, i.e., in areas of interplate tectonic or intraplate Earth dynamics stress, and in the cases of mining or reservoir induced stress, the stress field may be of similar or greater magnitude than the gravity stress field, but its direction and magnitude in general are not known, so that incorporating the static stress term may not make sense.

For an instantaneously reacting solid (an elastic solid) the constitutive relations reduce to

$$\dot{e}_{i,j}(\mathbf{x},t) = S_{i,j,p,q}(\mathbf{x})[\partial_t \tau_{p,q}(\mathbf{x},t) + v_r(\mathbf{x},t)\partial_r \tau^{(0)}_{p,q}(\mathbf{x})]\,, \tag{3.8}$$

$$\dot{\Phi}_k(\mathbf{x},t) = \rho_{k,r}(\mathbf{x})\partial_t v_r(\mathbf{x},t)\,, \tag{3.9}$$

where

$$S_{i,j,p,q} = \text{compliance tensor (Pa)}, \tag{3.10}$$

$$\rho_{k,r} = \text{volume density of mass tensor (kgm}^{-3}). \tag{3.11}$$

After our low-velocity linearization (but keeping the static stress contribution), mathematically we take advantage of this situation by carrying out a Laplace transformation with respect to time and considering the equations governing the elastodynamic wavefield in the corresponding Laplace-transform domain or s-domain. In the s-domain relations, the time coordinate has been eliminated, and a wavefield problem in space remains in which the transform parameter s occurs. Causality of the wavefield is taken into account by taking $\mathrm{Re}(s) > 0$, and requiring that all causal wavefield quantities are analytic functions of s in the right half $0 < \mathrm{Re}(s) < \infty$ of the complex s-plane. In a number of wavefield problems, the transform parameter s is profitably chosen to be real and positive. Furthermore, by considering the limiting case $s = j\omega$, where j is the imaginary unit and ω is real and positive, the complex steady-state representation of sinusoidally in time oscillating wavefields of angular (or circular) frequency ω follows, the complex representation having the complex time factor $\exp(j\omega t)$.

Combining Eqs. (3.1) and (3.2) with Eqs. (3.7) and (3.6), respectively, and assuming that the initial elastodynamic fields are zero, we obtain the following elastodynamic equation in the Laplace domain:

$$-\triangle_{k,m,p,q}\partial_m \hat{\tau}_{p,q} + s\hat{\mu}_{k,r}\hat{v}_r = \hat{f}_k\,, \tag{3.12}$$

$$\triangle_{i,j,m,r}\partial_m \hat{v}_r - s\hat{\chi}_{i,j,p,q}\hat{\tau}_{p,q} = \hat{h}_{i,j} + \hat{\chi}_{i,j,p,q}\hat{v}_r \partial_r \tau^{(0)}_{p,q}\,. \tag{3.13}$$

where $\hat{v}_r = \hat{v}_r(\mathbf{x}, s)$, $\hat{\tau}_{p,q} = \hat{\tau}_{p,q}(\mathbf{x}, s)$, $\hat{f}_k = \hat{f}_k(\mathbf{x}, s)$, $\hat{h}_{i,j} = \hat{h}_{i,j}(\mathbf{x}, s)$, $\hat{\mu} = \hat{\mu}(\mathbf{x}, s)$, and $\hat{\chi}_{i,j,p,q} = \hat{\chi}_{i,j,p,q}(\mathbf{x}, s)$ are the Laplace transforms of $v_r = v_r(\mathbf{x}, t)$, $\tau_{p,q} = \tau_{p,q}(\mathbf{x}, t)$, $f_k = f_k(\mathbf{x}, t)$, $h_{i,j} = h_{i,j}(\mathbf{x}, t)$, $\mu = \mu(\mathbf{x}, t)$, and $\chi_{i,j,p,q} = \chi_{i,j,p,q}(\mathbf{x}, t)$, respectively. Note that we have transferred the term containing the static stress to the right-hand side of Eq. (3.13), so that it is considered a source contribution.

For the special case of purely elastic isotropic, but inhomogeneous media we may replace the constitutive parameters, $\hat{\mu}_{k,r}$ and $\hat{\chi}_{i,j,p,q}$, by

$$\hat{\mu}_{k,r} = \rho\, \delta_{k,r}\,, \tag{3.14}$$

$$\hat{\chi}_{i,j,p,q} = S_{i,j,p,q} = \Lambda \delta_{i,j}\delta_{p,q} + 2M\Delta_{i,j,p,q}\,, \tag{3.15}$$

where $\rho = \rho(\mathbf{x})$ is the scalar volume density of mass and the material parameters $\Lambda = \Lambda(\mathbf{x})$ and $M = M(\mathbf{x})$ are given by

$$\Lambda = \frac{-\lambda}{2\mu(3\lambda + 2\mu)}\,, \quad M = \frac{1}{4\mu}\,,$$

in which $\lambda = \lambda(\mathbf{x})$ and $\mu = \mu(\mathbf{x})$ are the Lamé coefficients. This lossless, isotropic, but inhomogeneous medium serves as the background medium for our wavefield model. We consider the deviations from this background medium as perturbations. Hence, we write the constitutive parameters as a superposition of an isotropic non-dispersive part and a non-isotropic dispersive contribution, viz.,

$$\rho_{k,r} = \rho\delta_{k,r} + \hat{\mu}^{\Delta}_{k,r}\,, \tag{3.16}$$

$$\hat{\chi}_{i,j,p,q} = S_{i,j,p,q} + \hat{\chi}^{\Delta}_{i,j,p,q}\,. \tag{3.17}$$

Substituting these relations into Eqs. (3.12) and (3.13), and transferring the non-isotropic and dispersive parts to their right-hand sides, we obtain

$$-\triangle_{k,m,p,q}\partial_m\hat{\tau}_{p,q} + s\rho\hat{v}_k = \hat{f}_k - s\hat{\mu}^{\Delta}_{k,r}\hat{v}_r\,, \tag{3.18}$$

$$\triangle_{i,j,m,r}\partial_m\hat{v}_r - sS_{i,j,p,q}\hat{\tau}_{p,q} = \hat{h}_{i,j} + s\hat{\chi}^{\Delta}_{i,j,p,q}\hat{\tau}_{p,q} + \hat{\chi}_{i,j,p,q}\hat{v}_r\partial_r\tau^{(0)}_{p,q}\,. \tag{3.19}$$

We rewrite Eqs. (3.18) and (3.19) in a shorter notation, viz.,

$$-\triangle_{k,m,p,q}\partial_m\hat{\tau}_{p,q} + s\rho\hat{v}_k = \hat{f}_k + \hat{f}^{int}_k\,, \tag{3.20}$$

$$\triangle_{i,j,m,r}\partial_m\hat{v}_r - sS_{i,j,p,q}\hat{\tau}_{p,q} = \hat{h}_{i,j} + \hat{h}^{int}_{i,j}\,, \tag{3.21}$$

where $\{\hat{f}_k, \hat{h}_{i,j}\}$ represent the external sources. In our Earth observation system the external force source $\hat{f}_k$ represents the force volume density distribution of our surface vibrator. In that case the injection source $\hat{h}_{i,j}$ is zero. But we keep this latter source distribution in our analysis, because in the case of an earthquake or an underground explosion source, its corresponding moment tensor may be modeled as an external injection source. The terms $\{\hat{f}_k^{int}, \hat{h}_{i,j}^{int}\}$ represent the internal sources due to the presence of (1) the static stress, (2) losses, and (3) anisotropy. These internal sources are given by

$$\hat{f}_k^{int} = -s\hat{\mu}_{k,r}^{\Delta}\hat{v}_r\,, \tag{3.22}$$

$$\hat{h}_{i,j}^{int} = s\hat{\chi}_{i,j,p,q}^{\Delta}\hat{\tau}_{p,q} + \hat{\chi}_{i,j,p,q}\hat{v}_r\partial_r\tau_{p,q}^{(0)}\,. \tag{3.23}$$

3.2 Wave equations for the particle velocity

In analogy to the time domain derivation by De Hoop (1995, Section 10.12), we eliminate the stress tensor from the system of Eqs. (3.18) and (3.21) in favor of a single equation for the particle velocity. To this end, we introduce the stiffness tensor $C_{p,q,i,j} = S^{-1}_{i,j,p,q}$ given by

$$C_{p,q,i,j} = \lambda\delta_{p,q}\delta_{i,j} + 2\mu\Delta_{p,q,i,j}\,, \tag{3.24}$$

resolve $s\tau_{p,q}$ from Eq. (3.21) as

$$s\tau_{p,q} = C_{p,q,i,j}\left(\triangle_{i,j,m,r}\partial_m\hat{v}_r - \hat{h}_{i,j} - \hat{h}_{i,j}^{int}\right), \tag{3.25}$$

and substitute this in Eq. (3.18) multiplied by s, to obtain the elastodynamic wave equation for the particle velocity in our perturbed inhomogeneous, isotropic background medium as

$$\partial_k(\lambda\partial_i\hat{v}_i) + \partial_m(\mu\partial_k\hat{v}_m) + \partial_m(\mu\partial_m\hat{v}_k) - s^2\rho\hat{v}_k = -(\hat{q}_k + \hat{q}^{int})\,, \tag{3.26}$$

with source distributions

$$\hat{q}_k = s\hat{f}_k - \partial_m(C_{k,m,i,j}\hat{h}_{i,j})\,, \tag{3.27}$$

$$\hat{q}_k^{int} = s\hat{f}_k^{int} - \partial_m(C_{k,m,i,j}\hat{h}_{i,j}^{int})\,. \tag{3.28}$$

Let us define the Green tensor $\hat{G}_{k,k'}(\mathbf{x}-\mathbf{x}', s)$ so that it satisfies the wave equation with unit tensor point source at $\mathbf{x} = \mathbf{x}'$, viz.,

$$\partial_k(\lambda\partial_i\hat{G}_{i,k'}) + \partial_m(\mu\partial_k\hat{G}_{m,k'}) + \partial_m(\mu\partial_m\hat{G}_{k,k'}) - s^2\rho\hat{G}_{k,k'} = -\delta_{k,k'}(\mathbf{x}-\mathbf{x}'). \tag{3.29}$$

The solution of the wave equation for the particle velocity then is obtained as

$$\hat{v}_k(\mathbf{x}, s) = \int_{\mathbf{x}'\in\mathbb{R}^3} \hat{G}_{k,k'}(\mathbf{x}, \mathbf{x}', s)[\hat{q}_{k'}(\mathbf{x}', s) + \hat{q}^{int}_{k'}(\mathbf{x}', s)]\mathrm{dV}\,. \tag{3.30}$$

In the special case that the background is homogeneous, the Green tensor is obtained as

$$\hat{G}_{r,k}(\mathbf{x}, \mathbf{x}', s) = \frac{1}{\rho c_S^2}\hat{G}_S\delta_{r,k} + \frac{1}{s^2\rho}\partial_r\partial_k[\hat{G}_P - \hat{G}_S]\,, \tag{3.31}$$

where the scalar Green functions $\hat{G}_P$ and $\hat{G}_S$ are given by

$$\hat{G}_P(\mathbf{x}, \mathbf{x}', s) = \frac{\exp(-s|\mathbf{x}-\mathbf{x}'|/c_P)}{4\pi|\mathbf{x}-\mathbf{x}'|}\,, \quad \hat{G}_S(\mathbf{x}, \mathbf{x}', s) = \frac{\exp(-s|\mathbf{x}-\mathbf{x}'|/c_S)}{4\pi|\mathbf{x}-\mathbf{x}'|}\,, \tag{3.32}$$

with P-wave speed and S-wave speed

$$c_P = \left(\frac{\lambda+2\mu}{\rho}\right)^{\frac{1}{2}}\,, \quad c_S = \left(\frac{\mu}{\rho}\right)^{\frac{1}{2}}\,. \tag{3.33}$$

In the present application the dimensions of the vibrator source which generates the wavefield are much smaller than the dominant wavelength of the pertinent wavefield. This implies that we consider the vibrator source as a point-force source, which is written as

$$\hat{q}^{vib}_k(\mathbf{x}, s) = \hat{Q}_k(s)\,\delta(\mathbf{x}-\mathbf{x}^S)\,, \tag{3.34}$$

with resulting *direct,* or *incident,* particle velocity wave field at a receiver location $\mathbf{x}^R$

$$\hat{v}^{inc}_k(\mathbf{x}^R, \mathbf{x}^S, s) = \hat{G}_{k,k'}(\mathbf{x}^R, \mathbf{x}^S, s)\hat{q}^{vib}_{k'}(\mathbf{x}, s)\,, \tag{3.35}$$

where $\mathbf{x}^S$ is the source location.

In our 3-D transmission system concept, we operate with a number of vibrators transmitting mutually uncorrelated seismic wave signals simultaneously from different source locations. Furthermore, we preserved the option

of also accommodating information obtained from earthquake and explosion sources. Therefore, we would have to integrate the source distribution over a total source domain D_{source} encompassing all possible direct sources. However, the injection source term $-\partial_m(C_{k,m,i,j}\hat{h}_{i,j})$ then considerably complicates our further formulation. Since our work focuses on the seismic wave transmission system with controlled surface point force signals, we leave formulating the incorporation of earthquake and explosion sources for future research, and in our further development consider only our vibrator sources, putting $\hat{h}_{i,j} = 0$. As exposed in Chapter 2, in matched filter signal processing, each vibrator source is uniquely and automatically identified by its pseudo-random sequence modulation code. In view of this, it is convenient to formulate and process our wavefield representation for a single vibrator point source and a single receiver station; the total wavefield then is obtained by superimposing the wavefields generated by all source-receiver combinations. At each receiver station, this is equivalent to adding the seismograms resulting from each single source.

Thus, we write

$$\hat{q}_k(\mathbf{x}, s) = \hat{Q}_k(s)\,\delta(\mathbf{x} - \mathbf{x}^S)\,. \tag{3.36}$$

Substituting this into Eq. (3.30) we obtain the expression for the *total* particle velocity wave field at an observation point $\mathbf{x}^R$ as

$$\hat{v}_k(\mathbf{x}^R, \mathbf{x}^S, s) = \hat{v}_k^{inc}(\mathbf{x}^R, \mathbf{x}^S, s) + \int_{\mathbf{x}\in D_{contrast}} \hat{G}_{k,k'}(\mathbf{x}^R, \mathbf{x}, s)\hat{q}_{k'}^{int}(\mathbf{x}, \mathbf{x}^S, s)\mathrm{dV} \tag{3.37}$$

in which the domain $D_{contrast}$ includes the domain of factual internal contrast with respect to the background. The first term on the right-hand side represents the direct wavefield in the background from source to receiver, denoted as the incident wavefield, which, for a general observation point $\mathbf{x}^R$, and a single source location $\mathbf{x}^S$ is given by

$$\hat{v}_k^{inc}(\mathbf{x}^R, \mathbf{x}^S, s) = \hat{G}_{k,k'}(\mathbf{x}^R, \mathbf{x}^S, s)\hat{Q}_{k'}(s). \tag{3.38}$$

Since the contrast terms depend on the total wavefield, we observe that we are dealing with an essentially nonlinear problem.

In order to have an operational framework, we propose the Born type of linearization, in which the actual wavefield in the contrasting domain is replaced by the background incident wavefield. In Chapter 2 we made plausible that, due to the precise control and selectable code length of the

seismic wave signals emitted, in combination with our novel signal detection and timing algorithm, primary as well as many later seismic phase arrivals can be detected and timed correctly. Ray tracing of these arrivals then provides a sufficient grid for adequate subsurface imaging of the background medium and for definition of its Green tensor.

To be consistent with first order perturbations, we replace the anisotropic compliance relaxation $\hat{\chi}_{i,j,p,q}$ in the last term of Eq. (3.23) with the isotropic compliance $S_{i,j,p,q}$. Then, writing

$$s\tau^{inc}_{p,q} = C_{p,q,i,j}\left(\triangle_{i,j,m,r}\partial_m \hat{v}^{inc}_r\right) = C_{p,q,i,j}\partial_i \hat{v}^{inc}_j\,, \tag{3.39}$$

and combining Eqs. (3.22), (3.23) and (3.28), the contrast sources are approximated by

$$\hat{q}^{int}_k = -s^2\hat{\mu}^{\Delta}_{k,r}\hat{v}^{inc}_r - \partial_m(C_{k,m,i',j'}\hat{\chi}^{\Delta}_{i',j',p,q}C_{p,q,i,j}\partial_i\hat{v}^{inc}_j) - \partial_m(\hat{v}^{inc}_r\partial_r\tau^{(0)}_{k,m}). \tag{3.40}$$

Using the expression for the incident field of Eq. (3.38) we arrive at

$$\hat{q}^{int}_k(\mathbf{x},\mathbf{x}^S,s) = \hat{G}^{int}_{k,k'}(\mathbf{x},\mathbf{x}^S,s)\hat{Q}_{k'}(s)\,, \tag{3.41}$$

in which

$$\begin{aligned}\hat{G}^{int}_{k,k'}(\mathbf{x},\mathbf{x}^S,s) = &-s^2\hat{\mu}^{\Delta}_{k,r}\hat{G}_{r,k'}(\mathbf{x},\mathbf{x}^S,s)\\ &-\partial_m[C_{k,m,i',j'}\hat{\chi}^{\Delta}_{i',j',p,q}C_{p,q,i,j}\partial_i\hat{G}_{j,k'}(\mathbf{x},\mathbf{x}^S,s)]\\ &-\partial_m[\hat{G}_{r,k'}(\mathbf{x},\mathbf{x}^S,s)\partial_r\tau^{(0)}_{k,m}]\,.\end{aligned} \tag{3.42}$$

Substituting Eqs. (3.41), (3.42) and (3.38) in the integral representation of Eq. (3.37), and integrating the terms due to the second and third term in Eq. (3.42) by parts, in which we note that the contrast vanishes on the boundaries of the contrasting domain, we arrive at

$$\begin{aligned}\hat{v}_k(\mathbf{x}^R,\mathbf{x}^S,s) = &\hat{G}_{k,k'}(\mathbf{x}^R,\mathbf{x}^S,s)\hat{Q}_{k'}(s)\\ &-\left[\int_{\mathbf{x}\in D_{contrast}}\hat{G}^{cst}_{k,k'}(\mathbf{x}^R,\mathbf{x},\mathbf{x}^S,s)\mathrm{dV}\right]\hat{Q}_{k'}(s)\,,\end{aligned} \tag{3.43}$$

in which

$$\begin{aligned}\hat{G}^{cst}_{k,k'}(\mathbf{x}^R,\mathbf{x},\mathbf{x}^S,s) = &-\hat{G}_{k,s}(\mathbf{x}^R,\mathbf{x},s)\,s^2\hat{\mu}^{\Delta}_{s,r}(\mathbf{x},s)\,\hat{G}_{r,k'}(\mathbf{x},\mathbf{x}^S,s)\\ &+[\partial_m\hat{G}_{k,s}(\mathbf{x}^R,\mathbf{x},s)]\,\hat{\chi}^{cst}_{s,m,i,j}(\mathbf{x},s)\,\partial_i\hat{G}_{j,k'}(\mathbf{x},\mathbf{x}^S,s)\\ &+[\partial_m\hat{G}_{k,s}(\mathbf{x}^R,\mathbf{x},s)]\,[\partial_r\tau^{(0)}_{s,m}(\mathbf{x})]\,\hat{G}_{r,k'}(\mathbf{x},\mathbf{x}^S,s)\,,\end{aligned} \tag{3.44}$$

where we have introduced a new contrast quantity $\hat{\chi}^{cst}_{s,m,i,j}$ as

$$\hat{\chi}^{cst}_{s,m,i,j} = C_{s,m,i',j'} \hat{\chi}^{\Delta}_{i',j',p,q} C_{p,q,i,j}. \tag{3.45}$$

The latter quantity constitutes in a complicated fashion the non-isotropic dispersive contribution in the compliance. After determination of the perturbation quantities, $\hat{\mu}^{\Delta}_{s,r}$, $\hat{\chi}^{cst}_{s,m,i,j}$, $\partial_r \tau^{(0)}_{s,m}$, from some inversion method, the actual contrast quantity $\hat{\chi}^{\Delta}_{i',j',p,q}$ can be determined by using the tensorial inversion rules, operating with the inverse of $C_{i,j,p,q}$.

In the Born approximation of equations (3.43) and (3.44) we clearly identify the transmission path from source $\mathbf{x}^S$ to the (unknown) interior contrast location at $\mathbf{x}$ back to the receiver position $\mathbf{x}^R$. This wave propagation is formulated by the Green tensors of the background medium. Up to this point we did not make any decision on how to perform the computation of these Green tensors. To facilitate these computations and to have a fast way to implement this in an inversion scheme, we propose to apply the body wave ray-theoretical approximation of the Green tensors. To this end, in the next section we consider the elements of the body wave ray theory necessary to reconstruct the Green tensor. We carry out this analysis in the time domain and transform the results to the frequency domain in order to use them in our representation, Eqs. (3.43) and (3.44).

3.3 Propagation in an inhomogeneous background: body wave ray theory

For the *approximate* wave equation solution for an inhomogeneous isotropic background (the *geometrical ray solution*), we adopt the basic body wave ray theory as found in standard texts (e.g., Aki and Richards (1980, Section 4.4), Dahlen and Tromp (1998, chapters 12, 15), and Lay and Wallace (1995, Chapter 3). Most of the theory is derived from the *eikonal equation*; the validity for its application in seismic wave propagation is subject to various *constraints* allowing the approximations applied. In order to establish at the outset the limitations or restrictions for this theory, we analyze these constraints with respect to our proposed signal transmission system. Next, we analsye ray tracing and Green tensor aspects, and consider the consequences for static and time-lapse tomography.

3.3.1 Ray theory constraints

Ray theory applies to:

1. *Far-field* particle motion: $\omega r/c \gg 1$, or $r \gg \lambda$, where ω is the radial frequency, r is the raypath length, c is the wave propagation speed, and λ is the wavelength. This means considering wave behavior at least several wavelengths away from the source.
2. *Smoothly varying* Earth properties, defined by Dahlen and Tromp (1998) as $\lambda \ll \Lambda$, where Λ is the distance over which the Earth properties change significantly.

Both constraints indicate that seismic wave ray theory is valid only for relatively high frequency body waves. In fact, several derivations, including the JWKB solution, are strictly valid only in the limit as $\omega \to \infty$. It then seems curious that usually bodywaves are studied in the 1- 5 Hz frequency range, in particular also in view of the present-day availability of broad-band (0.001-50 Hz) seismograms. Probably the reason for this is that, due to exponentially increasing attenuation with frequency, higher frequency body waves carry little energy in the far field, and body wave theory breaks down at lower frequencies, in part because of the far-field constraint, and in part because in most approximations only terms in the lowest order of ω^{-1} are retained, necessitating at least $\omega > 1$.

In our project, the suggested force signal has a $\sin(x)/x$, 0-5 Hz amplitude spectrum with its main energy in the 1-4 Hz frequency band. Thus, for the main-energy band, body wave ray theory seems adequate, at least to the same approximation extent as in earthquake seismology, for describing the geometrical raypaths and the main features at far-field positions and receivers. But uncertainty exists on the behavior in the near field and in the frequency band 0-1 Hz. This is also of concern in order to take advantage of the mentioned present availability of modern broad-band seismometry, and in view of the likelihood that development of low-frequency controlled-signal sources becomes feasible. It appears, therefore, that development of a low-frequency body wave propagation theory is becoming highly desirable. Such development is beyond the immediate objectives of the present work.

Aki and Richards (1980) define a *wavefront* as a propagating discontinuity in a variable of physical interest or in one of its derivatives (e.g., particle displacement, velocity, acceleration). The body waves travel as wavefronts

with local propagation speed along *ray paths* following Snell's law, with amplitudes determined by the source force and radiation pattern, and by the geometrical spreading of the rays between source and receivers. The form of the *far-field* Green function P- and S-wave solutions for homogeneous isotropic media, Eq. (3.31), is generalized for *smoothly varying inhomogeneous isotropic media* using *ray coordinates.* The travel time $T(\mathbf{x}, \mathbf{x}')$ from a point source at position $\mathbf{x}'$ to a given location $\mathbf{x}$ is obtained by integrating the wavefront *slowness* (the inverse of the propagation speed) along the ray path s.

Aki and Richards (1980) consider the particle displacement wave equation

$$\rho \partial_t^2 u_i = \partial_j \tau_{i,j} \tag{3.46}$$

with

$$\tau_{i,j} = C_{i,j,k,l} \partial_l u_k \,, \tag{3.47}$$

corresponding to the homogeneous form (all source terms set equal to zero) of our Eqs. (3.20) and (3.25), and pose an *ansatz* solution in a generally *inhomogeneous anisotropic* medium of the form

$$u_k(\mathbf{x}, t) = U_k(t - T) A(\mathbf{x}) \,, \quad \mathbf{x} \neq \mathbf{x}' \,, \tag{3.48}$$

where U_k is the time-dependent, but not location-dependent, pulse shape and A is the location-dependent, but not time-dependent, amplitude. U_k and its time derivatives near a wavefront are assumed to "fluctuate much more rapidly than A or $C_{i,j,k,l}$". This is argued to lead to

$$det(\rho \delta_{i,k} - C_{i,j,k,l} \partial_j T \partial_l T) = 0 \,, \tag{3.49}$$

which determines the possible wavefronts in an elastic medium because of its constraint on the function $T(\mathbf{x}, \mathbf{x}')$. For an isotropic medium, the latter equation results in the eikonal equation

$$|\nabla T|^2 = \frac{1}{c^2} \,, \tag{3.50}$$

where c is either the local P-wave speed, or the local S-wave speed.

The quoted constraint on waveform temporal fluctuation rapidity vs. spatial variation in A and C, is stated only *qualitatively* by the authors; *quantitatively,* we may elucidate as follows. Consider a weakly inhomogeneous solid with fractional propagation speed spatial variation $\frac{dc}{c}$ per unit

length. If f is the waveform frequency, and s the raypath length, the constraint suggests that

$$dc/ds \ll f\,, \tag{3.51}$$

or

$$\frac{dc}{c}/ds \ll \frac{f}{c} = \frac{1}{\lambda}\,, \tag{3.52}$$

or

$$\lambda \ll \frac{ds}{dc/c}\,. \tag{3.53}$$

For instance, $\frac{dc}{c}/ds = 1\%$ per km requires $\lambda \ll 100$ km. For 1-5 Hz body waves in the crust with $c =$ 2-6 km/s, the wavelength is 0.5-6 km, satisfying the constraint concerned. The approximations become invalid as $\frac{dc}{c}/ds > 10\%$ per km. A similar reasoning can be held for the constraint in the variation in A, with

$$\frac{dA}{A}/ds \ll \frac{f}{c} = \frac{1}{\lambda}\,, \tag{3.54}$$

leading to

$$\lambda \ll \frac{ds}{dA/A}\,. \tag{3.55}$$

Dahlen and Tromp (1998, Chapter 15) consider high-frequency body waves in a general *non-rotating, elastic, isotropic* (NREI) Earth model $\bigoplus = \bigoplus_S \cup \bigoplus_F$ composed of *concentric* solid and fluid regions separated by non-intersecting free-surface, solid-solid, or fluid-solid interfaces $\Sigma = \partial \bigoplus \cup \Sigma_{SS} \cup \Sigma_{FS}$ with outward unit normal $\hat{\mathbf{n}}$. Between the interfaces, the Earth may contain arbitrarily large, but sufficiently *smooth* variations, the latter being defined as satisfying $\lambda/\Lambda \ll 1$, where λ is the wavelength and Λ is the distance over which the Earth properties change significantly. This smoothness definition also determines the frequency band valid for this approximation theory. In our project, the transmission power spectrum is a $[\sin(x)/x]^2$, $x = \pi\,(f - f_0)\,/f_0$ function centered at $f = f_0$, with, for instance, $f_0 = 2.5$ Hz. This carrier frequency and, e.g., $c = 6$ km/s, results in $\lambda = 2.4$ km, leading to the requirement $\Lambda \gg 2.4$ km.

3.3.2 Ray tracing and Green tensor

The geometrical raypaths between any two points $\mathbf{x}', \mathbf{x}$ may be obtained by a number of different *ray tracing* methods. Dahlen and Tromp (1998) describe kinematic and dynamic ray tracing algorithms. Two basic methods

for numerical ray tracing between given source and receiver locations are *"ray shooting"* and *"ray bending"*. In "ray shooting", trial values for the source incidence angle are used and iteratively adjusted in order to "hit" the receiver. In the "ray bending" method, trial raypaths through correct source and receiver locations are adjusted to fit the geometrical ray equations. Several 3-D ray tracing methods in seismic tomography applications are discussed in the literature, e.g., Papazachos and Nolet (1997), Moser (1991), Julian and Gubbins (1977), Sambridge (1990), Moser, Nolet, and Snieder (1992), Thurber and Elsworth (1980), Wielandt (1987), Bijwaard and Spakman (1999). The literature reflects that 3-D ray tracing in smoothly inhomogeneous media, using large source-receiver data bases obtained from earthquakes and underground explosions, now seems well established and can be performed within reasonable computer time. These methods may be adapted to accommodate data obtained with our proposed controlled-signal seismic transmission system. In the 2-D source-receiver configuration transmission simulation presented in Chapter 2, we performed ray tracing by applying a for this purpose developed finite-element "shooting" method algorithm.

The ray tracing process yields the spatial propagation velocity distribution, the raypath geometry, the raypath length, the polarization vectors, and the travel time T along each ray or along particular sections of a ray. Symbolically, these parameters can be combined in an expression for the ray-theoretical Green tensor, as discussed below.

Dahlen and Tromp (1998) arrive at a frequency domain generic, *far-field ray-theoretical Green tensor* over all possible rays between a given source location $\mathbf{x}^S$ and an observation point $\mathbf{x}$:

$$\hat{G}_{r,k}(\mathbf{x}^S, \mathbf{x}, j\omega) = \sum_{\text{rays}} \eta_r \eta_k^S \left(\rho\rho^S c (c^S)^3\right)^{-1/2} \Pi \frac{\exp(-j\omega T + jM\pi/2)}{4\pi\mathcal{R}}, \quad (3.56)$$

where the superscript S refers to the source location $\mathbf{x}^S$, $\mathbf{x}$ is a point along the ray, η_r are the polarization unit vectors, Π is the product of all forward and backward scattering matrices at the concentric boundaries, comprising reflection/transmission coefficients and polarization transitions, $\mathcal{R} = \mathcal{R}(\mathbf{x}^S, \mathbf{x})$ is the geometric spreading factor, $T = T(\mathbf{x}^S, \mathbf{x})$ is the travel time between $\mathbf{x}^S$ and $\mathbf{x}$, and M is the Maslov index indicating the number of times the wave encounters a caustic and consequently undergoes a Hilbert transform. Figure 3.1 illustrates the ray-theoretical Green tensor by showing some crustal

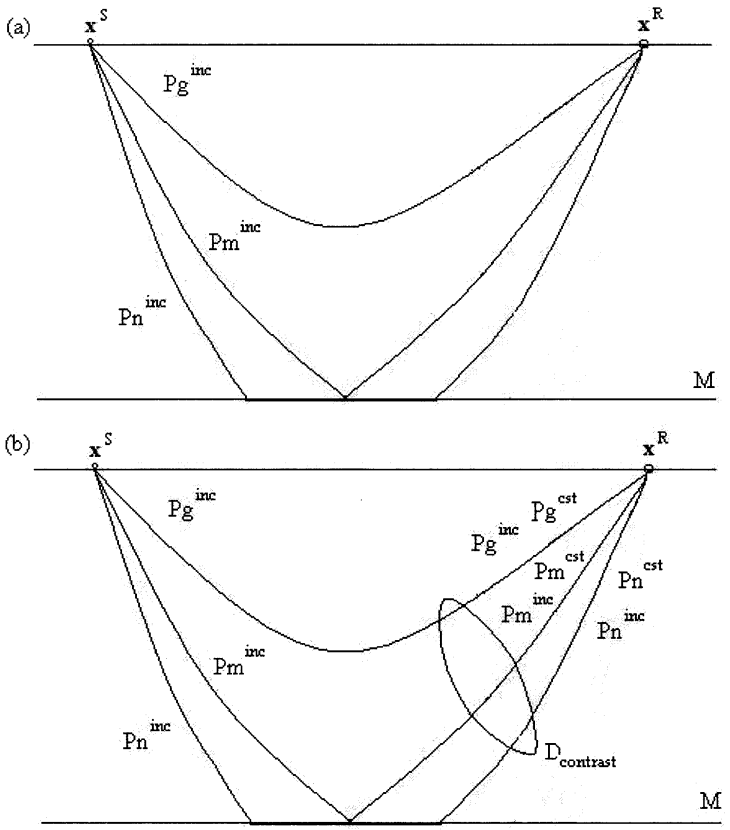

Figure 3.1: Schematic illustration of the ray-theoretical Green tensor: (a) in a medium without contrast sources, (b) in a medium with contrast sources. For clarity, only a few crustal P-waves are drawn.

P-wave phases generated by an external source in a medium without and with contrast sources. Our 2-D transmission simulation in Chapter 2, Figures 2.33-2.38, illustrates the incident wavefield time domain process for two external vibrator sources for direct P-waves and first M-reflected P-waves.

For an isotropic *homogeneous* medium, Eq. (3.56) becomes the far-field Green function given in Eq. (3.31). In that case, the raypath is a straight line connecting point source and receiver, $\mathcal{R} = \left|\mathbf{x} - \mathbf{x}^S\right|$, $\rho^S = \rho$, $c^S = c$, there are no caustics so that $M = 0$ (no Hilbert transform executed), and there are no boundaries so that $\Pi = I$.

The ray-theoretical Green function is to be used in all direct and indirect

source-receiver transmissions, i.e., wherever it appears in Eqs. (3.43) and (3.44), expressed in the frequency domain by replacing s with $j\omega$, viz.

$$\hat{v}_k(\mathbf{x}^R, \mathbf{x}^S, j\omega) = \hat{G}_{k,k'}(\mathbf{x}^R, \mathbf{x}^S, j\omega)\hat{Q}_{k'}(j\omega) - \left[\int_{\mathbf{x}\in D_{contrast}} \hat{G}^{cst}_{k,k'}(\mathbf{x}^R, \mathbf{x}, \mathbf{x}^S, j\omega)\mathrm{dV}\right] \hat{Q}_{k'}(j\omega)\,, \tag{3.57}$$

in which

$$\begin{aligned}\hat{G}^{cst}_{k,k'}(\mathbf{x}^R, \mathbf{x}, \mathbf{x}^S, j\omega) = {} & \hat{G}_{k,s}(\mathbf{x}^R, \mathbf{x}, j\omega)\,\omega^2\,\hat{\mu}^{\Delta}_{s,r}(\mathbf{x}, j\omega)\,\hat{G}_{r,k'}(\mathbf{x}, \mathbf{x}^S, j\omega) \\ & + [\partial_m \hat{G}_{k,s}(\mathbf{x}^R, \mathbf{x}, j\omega)]\,\hat{\chi}^{cst}_{s,m,i,j}(\mathbf{x}, j\omega)\,\partial_i \hat{G}_{j,k'}(\mathbf{x}, \mathbf{x}^S, j\omega) \\ & + [\partial_m \hat{G}_{k,s}(\mathbf{x}^R, \mathbf{x}, j\omega)]\,[\partial_r \tau^{(0)}_{s,m}(\mathbf{x})]\,\hat{G}_{r,k'}(\mathbf{x}, \mathbf{x}^S, j\omega)\,.\end{aligned} \tag{3.58}$$

3.4 Final considerations

In our controlled vibrator signal transmission system concept, the external source $\hat{Q}_{k'}$ in Eq. (3.57) can be written as

$$\hat{Q}_{k'} = j\omega A\hat{F}\,(j\omega)\,e_{k'}\,, \tag{3.59}$$

in which A is the vibrator force signal amplitude, $\hat{F}\,(j\omega)$ is the Fourier transform of the time domain *unit* amplitude vibrator force scalar signal signature $F\,(t)$, and $e_{k'}$ is the force direction unit vector. In the signal processing part of our transmission system, at each seismometer component we first demodulate the received signal, and subsequently match-filter the demodulated signal to the unit amplitude force modulating signature $F_{\mathrm{mod}}\,(t)$, i.e., we time-correlate the demodulated signal with $F_{\mathrm{mod}}\,(t)$. In the frequency domain, demodulation is equivalent to replacing ω with $\omega' = \omega - \omega_0$, i.e., translating all frequencies about the carrier frequency ω_0 to frequencies about dc; matched filtering is equivalent to multiplying the demodulated signal with the complex conjugate $\hat{F}^*_{\mathrm{mod}}\,(j\omega) = \hat{F}^*\,(j\omega')$ of $\hat{F}_{\mathrm{mod}}\,(j\omega) = \hat{F}\,(j\omega')$. For a linear Earth transfer function or Green function $\hat{G}_{k,k'}$, this process trans-

forms Eq. (3.57) into the matched filter output

$$\hat{v}_k(\mathbf{x}^R, \mathbf{x}^S, j\omega')\hat{F}^*\left(j\omega'\right) = \hat{G}_{k,k'}(\mathbf{x}^R, \mathbf{x}^S, j\omega')j\omega' A\left|\hat{F}\left(\omega'\right)\right|^2 e_{k'} - \left[\int_{\mathbf{x}\in D_{contrast}} \hat{G}^{cst}_{k,k'}(\mathbf{x}^R, \mathbf{x}, \mathbf{x}^S, j\omega')\mathrm{dV}\right] j\omega' A\left|\hat{F}\left(\omega'\right)\right|^2 e_{k'} . \tag{3.60}$$

The left-hand side of Eq. (3.60) corresponds to the Fourier transform of the observed time domain complex-envelope correlogram or seismogram. The quantity $\left|\hat{F}\left(\omega'\right)\right|^2$ is the $[\sin(x)/x]^2$, $x = \omega'/2f_0$ power density spectrum of the pseudo-random sequence vibrator force modulating signal, or, equivalently, the Fourier transform of the pseudo-random sequence auto-correlation function, as displayed in Chapter 2.

We remark that, in analogy of our static stress, anisotropy and losses perturbation models, we may model any wave propagation non-linearity as an additional perturbation in the form of an additional contrast source. For the moment, we will consider this to be incorporated in the other contrast sources.

At this stage, the *static* medium properties, including anisotropy and losses, are defined within the background medium limitations mentioned. Any deviations from this model will cause perturbation of the ray-theoretical Green tensor and result in additional contrast sources, thus distorting the contrast sources modeled.

Our main objective is to locate, map, and characterize earthquake preparation zones emerging in *lapsed time*. This is to be performed by means of time-lapse seismic tomography. In our space-time stationary transmission system, any change in Earth physics parameters, potentially reflecting an earthquake preparation process, will cause changes in travel time, amplitude, and spectrum of the signals from rays passing through this potential earthquake preparation zone. The location and geometry of the earthquake preparation zone may be found from the intersections of rays experiencing time-lapse differences in travel time. Its character, i.e., the time-lapse perturbation in static stress, anisotropy and losses, modeled as newly emerging contrast sources, is to be determined from contrast source inversion, through our integral representation, of the observed time-lapse differences in the particle velocity matched-filter output spectrum, i.e., the complex-envelope seis-

mogram spectrum. We note that time-lapse differential measurement cancels any model errors incurred in our representation.

Chapter 4

Conclusions

With the principal objective to enhance earthquake prediction feasibility, we have argued the need for, and the technological feasibility of, realizing a seismic transmission system capable of continuously monitoring the Lithosphere for changes in Earth physics quantities. The *need* for such a system arises from concise formulation of the general earthquake prediction problem, and from reviewing theoretical earthquake preparation process models as well as attempts to probe the Earth for potential earthquake precursors. The literature suggests that for magnitude $M = 4$, $M = 6$, $M = 8$ earthquakes, respectively, the precursor times would be on the order of one month, one year, and seventeen years, and the radii of possible precursor activity 0.6, 6.2, and 65 km. Precursory observables may be small, requiring high resolution measurement. The review leads us to the conclusion that at the present time no adequate system exists to perform the required monitoring functions with sufficient space-time resolution in a systematic, objective manner. The technical *feasibility* of realizing a system satisfying our objectives was demonstrated by presenting the concept, the design layout, and technical details of a seismic transmission system capable of precise, continuously repeated measurement, identification, and statistics compilation of potential earthquake precursors in the form of observed changes in elapsed time in Earth physics quantities governing wave propagation behavior.

Such a system requires the precisely controlled, long-term phase coherent transmission and processing of coded seismic signals covering the 1-5 Hz or broader body wave frequency band, for indefinite duration. The relatively

low frequencies ensure far and deep penetration; the body wave frequency band facilitates the application of body wave ray tracing methods for subsurface imaging. Moreover, in this frequency band, the signals can be adequately received, recorded, and processed at existing and next-generation permanent and portable digital seismic stations worldwide. The signals are to be retrieved by long-term coherent, synchronous stacking of, and correlation (matched filtering) with, the emitted signal code. The 'indefinite duration' of coherent signal transmission and processing is required (1) to emit, over extended time, sufficient coherent signal energy to obtain, after signal energy compression by matched filtering, adequate signal-to-noise ratios over at least regional transmission ranges, and (2) to provide elapsed time signal comparison over precursor time periods of weeks, months, years, and longer. To optimize the attainable information, the signal code must be of sufficient length to generate seismograms which can accommodate the primary and major later seismic phase arrivals.

In our system concept, we achieve these goals by incorporating features taken from communications technology, and by deploying new-technology seismic sources. The communications technology concepts include long-term coherent pseudo-random sequence signal transmission and quadrature matched filter signal processing, resulting in phase coherent complex-envelope seismograms of selectable, sufficient duration, consisting of the dual time series of instantaneous amplitude and instantaneous phase. Families of pseudo-random sequences which are mutually uncorrelated, but are of identical length, and possess identical signal spectra, can be selected as the modulating signal code to enable three-dimensional, simultaneous signal transmission from different source sites. Concerning seismic sources suitable for our transmission system, existing seismic vibrator technology cannot adequately perform the functions required. For that reason, we conceived, and partially developed, a magnetic levitation P-wave vibrator and a linear synchronous motor S-wave vibrator as surface point-force sources, both allowing precisely controlled, long-term phase coherent, low-frequency signal emission, and accommodating a broad class of signal signatures, including the conventional 'chirp' signal used in commercial exploration, and the fast changing pseudo-random sequence signals.

Regarding the complex-envelope seismogram, we showed that the instantaneous phase is more sensitive than the instantaneous amplitude in the detection of low signal-to-noise ratio (<6 B) signals. It is also the instantaneous phase which provides by far more precise signal arrival time information; for

noise-free signals the timing resolution equals the computer´s least significant bit. Taking advantage of these important features, and considering that propagation velocity change, measured as signal travel time deviation, is one of the most prominent earthquake precursors, we developed a new signal detection and timing algorithm operating on coherent complex-envelope seismogram ensembles of the instantaneous phase. From signal-plus-noise vector diagram geometry, and based on the probability distribution of the instantaneous phase of normally distributed seismic noise, we derived a closed-form relation between signal arrival time error and signal-to-noise ratio. The timing error standard deviation ranges from less than 0.5 millisecond at 36 dB and higher seismogram signal-to-noise ratio to less than 0.5 second at -6 dB signal-to-noise ratio. This range, in combination with the capability of selecting seismogram lengths of approximately 15 minutes or longer, permits the detection and timing of primary and many later seismic phase arrivals, thus optimizing the quantity and quality of attainable potential precursor data, as well as providing, in principle, sufficient information to perform regional 3-D ray-tracing and travel time tomography with as few as three seismic vibrator sources, with an anticipated spatial resolution on the order of 10 km, for a distribution of one station per 10 km. The reciprocal of the timing error standard deviation in each detected arrival can be used as a reliability weight in inversion algorithms. Extrapolation of existing hydraulic vibrator transmission data suggests that sufficient signal-to-noise ratio over regional distances is obtained from 1-2 weeks coherent, continuous signal transmission and processing. We illustrated controlled-signal seismic wave transmission, ray tracing, and signal processing by simulating a 2-D source-receiver configuration transmission; the simulation supports the feasibility of performing seismic tomography with only a limited number of controlled-signal sources.

Formulating the transmission problem in the mathematical wave propagation and radiation context, we found that, in view of the low frequency energy present in our suggested 0-5 Hz, $[\sin(x)/x]^2$ power density spectrum pseudo-random sequence signal transmission, in contrast to most literature, the static stress gradient term, if known with sufficient accuracy, should not be neglected. Accordingly, we take this term to the right-hand side of the particle velocity wave equation and consider it as an extra source term. Deviating from conventional formulation of wave propagation in an anisotropic, anelastic, inhomogeneous medium, we model anisotropy and anelasticity as perturbations in the wave propagation in a generally isotropic, but inhomoge-

neous medium. These perturbations take on the form of contrast-in-medium sources. This allows us to take a uniform approach by expressing all three perturbations static stress, anisotropy, and anelasticity, as contrast sources in an inhomogeneous, isotropic background medium. Adopting body wave ray theory to describe the background medium Green function tensor, we arrived at integral representations for contrast source inversion from which the static stress, anisotropy, and anelasticity perturbations are to be resolved.

Viewing an earthquake preparation zone as an *emergent heterogeneity,* we proposed to solve for its contrast-in medium source parameters by performing elapsed-time *travel time tomography* to obtain the preparation zone geometry, volume, and orientation, and applying *3-D contrast source inversion* methods to estimate its essential Earth physics parameters in the broadest sense, i.e., for a generally anisotropic, inhomogeneous, anelastic medium, as deviations in its inertia relaxation tensor function $\mu_{r,k}$, and in its compliance relaxation tensor function $\chi_{r,k,p,q}$.

With the system features mentioned, we believe to have made plausible that our proposed system is capable of providing sufficient, high-resolution data to enable successful execution of these tomography and inversion methods. This data, obtained by *active* seismic transmission may be augmented by *passive* tomography data from earthquake and underground explosion data bases worldwide. If we succeed in mapping the earthquake preparation zone in this manner, and monitoring its evolution, these results should give greater insight in the earthquake preparation mechanics and physics, and possibly provide well-defined, short-term precursors providing estimates of earthquake location, volume, orientation, onset time, magnitude, and Earth physics parameter perturbation.

We did not elaborate on the actual inversion algorithms to be applied, but obviously, contrast source inversion methods, for instance such as successfully applied in electromagnetics (Van den Berg and Kleinman, 1997; Abubakar, 2000), are prime candidates for development into elastodynamic applications.

In addition to our main objective of advancing earthquake prediction feasibility, the system may be applied in general seismology research and seismic tomography experiments, in seismic engineering to measure the response of local soil conditions, buildings, or mechanical structures to remotely generated controlled seismic wave motion, and in reservoir parameter monitoring for oil, gas, and water resource management. Regional controlled-signal to-

mography may improve earthquake and explosion re-location procedures, and enhance Nuclear Test Ban Treaty compliance verification, by providing velocity profile data for seismograph network calibration (Firbas, Fuchs, and Mooney, 1998) and by improving explosion yield estimation through better knowledge of Lithosphere heterogeneity.

Bibliography

Abubakar, A., 2000. Three-Dimensional Non-Linear Inversion of Electrical Conductivity. PhD Thesis. Delft University Press, Delft.

Aki, K. & P.G. Richards, 1980. *Quantitative Seismology.* Freeman, New York.

Baeten, G., 1989. *Theoretical and Practical Aspects of the Vibroseis Method.* PhD Thesis. Delft University of Technology, Department of Applied Earth Sciences. Delft, The Netherlands.

Berg, P.M. van den, & R. E. Kleinman, 1997. A Contrast Source Inversion Method. *Inverse Problems*, 13, 1607-1620.

Bijwaard H. & W. Spakman, 1999. Fast Kinematic Ray Tracing of First-and-Later-Arriving Global Seismic Phases. *Geophysics J.Int.* 139, 359-369.

Byerlee, J., 1977. Friction of Rocks. *Proc. of Conference II. Experimental Studies of Rock Friction with Application to Earthquake Prediction.* Menlo Park, California, 55-77.

Byerlee, J., 1978. A Review of Rock Mechanics Studies in the United States Pertinent to Earthquake Prediction. *Pageoph.*, 116, Nos. 4/5. 586-602.

Clymer, R.W. & T.V. McEvilly, 1981. Travel-Time Monitoring with Vibroseis, *Bull. Seismol. Soc. Am.*, 71, No.6, 1903-1927.

Cunningham, A.B., 1979. Some Alternative Vibrator Signals. *Geophysics*, 44, 1901-1921.

Dahlen, F.A., 1972. Elastic Dislocation for a Self-Gravitating Elastic Configuration with an Initial Static Stress Field. *Geophys. J.R Astr. Soc.*, 28, 357-383.

Dahlen, F.A., 1973. Elastic Dislocation Theory for a Self-Gravitating Elastic Configuration with an Initial Static Stress Field. II. Energy Release. *Geophys. J.R. Astr. Soc.*, 31, 469-484.

Dahlen, F.A. & J. Tromp, 1998. *Theoretical Global Seismology*, Princeton University Press. Princeton, New Jersey.

Dambara, T., 1966. Vertical Movements of the Earth's Crust in Relation to the Matsushiro Earthquake. *J. GSJ.*, 12, 18-45.

Dillen, W.P., H.M.A. Cruts, J. Groenenboom, J.T. Fokkema & A.J.W. Duijndam, 1999. Ultrasonic Velocity and Shear-Wave Splitting Behavior of a Colton Sandstone under a Changing Triaxial Stress. *Geophysics*, 64, No.5, 1603-1607.

Edelmann, H.A.K. & K. Helbig., 1984. Vibroseis - Theory and Practice. *Continuing Education for Explorationists.* EAEG, London.

Firbas, P., K. Fuchs & W.D. Mooney, 1998. Calibration of Seismograph Network May Meet Test Ban Treaty's Monitoring Needs. *Eos, Trans., AGU*, 79, no.35, 414,421.

Geller, R.J., 1997. Earthquakes: Thinking About the Unpredictable. *Eos, Trans., AGU*, 78, 63-67.

Gershanik, S., 1996. *Sismología.* Facultad de Ciencias Astronómicas y Geofísicas, Universidad Nacional de La Plata, Argentina.

Golomb, S.W. 1967. *Shift Register Sequences.* Holden Day, Inc., Amsterdam.

Gusev, A., 1998a. Earthquake Precursors: Banished Forever? *Eos, Trans.*, AGU, 79, 71-72.

Gusev, A., 1998b. Reply to "Comment: Unpredictability of Earthquakes – Truth or Fiction?" *Eos, Trans., AGU*, 79, 373.

Hadley, 1973. Laboratory Investigations of Dilatancy and Motion on Fault Surface at Low Confining Pressure. Proc. Conf. on Tectonic Problems on the San Andreas Fault System. R.L. Kovach and A. Nur, (eds), *Geol. Sciences XIII*, Stanford Univ., 427-435.

Hoop, A.T. de, 1995. *Handbook of Radiation and Scattering of Waves.* Academic Press Ltd., New York.

Julian, B.R. & D. Gubbins, 1977. Three-Dimensional Seismic Ray Tracing. *J. Geophys.*, 43, 95-113.

Kampen, W.A. van, A.R. Ritsema & R. Unger, 1987. *Electromagnetic Vibrator for Seismic and Civil Engineering Applications.* European Patent Application # 87200865.1, United States Patent Application # 48223.

Karageorgi, E., R. Clymer & T.V. McEvilly, 1992. Seismological Studies at Parkfield II. Search for Temporal Variations in Wave Propagation Using Vibroseis. *Bull.*

Seismol. Soc. Am., 82, 1388-1415.

Karageorgi, E., T.V. McEvilly & R.Clymer, 1997. Seismological Studies at Parkfield IV: Variations in Controlled-Source Waveform Parameters and Their Correlation with Seismicity, 1987 to 1995. *Bull. Seismol. Soc. Am.*, 87, No.1, 39-49.

Kasahara, K., 1981. *Earthquake Mechanics.* Cambridge University Press.

Lay T. & T.C. Wallace, 1995. *Modern Global Seismology.* Academic Press, Inc. San Diego, CA.

Lomnitz, C., 1994. *Fundamentals of Earthquake Prediction.* Wiley, New York.

Lomnitz, C., 1998. Comment: Unpredictability of Earthquakes – Truth or Fiction? *Eos, Trans., AGU*, 79, 373.

McEliece, R.J., 1987. *Finite Fields for Scientists and Engineers.* Kluwer, Boston.

Miller, G.F. & H. Pursey, 1954. The Field and Radiation Impedance of Mechanical Radiators on the Free Surface of a Semi-Infinite Isotropic Solid. *Proc. R.Soc.*, A223, 521-541.

Moser, T.J., 1991. Shortest Path Calculation of Seismic Rays. *Geophysics*, 56, 59-67.

Moser, T.J., G. Nolet & R. Snieder, 1993. Ray Bending Revisited. *Bull. Seismol. Soc.Am.*, 82, 259-288.

Papazachos, C.B. & G. Nolet, 1997. Non-linear Arrival Time Tomography. *Annali Di Geofisica*, XL, No.1, 85-97.

Papoulis, A., 1965. *Probability, Random Variables, and Stochastic Processes.* McGraw-Hill Book Company, New York.

Papoulis, A., 1991. *Probability, Random Variables, and Stochastic Processes.* Third edition. McGraw-Hill, Inc., New York.

Rikitake, T., 1981. *Current Research in Earthquake Prediction I.* Center for Academic Publications, Tokyo; Reidel Publishing Company, Dordrecht.

Roden, Martin. 1982. *Digital and Data Communications Systems.* Prentice-Hall, Inc.: Englewood Cliffs, N.J.

Safar, M.H. 1984. On the Determination of the Downgoing P-Waves Radiated by the Vertical Seismic Vibrator. *Geophys. Prospecting*, 32, 392-405.

Sallas, J.J. 1984. Seismic Vibrator Control and the Downgoing P-Wave. *Geophysics*, 49, 732-740.

Sambridge, M.S. 1990. Non-Linear Arrival Time Inversion: Constraining Velocity

Anomalies by Seeking Smooth Models in 3D. *Geophys. J. Int.*, 102, 653-677.

Schwartz, M., 1970. *Information, Transmission, Modulation, and Noise*, McGraw-Hill, London.

Steinberg, J.C. & T.G. Birdsall, 1966. Underwater Sound Propagation in the Straits of Florida, *J. Acoustical Soc. of Am.*, 39, No. 2, 301-315.

Sobolev, G.A., 1978. Physical Processes During the Earthquake Preparation Period: Experiment and Theory. *Pageoph.*, 116, 281-310.

Thurber, C.H. & W.L. Ellsworth, 1980. Rapid Solution of Ray Tracing Problems in Heterogeneous Media. *Bull. Seismol. Soc. Am.*, 70, 1137-1148.

Unger, R. & R. Veenkant, 1967a. Underwater Sound Propagation in the Straits of Florida: The MIMI Experiment of 3 and 4 February 1965, *Cooley Electronics Laboratory Technical Report*, 183, The University of Michigan, Ann Arbor.

Unger, R. & R. Veenkant, 1967b. Underwater Sound Propagation in the Straits of Florida. *Cooley Electronics Laboratory Technical Report*, 186, The University of Michigan, Ann Arbor.

Unger, R., 1981a. The Instantaneous Amplitude, Phase and Frequency in Seismic Event Detection, Timing and Identification. In: E.S. Husebye & S. Mykkeltveit (eds), *Identification of Seismic Sources – Earthquake or Underground Explosion*, D. Reidel, Dordrecht, 649-662.

Unger, R. 1981b. Regional Seismology in Argentina. *Technical Report.* Facultad de Ciencias Exactas y Tecnología, Universidad Nacional de Tucumán. Argentina.

Unger, R., W.A. van Kampen, A.J. Berkhout, R.G. Boiten, A.R. Ritsema, D.Ph. Schmidt & A.M. Ziolkowski, 1987. New Possibilities in Controlled-Source Seismology with a Magnetic Levitation Vibrator. *Geophys. J.R. Astr. Soc.*, 89, 41-46.

Viterbi, A.J., 1966. *Principles of Coherent Communication.* McGraw-Hill, New York.

Whelan, M.P., R.P. Kenny & C. Hussey, 1998a. *Sensing Apparatus and a Measurement Method.* European Patent Application # 9820467.0, UK.

Whelan, M.P., R.P. Kenny & C. Hussey, 1998b. *A Strain Sensor and Sensing Apparatus.* European Patent Application # 9824756.2, UK.

Wielandt, E., 1987. On the Validity of the Ray Approximation for Interpreting Delay Times. In: G. Nolet (ed) *Seismic Tomography.* Reidel, Dordrecht.

Wyss, M., 1997. Second Round of Evaluation of Proposed Earthquake Precursors. *Pageoph.*, 149, 3-16.

Summary

A Seismic Transmission System for Continuous Monitoring of the Lithosphere: A Proposition

by Rudolf Unger

The principal objective of this thesis is to enhance earthquake prediction feasibility. We argue the need for, and the technological feasibility of, realizing a seismic transmission system capable of continuously monitoring the Lithosphere for changes in Earth physics quantities. The *need* for such a system arises from concise formulation of the general earthquake prediction problem, and from reviewing theoretical earthquake preparation process models and attempts to probe the Earth for potential earthquake precursors. The literature suggests that for magnitude $M = 4$, $M = 6$, $M = 8$ earthquakes, respectively, the precursor times would be on the order of one month, one year, and seventeen years, and the radii of possible precursor activity 0.6, 6.2, and 65 km. Precursory observables may be small, requiring high resolution measurement. The review leads us to the conclusion that at the present time no adequate system exists to perform the required monitoring functions with sufficient space-time resolution in a systematic, objective manner. We demonstrate the technical *feasibility* of realizing a system satisfying our objectives by presenting the concept, the design layout, and technical details of a seismic transmission system capable of precise, continuously repeated measurement, identification, and statistics compilation of potential earthquake precursors in the form of observed time-lapse changes in Earth physics quantities governing wave propagation behavior.

Such a system requires the precisely controlled, long-term phase coherent transmission and processing of coded seismic signals covering the 1-5 Hz or broader body wave frequency band, for indefinite duration. The relatively low frequencies ensure far and deep penetration; the body wave frequency band facilitates the application of body wave ray tracing methods for subsurface imaging. Moreover, in this frequency band, the signals can be adequately received, recorded, and processed at existing and next-generation permanent and portable digital seismic stations worldwide. The

signals are to be retrieved by long-term coherent, synchronous stacking of the received signals and correlation (matched filtering) with the emitted signal code. The 'indefinite duration' of coherent signal transmission and processing is required (1) to emit, over extended time, sufficient coherent signal energy to obtain, after signal energy compression by matched filtering, adequate signal-to-noise ratios over at least regional transmission ranges, and (2) to provide elapsed time signal comparison over precursor time periods of weeks, months, years, and longer. To optimize the attainable information, the signal code must be of sufficient length to generate seismograms which can accommodate the primary and major later seismic phase arrivals.

In our system concept, we achieve these goals by incorporating features taken from communications technology, and by deploying new-technology seismic sources. The communications technology concepts include long-term coherent pseudo-random sequence signal transmission and quadrature matched filter signal processing, resulting in phase coherent complex-envelope seismograms of selectable, sufficient duration, consisting of the dual time series of instantaneous amplitude and instantaneous phase. Families of pseudo-random sequences which are mutually uncorrelated, but are of identical length, and possess identical signal spectra, can be selected as the modulating signal code to enable three-dimensional, simultaneous signal transmission from different source sites. Concerning seismic sources suitable for our transmission system, existing seismic vibrator technology cannot adequately perform the functions required. For that reason, we conceived a magnetic levitation P-wave vibrator and a linear synchronous motor S-wave vibrator as surface point-force sources. Both source technologies allow precisely controlled, long-term phase coherent, low-frequency signal emission, and accommodate a broad class of signal signatures, including the conventional 'chirp' signal used in commercial exploration, and the fast changing pseudo-random sequence signals.

Regarding the complex-envelope seismogram, we establish that the instantaneous phase is more sensitive than the instantaneous amplitude in the detection of low signal-to-noise ratio (< 6 dB) signals. It is also the instantaneous phase which provides by far more precise signal arrival time information; for noise-free signals the timing resolution equals the computer's least significant bit. Taking advantage of these important features, and considering that propagation velocity change, measured as signal travel time deviation, is one of the most prominent earthquake precursors, we develop a new signal detection and timing algorithm which operates on coherent

ensembles of the instantaneous phase seismograms. From signal-plus-noise vector diagram geometry we derive a closed-form relation between signal arrival time error and signal-to-noise ratio. The timing error standard deviation ranges from less than 0.5 millisecond at 36 dB and higher seismogram signal-to-noise ratio to less than 0.5 second at -6 dB signal-to-noise ratio. This range, in combination with the capability of selecting seismogram lengths of approximately 15 minutes or longer, permits the detection and timing of primary and many later seismic phase arrivals, thus optimizing the quantity and quality of attainable potential precursor data. In addition, sufficient information is provided to perform regional 3-D ray-tracing and travel time tomography with as few as three seismic vibrator sources. The anticipated spatial resolution is on the order of 10 km for a distribution of one station per 10 km. The reciprocal of the timing error standard deviation in each detected arrival can be used as a reliability weight in inversion algorithms. Extrapolation of existing hydraulic vibrator transmission data suggests that sufficient signal-to-noise ratio over regional distances is obtained from 1-2 weeks coherent, continuous signal transmission and processing. We illustrate controlled-signal seismic wave transmission, ray tracing, and signal processing by simulating a 2-D source-receiver transmission configuration; the simulation supports the feasibility of performing seismic tomography with only a limited number of controlled-signal sources.

We formulate the transmission problem in the mathematical wave propagation and radiation context. In contrast to most literature, the static stress gradient term should not be neglected due to the low frequency energy present in our suggested pseudo-random sequence signal transmission with its 0-5 Hz, $[\sin(x)/x]^2$ power density spectrum. Accordingly, we take this term to the right-hand side of the particle velocity wave equation and consider it as an extra source term. Deviating from conventional formulation of wave propagation in an anisotropic, anelastic, inhomogeneous medium, we model anisotropy and anelasticity as perturbations in the wave propagation in a generally isotropic, but inhomogeneous medium. These perturbations take on the form of contrast-in-medium sources. This allows us to take a uniform approach by expressing all three perturbations static stress, anisotropy, and anelasticity, as contrast sources in an inhomogeneous, isotropic background medium. Adopting body wave ray theory to describe the background medium Green function tensor, we arrive at integral representations for contrast source inversion from which the static stress gradient, anisotropy, and anelasticity perturbations are to be resolved. Viewing an

earthquake preparation zone as an *emergent heterogeneity,* we propose to solve for its contrast-in medium source parameters by performing elapsed-time *travel time tomography* to obtain the preparation zone geometry, volume, and orientation, and applying *3-D contrast source inversion* methods to estimate its essential Earth physics parameters in the broadest sense, i.e., for a generally anisotropic, inhomogeneous, anelastic medium, as deviations in its inertia and compliance relaxation tensor functions.

We believe to have made plausible that our proposed system is capable of providing sufficient, high-resolution data to enable successful execution of these tomography and inversion methods. This data, obtained by *active* seismic transmission may be augmented by *passive* tomography data from earthquake and underground explosion data bases worldwide. Mapping the earthquake preparation zone in this manner, and monitoring its evolution should give greater insight in the earthquake preparation mechanics and physics, and possibly provide well-defined, short-term precursors providing estimates of earthquake location, volume, orientation, onset time, magnitude, and Earth physics parameter perturbation.

In addition to our main objective of advancing earthquake prediction feasibility, the system may be applied in general seismology research and seismic tomography experiments, in seismic engineering to measure the response of local soil conditions, buildings, or mechanical structures to remotely generated controlled seismic wave motion, and in reservoir parameter monitoring for oil, gas, and water resource management. Regional controlled-signal tomography may improve earthquake and explosion re-location procedures, and enhance Nuclear Test Ban Treaty compliance verification by providing velocity profile data for seismograph network calibration and by improving explosion yield estimation through better knowledge of the Lithosphere's heterogeneity.

Samenvatting

Een Seismisch Transmissiesysteem voor Continue Waarneming van Veranderingen in de Lithosfeer: Een Voorstel

door Rudolf Unger

Dit proefschrift beoogt voornamelijk het naderbij brengen van de mogelijkheid van aardbevingsvoorspelling. De noodzaak en de technologische haalbaarheid om een seismisch transmissiesysteem te realiseren, dat in staat is om continu veranderingen in fysische parameters in de lithosfeer waar te nemen, worden beargumenteerd. De *noodzaak* komt voort uit een precieze formulering van het probleem van de aardbevingsvoorspelling, en uit een literatuuronderzoek naar theoretische modellen van het aardbevingsproces en experimentele pogingen om aardbevingsprecursoren te vinden. De literatuur suggereert precursorperioden van ca. een maand, een jaar, en zeventien jaar, en precursorradii van 0,6 , 6,2 , en 65 km voor aardbevingen met respectievelijke magnitudes van $M = 4$, $M = 6$, en $M = 8$. Precursor parameters hebben mogelijk zeer kleine waarden, hetgeen waarnemingen met zeer hoge resolutie vereist. Het literatuuroverzicht leidt tot de conclusie dat momenteel geen systeem beschikbaar is om de waarnemingsfuncties objectief, op een systematische wijze, met voldoende ruimte-tijd-resolutie te verrichten. De technische *haalbaarheid* om een systeem te realiseren, dat aan de doelstellingen voldoet, wordt gedemonstreerd met de presentatie van concept, ontwerpplan, en technische details van een seismisch transmissiesysteem, dat in staat is continu nauwkeurig herhaalbare metingen te verrichten om veranderingen in tijdverloop waar te nemen van fysische aardeigenschappen, die de golfvoortplanting bepalen, deze veanderingen te identificeren als potentiële precursors, en statistische data-compilatie uit te voeren ter bevestiging of verwerping van de precursor-hypothesis.

Het systeem vereist preciese, gestuurde, langdurig fase-coherente transmissie en verwerking van gecodeerde seismische signalen in de 1-5 Hz of bredere 'bodywave' frequentieband, voor onbepaalde tijd. De relatief lage

frequenties verzekeren verre en diepe signaalpenetratie in de aarde, maken 'bodywave raytracing' mogelijk ten behoeve van de beeldvorming van de lithosfeer, en kunnen worden opgevangen en verwerkt op bestaande en volgende generatie vaste en mobiele digitale seismische waarnemingsstations overal ter wereld. De signalen worden boven het ruisniveau gebracht door middel van langdurig coherente, synchrone stapeling van de ontvangen golfvormen en kruiscorrelatie ('matched filtering') met de uitgezonden signaalcode. Transmissie en verwerking 'voor onbepaalde tijd' is ten eerste nodig nodig om, uitgestrekt in tijd, voldoende signaalenergie uit te zenden zodat na energiecompressie door het 'matched' filter de juiste signaal-ruisverhouding in het seismogram wordt verkregen over tenminste regionale transmissieafstanden, en ten tweede om signaalvergelijking van het tijdverloop over precursorperioden van weken, maanden, jaren, of langer mogelijk te maken. Teneinde de informatie te optimaliseren dienen de signaalcodes voldoende lang te zijn om primaire zowel als later aankomende seismische golven in het seismogram te kunnen registreren.

In ons concept kunnen wij aan deze systeemeisen voldoen door concepten uit de communicatietechniek, met name pseudo-random-sequence-signaalemissie en coherente kwadratuur-matched-filter-signaalverwerking, aan te passen aan de transmissie van seismische golven, en door technologisch nieuwe seismische bronnen te gebruiken. De communicatietechniekconcepten resulteren in complex-envelope-seismogrammen van voor ons doel voldoende lengte, bestaande uit de duale tijdreeksen van momentane amplitude en momentane fase. Suites van onderling ongecorreleerde pseudo-random-sequences, maar met identieke lengte en spectra kunnen worden geselecteerd als de modulerende signaalcodes voor driedimensionale simultane transmissie vanuit verschillende bronlocaties. Bestaande seismische bronnen, inclusief de hydraulische, elektrodynamische, of mechanische vibratoren zijn ongeschikt voor de ons gestelde doeleinden. Om die reden conceptueren wij twee nieuwe seismische vibratortechnologieën, een op magnetische levitatie gebaseerde 'P-wave'vibrator, en een op het principe van de lineaire synchrone motor gebaseerde 'S-wave'vibrator. Beide vibratoren werken als oppervlakte-puntkracht-bronnen en zijn in staat de gewenste laagfrequente, nauwkeurig gestuurde signalen op te wekken en deze signalen langdurig coherent te herhalen en te onderhouden. Signaalcoherentie tussen alle bronnen en ontvangstations wordt verkregen door middel van een precieze standaard van de Universele Tijd.

In het complex-envelope-seismogram is voor signaaldetectie, bij lage sig-

naal-ruisverhouding (< 6 dB), de momentane fase gevoeliger dan de momentane amplitude. Het is ook de momentane fase die veruit de meest precieze informatie bevat voor het bepalen van de aankomsttijd. Mede omdat de golfvoortplantingssnelheid één van de meest belovende precursors is, benutten wij deze eigenschappen en ontwikkelen een nieuw signaaldetectie- en tijdsbepaling-algorithme dat werkt op coherente ensembles van momentane fase-seismogrammmen. Met behulp van signaal-met-ruis-vectordiagrammen leiden wij een analytische uitdrukking af voor de tijdfout als functie van de signaal-ruisverhouding. De tijdfout-standaarddeviatie is minder dan 0,5 millisekonde bij 36 dB seismogram-signaal-ruisverhouding en minder dan 0,5 sekonde bij -6 dB. Dit bereik, in combinatie met een te selecteren seismogramlengte van ca. 15 minuten of langer, maakt de detectie en tijdsbepaling mogelijk van primaire en vele later aankomende golven, zodat de hoeveelheid en de kwaliteit van potentiële precursordata geoptimaliseerd wordt en bovendien de golftrajecten geometrisch een voldoende raster vormen om looptijden 'raytracing'-tomografie uit te voeren met slechts drie vibratorbronnen. De verwachte ruimtelijke resolutie is ca. 10 km voor een verdeling van één station per 10 km. Het omgekeerde van de gemeten tijdfout-standaarddeviatie kan worden gebruikt als een gewichtsfactor in inversieprocedures. Wij illustreren het totale proces van seismische golftransmissie met gestuurde signalen, 'raytracing', en signaalverwerking met een tweedimensionale configuratie van bron-ontvanger-transmissie; de simulatie ondersteunt de mogelijk-heid van seismische tomografie met een klein aantal gestuurde bronnen. Extrapolatie van bestaande (hydraulische) vibratordata suggereert de haalbaarheid van voldoende signaal-ruisverhouding over regionale afstanden met twee weken continue transmissie.

Wij formuleren het transmissieprobleem in de context van wiskundige golfvoortplantings- en stralingstheorie. In tegenstelling tot de meeste literatuur blijkt dat tengevolge van de lage frequenties in het $[\sin(x)/x]^2$-spectrum van de pseudo-random-sequence-signalen de gradient van de statische stress niet zonder meer verwaarloosd mag worden. Dienovereenkomstig brengen wij deze term naar het rechterlid in de golfvergelijking voor de deeltjessnelheid, en beschouwen deze als een extra bronterm. In afwijking van de conventionele formulering van de golfvoortplanting in een anisotropisch, anelastisch, en inhomogeen medium modelleren wij anisotropie en anelasticiteit als perturbaties in de golfvoortplanting in een algemeen isotropisch, maar inhomogeen medium. Deze perturbaties leiden tot medium-contrastbronnen. Dit maakt het mogelijk om op een uniforme behandelingswijze alle

drie perturbaties, namelijk de statische stress, de anisotropie en de anelasticiteit, voor te stellen als contrastbronnen in een inhomogeen, isotropisch achtergrondmedium waarvan de Greense tensor beschreven wordt door de theorie van de 'bodywave'-stralen. Zo komen wij tot integraalrepresentaties geschikt voor contrastbron-inversie waaruit de betreffende perturbaties moeten worden opgelost. Voor het vinden van de aardbevingsprecursoren beschouwen wij het aardbevingsvormend gebied als een gradueel tevoorschijn tredende heterogeneiteit, en stellen voor de betreffende medium-contrastparameters op te lossen door het uitvoeren van tijdverloop-voortplantingstijdtomografie ter bepaling van de geometrie, het volume, en de oriëntatie van het gebied, en toepassing van drie-dimensionale contrastbron-inversie om de essentiële fysische aardparameters te schatten in de breedste zin, namelijk voor een algemeen anisotropisch, anelastisch, inhomogeen medium, als afwijkingen in de tensorfuncties van inertia- en 'compliance'-relaxatie.

Wij menen aannemelijk gemaakt te hebben dat het door ons voorgestelde systeem in staat is om data te produceren met hoge resolutie, voldoende voor succesvolle uitvoering van de tomografie- en inversiemethoden. Deze data, verkregen met *actieve* seismische transmissie, kunnen worden aangevuld met data van *passieve* tomografie van wereldwijde aardbevings- en explosiedatabases. Het op deze wijze in kaart brengen van het aardbevingsgebied en het volgen van haar ontwikkeling in de loop der tijd zal meer inzicht geven in de mechanica en fysica van het proces van de aardbevingsvorming, en mogelijk goed gedefinieerde 'short-term'-precursoren opleveren met schattingen van hypocenter, volume, oriëntatie, aanvangstijd, magnitude en perturbatie van de fysische aardparameters.

Naast ons hoofddoel om aardbevingsvoorspelling naderbij te brengen, kan het systeem ook worden gebruikt in algemeen seismologisch onderzoek en experimenten voor seismische tomografie, in onderzoek naar seismisch resistente constructies voor het meten van de responsie van de lokale ondergrond, gebouwen of mechanische constructies op seismische golfbewegingen, die op afstand gegenereerd worden, en in de observatie van reservoirparameters ten behoeve van het management van petroleum-, gas- en waterbronnen. De tomografie van regionale gestuurde signalen kan verbetering brengen in plaatsbepalingsprocedures van aardbevingen en explosies, en in de verificatie van het 'Nuclear Test Ban Treaty' door beschikking over snelheidsprofieldata voor calibratie van seismische netwerken en door verbetering van de schatting van de explosie-'yield' door meer kennis van de heterogeneiteiten in de lithosfeer.

Curriculum Vitae of Rudolf Unger

1932: Born at Delft, 26 December.
1951: High School Diploma, Gemeentelijke Hogere Burger School, Delft.
1956: Electrical Engineering Diploma, Polytechnical College, Dordrecht.
1964: MSEE, Delft University of Technology.
1987: Patent on Magnetic Levitation Seismic Vibrator.

1956-1958: Netherlands Army Signal Corps, Lieutenant.
1958-1959: Van der Heem, N.V., The Hague/Utrecht,
Production engineer: electric consumer products.
1963-1964: Delft University of Technology, Delft, The Netherlands,
Research Assistant: Development particle accelerating machine.
1964-1969: The University of Michigan, Ann Arbor, Michigan, U.S.A.,
Research Engineer: Research and development underwater acoustics.
1969-1972: Texas Instruments, Inc., Dallas, Texas, U.S.A.,
Scientist: Development of integrated marine navigation system for seismic prospecting.
1972-1978: Texas Instruments Inc., Alexandria, Virginia, U.S.A.,
Scientist: Research and development on seismic monitoring of nuclear test ban treaty, US Government contracts.
1978-1979: ENSCO, Inc., Springfield, Virginia, U.S.A.,
Scientist: Research and development on seismic monitoring of nuclear test ban treaty, US Government contracts.
1979-1982: Universidad Nacional de Tucuman, Argentina,
Associate Professor: Teaching and research in seismic signal analysis and processing; initiator/director, digital seismic station/laboratory, USA and Argentina Governments funded research programs.
1982-1983: Royal Netherlands Meteorological Institute (KNMI),
Guest Scientist: Research on digital seismic methods for nuclear test ban treaty verification, Advice to Ad Hoc Group of Seismic Experts, Committee of Disarmament, United Nations, Geneva;
initiator, new-technology seismic long-range transmission system.
1984-1987: Delft University of Technology, Delft, The Netherlands,
Senior Scientist: Seismic signal transmission system development, Netherlands Technology Foundation (STW) grant.
1988-1997: Delft University of Technology, Delft, The Netherlands,
Lecturer Mathematics.
1990- : Unger Scientific International (USI), Houten, The Netherlands,
Consultant.
1998- : Faculty of Medicine, Universidad Nacional de Tucuman, Argentina,
Professor of Environment Modeling: Graduate Environmental Health Master's Program, Master's thesis supervisor committee member.